Dynamics and adaptation in the olfactory and phototransduction pathways

Giovanna De Palo

SISSA - International School for Advanced Studies

Supervisor: Dr Claudio Altafini
Coadvisor: Prof Anna Menini

Thesis submitted for the degree of
Doctor Philosophiæ

29th October 2012

Contents

Outline

Several biological systems have the ability to adjust the range of their sensitivity to a stimulus. This ability, called adaptation, has been widely studied in the last decades. Discovering new pathways that exhibit this capability and trying to understand the biological regulations carried out by the cells in order to achieve this form of dynamic sensitivity is an intriguing area of research.

Due to their function of "probes" of external stimuli, sensory systems have to be able to respond appropriately in a wide range of output amplitudes. As such they represent an optimal biological setting for the study of adaptation. For this reason, after a first work on the adaptation in yeast stress response (published in [21] and not included in this thesis), we have focused our research on the study of sensory transduction pathways. Sensory transduction pathways represent the first step in sensory perception and are responsible for the conversion of an external stimulus (e.g. an odorant molecule, the environment light, a particular sound) into an electrical one, then sent to the higher parts of the brain for a further elaboration. Although these pathways represent only a first stage of signal processing, it is already possible to detect in them mechanisms designed to adjust the response of the cell depending on the input amplitude.

Most of the experimental data discussed in this thesis have been recorded in the laboratory of my coadvisor Professor Anna Menini, who has been studying the olfactory transduction pathway for several years. This has allowed us to test and compare the responses of our models with a variety of different experiments, permitting a detailed analysis of the behavior of the systems. The first part of this thesis therefore focuses on the study of the olfactory transduction pathway, explaining the adaptation exhibited by this system. We then consider data obtained from phototransduction experiments and compare their properties with those of the olfactory system. Finally a detailed study of one of the ion channels involved in the olfactory transduction mechanism is presented.

In the Introduction I present a description of adaptation in biology and of the

methodologies we use in this thesis, followed by a characterization of the olfactory transduction pathway (including an in-depth presentation of the calcium-activated chloride channel) and of the phototransduction pathway.

A first dynamical model for the olfactory system is then described in the Chapter 2, containing all the significative molecular mechanisms of the pathway and explaining adaptation through the hypothesis that the molecular complexes responsible for the feedback regulation have a slower kinetic compared to the other processes involved.

This hypothesis is further developed in Chapter 3, where elementary models are presented, with the aim to find the minimal set of ordinary differential equations able to reproduce the essential features of the biological responses. In this chapter also a comparison between the adaptation present in the olfactory and phototransduction pathways is presented. In particular it is observed how it is possible to distinguish different levels of adaptation, with the olfactory response being "mode adapted" than the visual one. This difference is explained in terms of trade-off of time constant between the variables responsible for the feedback and those belonging to the open-loop part of the system.

The last chapter of the thesis presents instead a more detailed study of a specific component of the olfactory transduction pathway, the calcium-activated chloride channel. Despite the fact that the current flowing through this channel accounts for up to 90% of the total response of the olfactory sensory neuron, many features of the response of this channel are still under investigation. In particular a Markov model is used to study the dependence of the channel on its two activation mechanisms, that are the calcium ion and the transmembrane potential.

Most of the material presented in this thesis has been collected in the following papers:

- G. De Palo, A. Boccaccio, A. Miri, A. Menini and C. Altafini. "A dynamical feedback model for adaptation in the olfactory transduction pathway." *Biophysical J.*, 102(12):26772686, 2012.
- G. De Palo, G. Facchetti, M. Mazzolini, A Menini, V. Torre and C. Altafini. "Understanding the common features of sensory adaptation in photoreceptors and olfactory sensory neurons through minimal dynamical models" *Submitted for publication*
- G. De Palo, A. Boccaccio, A Menini and C. Altafini. "A dynamical model for the calcium-activated chloride channel in the olfactory transduction." *In preparation*

Chapter 1

Introduction

1.1 Adaptation in biological systems

The study of intracellular signaling pathways is fundamental for the understanding of the ability of the cells to survive and proliferate in different environmental conditions. These biochemical pathways allow the cell to organize an appropriate response to constantly changing external stimuli, such as environmental stresses, nutrients or growth factors. The different inputs received by the cells, and the consequent elicited responses, are characterized by different time dependent profiles.

The adjustments made by the cell allow it to maintain a narrow change in the vital quantities in response to broad changes of the extracellular signals. An important example of such a regulation is the phenomenon of adaptation, which can be defined as the ability of a cell to recover (partially or completely) an optimal level of some components in spite of a persistent stimulation. This allows the cell to adjust the dynamical range of the response, thereby increasing the range of sensitivity and avoiding saturation conditions which could damage the biological system.

Adaptation plays a crucial role in many signaling pathways, such as bacterial chemotaxis, yeast stress response [21] and different sensory systems [98]. One of the most investigated biological setting for the study and the modeling of adaptation is the bacterial chemotaxis [2, 1, 7, 107]. The movement of the bacterium consists of two different components: a linear run plus a random tumbling part which allows the changing of the direction. While moving, the bacterium detects the concentration of the chemoattractants and compares it with the previous value, thus measuring the spatial gradient through a temporal difference. If we take the variations of the tumbling frequency in response to changing concentrations of chemoattractants as measure of the response of the system, then we can conclude that the bacterium is

able to adapt. Indeed in the presence of a nutrient increase (or decrease) in a given direction, the tumbling probability initially decreases (increases), thus propelling the bacterium in the corresponding direction. However, after this transient response, the tumbling frequency returns to a given steady state value, independently of the new concentration of the nutrient (provided this is constant in time). This allows the bacterium to move toward the chemoattractant while the gradient is present and to restore the original tumbling-like motion once the nutrient is equally distributed in space, independently of its concentration. This type of adaptation, in which the steady state of the response of the system does not depend on the input amplitude, is called perfect adaptation.

The ideas developed for the pathway involved in bacterial chemotaxis can be successfully applied in the study of more complex biological settings. In the present thesis, we focus our attention mainly on vertebrates olfactory sensory neurons and on photoreceptors. From the point of view of signaling transduction pathways, the olfactory and visual systems share many common features. However there are significant differences between them which we are now going to underline. Both systems are present in higher organisms and both carry out highly complex functions involving many layers of neuronal activity which has been only partially decoded and understood. For the purposes of the present study the focus will be on signaling transduction at the level of the single neuron where the basic processing of the input stimulus occurs. The olfactory transduction takes place in the olfactory sensory neurons, the first cells in the whole olfaction machinery. They are located on the apical part of the nasal cavity and are responsible for the conversion of a chemical stimulus (the odorant) into an electrical one, subsequently sent through neurons connections toward the higher parts of the brain. The corresponding cell in the visual system are the photoreceptors, located in the retina, capable to convert a light stimulus into an electrical one. The effect of adaptation in these pathway is very common in our everyday life. For instance when we enter a bright room coming from a dark environment, after few seconds of being dazzled, we "adapt" to the current light and the same occurs returning to the dark environment. A similar reaction takes place for the odors, after a short time smelling some strong odor, our perception of it gradually decreases. If this "macroscopic" effect involves the whole sensor and is therefore beyond the scope of our study, traces of it are observed also in the stimulus-response curves of a single neuron and it is on these that we will focus our attention.

It is important to notice that differently from the bacterial chemotaxis, adaptation in the olfactory and phototransduction pathways (at the level of the single neuron) is not perfect. This means that in the presence of a sustained stimula-

tion lasting for several seconds (a bright light or a prolonged odor), the response of the sensory neurons does not completely disappear after the first transient, but it reaches a low level which is slightly different from the prestimulus one. This behavior is clearly detectable in the experimental data and is a novelty in the landscape of the models for the adaptation, which are instead focused on perfect adaptation.

Another peculiar feature of our work is that the data we analyze are not only responses to sustained stimulations lasting several seconds, but also responses to short pulses of light or odorant molecules, thus allowing us to make more detailed investigations on the dynamics of the response.

1.2 Modeling techniques

The molecular pathways previously mentioned are characterized by the presence of an extracellular input to which corresponds a measurable response of the cell. This biological setting can be modeled by a dynamical system, representable through ordinary differential equations (ODE). More precisely if we denote $u = u(t)$ the time-dependent input of the system and $y = y(t)$ the corresponding output (i.e. the measured response), then our model is given by the following formulæ:

$$\begin{aligned} \dot{z} &= g(u, z) \\ y &= f(u, z), \end{aligned} \tag{1.2.1}$$

where $z(t) = (z_1(t), ..., z_n(t))$ represents the vector of the state variables characterizing the system.

For the sensory transduction systems we are considering, the input consists of a flash of light or of a release of odorant molecules, the output is the current produced on the surface of the sensory neurons and the different components of the pathway can be represented through the state variables.

Following the introduced formalism, the system (1.2.1) adapts perfectly if the steady-state output y equals a fixed y_0, independently on the constant value assumed by u. This property means that in correspondence of a step input, the output of the system, after an input-dependent transient, will be constant and exactly equal to the prestimulus level y_0 regardless of the amplitude of the step. This is the behavior expected in bacterial chemotaxis.

A first feature in order to distinguish the possible models able to explain adaptation is their robustness [1, 2, 7, 84]. It has been shown that *biological circuits have robust designs such that their essential function is nearly independent of biochemical*

parameters that tend to vary from cell to cell [2]. Consequently we can classify a model as robust if the qualitative behavior of the output time profile is independent of the model parameters. However it is necessary to distinguish which is the feature we are looking at and if that feature is robust to specific parameter variations. On the contrary characteristics which constantly depend upon certain parameter values are said to be fine-tuned. An example of a model for bacterial chemotaxis in which adaptation is a fine-tuned property is described in [41]. In a mechanism of this type, the steady state value in response to an input step is constrained to be equal to the prestimulus value, choosing values of the parameters that satisfy this constraint. As soon as the parameters are perturbed, the match between the steady state of the step response and y_0 is lost, hence the behavior of the model is not robust. Barkai and Leibler [7] proposed instead a model for the same biological setting allowing exact adaptation for a wide range of parameters variations. Their model is more interesting from a theoretical point of view since adaptation turns out to be an intrinsic feature, depending upon how the model is built.

In the landscape of robust models explaining perfect adaptation in response to a step which have been built in the last decade it is possible to point out two main schemes: the integral feedback and the incoherent feedforward loop. The integral feedback control (Fig. 1.1) is a well known scheme in control theory and it was initially proposed to explain adaptation in bacterial chemotaxis by Doyle and collaborators [107]. In this type of scheme, there is a "memory" variable (x in Fig. 1.1), which keep tracks of the past history of the system, intended as the difference between the present value of the output $y(t)$ and the desired steady-state value y_0. Feeding back to the system the value of the integral of this "error" (the variable x) ensures that the steady-state error for y approaches y_0 despite of parameters or input fluctuations. A scheme of this type guarantees a perfect adaptation. Recalling the previously introduced formalism, let $z = (x, y)$ represents a two component states vector in which the output of the system is identified with the state variable y.

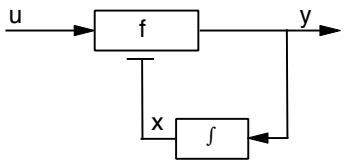

Figure 1.1: **Integral feedback scheme**

The equations of this scheme become as follow:

$$\begin{aligned} \dot{x} &= g(x, y) = y - y_0 \\ \dot{y} &= f(u, x, y) \end{aligned} \tag{1.2.2}$$

The second possible scheme to achieve perfect adaptation for a step input is given by incoherent feedforward loops (Fig. 1.2). Feedforward motifs have been found to be overrepresented in biology [2], in particular in *E. coli* transcription networks [62] and recently the incoherent configuration has been consider as a possible scheme explaining adaptation [89, 95, 100]. In this scheme, the input u promotes the activity of both the output y and of the inhibitor x of the output, thus acting as a delayed inhibitor.

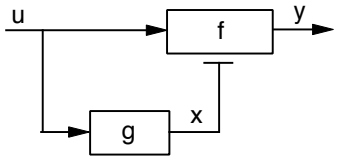

Figure 1.2: **Incoherent feedforward loop scheme**

The corresponding equations are:

$$\begin{aligned} \dot{x} &= g(u, x) \\ \dot{y} &= f(u, x, y) \end{aligned} \tag{1.2.3}$$

In this motif feedback regulation is completely absent. Although it is robust with respect to perfect adaptation to constant steps, lack of feedback means it is inadequate for many other tasks ad in particular that it is not suitable for our sensory pathways, in which regulation is known to play a key role. For this reason hereafter we will focus our work on the integral feedback scheme.

1.3 The transduction pathways

1.3.1 The olfactory transduction pathway

Olfactory transduction occurs in the cilia of olfactory sensory neurons (OSNs, see Fig. 1.3). OSNs are bipolar neurons with an axon, soma, dendrite and several cilia protruding from the apical side of the dendrite [40, 85].

The binding of an odorant molecule to an odorant receptor on a cilium induces a conformational change of the receptor causing the activation of an interacting G-protein. In turn, the G-protein stimulates the enzymatic activity of an adenylyl cyclase (AC) generating an increase in the concentration of cyclic AMP (cAMP). Cyclic nucleotide-gated (CNG) channels located in the ciliary membrane are directly activated by cAMP, causing a depolarizing influx of Na^+ and Ca^{2+} ions. The intracellular increase of Ca^{2+} concentration directly gates Ca-activated Cl channels. Since OSNs maintain an unusually high internal concentration of Cl^-, which is in the same range as the Cl^- concentration present in the mucus at the external side of the ciliary membrane, the opening of Ca-activated Cl channels causes an efflux of Cl^- ions from the cilia, corresponding to an inward current that further contributes to the depolarization of OSNs [40, 70]. The depolarization spreads passively to the dendrite and soma of the neuron, triggering action potentials that are conducted along the axon to the olfactory bulb.

Several Ca-dependent feedback mechanisms may contribute to adaptation. The cilia contain a phosphodiesterase that, after being activated by the complex Ca-Calmodulin (CaCaM), hydrolyzes cAMP [13]. The complex CaCaM and possibly other Ca-binding proteins decrease the sensitivity of the CNG channel to cAMP [6, 14, 19]. The activation of CaCaM-dependent protein kinase II (CaMK) inhibits AC activity [103]. Finally, the intracellular Ca^{2+} concentration is reduced by Ca-extrusion through a Na^+/Ca^{2+} exchanger [60].

The cilia contain only two types of ion channels, CNG and Ca-activated Cl channels. Voltage-gated channels are instead located in other compartments of OSNs: dendrite, soma and axon. The depolarization originating in the cilia spreads to the soma where action potentials originate and carry the information to the olfactory bulb [40, 85]. Here, we study the transduction current in voltage-clamp conditions to isolate the transduction properties of the cascade from voltage-gated channels. The generation of action potentials occurring at the soma and spike rate adaptation depends also on the specific properties of the voltage-gated channels expressed by OSNs and are not considered in this thesis. However, it is worth noting that adaptational properties have also been measured in OSNs in vivo in some pioneering

studies, as reviewed by Getchell [29]. Both the generator potential measured using electroolfactograms in frogs [68] and single unit extracellular recordings from salamander OSNs [30] exhibited step adaptation and multipulse adaptation in response to odorants.

These results indicate that the choice of the transduction current as the output of OSNs is also a good representation of the response of OSNs in natural conditions.

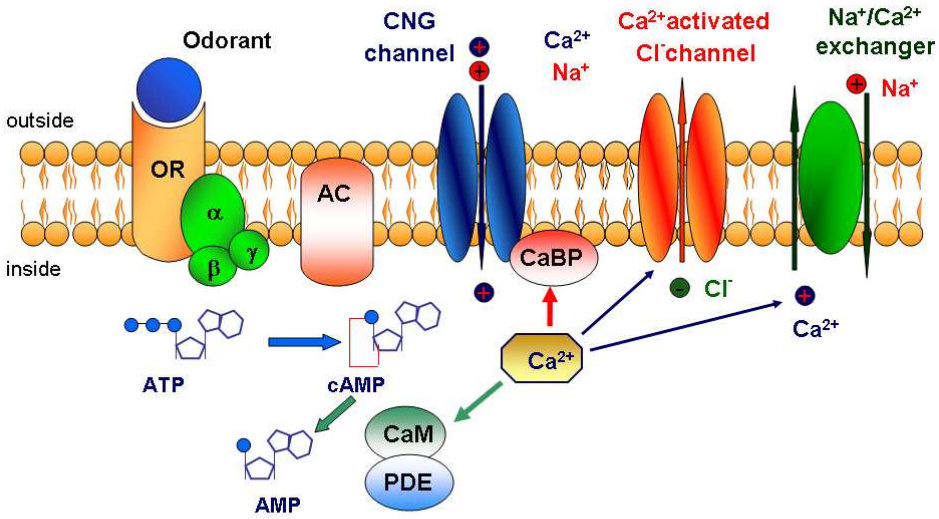

Figure 1.3: **The olfactory transduction pathway and its feedback loops in olfactory sensory neurons cilia.**(modified from [70])

1.3.2 Ion channels in the olfactory transduction

As discussed in the previous paragraph, the olfactory transduction current is composed by the current flowing through two main type of channels: the cyclic-nucleotide-gated channels and the calcium-activated chloride channels.

The cyclic nucleotide gated channels are composed by four subunits forming a tetramer with a central pore [38]. They are permeable to all monovalent cations

Na^+, K^+, Li^+, Rb^+ and Cs^+ and by divalent cation such as Ca^{2+} and Mg^{2+} and are activated by a direct binding of a cyclic nucleotide such as cAMP or cGMP [24, 66]. These channels are sensitive to the calcium-calmodulin complex, which lowers the affinity of the channels for the cyclic nucleotides [38]. This mechanism constitutes one of the two main feedback loops responsible for the adaptation in the olfactory transduction pathway.

The calcium-activated chloride channels (CaCCs) act as amplifiers in the olfactory transduction pathway. Indeed it has been shown that in rat and mouse they account for up to 85%-90% of the total current induced during the response to an odorant [12, 67, 78]. In the rat olfactory cilia the channel density has been estimated to be four chloride channels per cyclic nucleotide gated channel [78]. Despite its importance, the molecular identity of this calcium-activated chloride channel has remained unknown until 2008. In that year three different groups showed that TMEM16A, or Anoctamin1, functions as Ca^{2+}-activated Cl^- channel [17, 86, 105]. The following year, 2009, it was found that another member of the same family, TMEM16B/Anoctamin2 functions as CaCC [71, 92, 93]. Moreover TMEM16B is expressed in olfactory sensory neurons [9, 83] and it was shown that calcium-activated chloride currents were undetectable in mice lacking this protein [9]. This connection with the olfactory transduction and the surprising little knowledge of it, led us to focus our study on the modeling of the behavior of TMEM16B/Anoctamin2.

1.3.3 The visual transduction pathway

The neurons responsible for the conversion of the light into an electrical signal are called photoreceptors. They are located in the retina and can be divided in two types: rods and cones. Rods exhibit a high sensitivity to light, though their response is relatively slow. The response of cones is less sensitive, faster, noisier and they are able to provide the color vision. These features render the rods more specific for nocturnal vision and the cones for the case of a bright light. Despite of this different behavior, the main components in the phototransduction of rods and cones are very similar.

In the inset of Fig. 1.4 it is possible to see a drawing of a rod structure. Every photoreceptor is divided into an outer segment region, responsible for the phototransduction, and an inner segment region, providing energy to the cell and connecting it through the synaptic terminal. The rods outer segment is filled with a stack of disks containing a high concentration of the visual pigment rhodopsin. The cones possess a slightly different visual pigment included directly into foldings of the cytoplasmic membrane [46, 73, 106].

A scheme of a rod phototransduction pathway is presented in Fig. 1.4. The absorption of a photon converts rhodopsin into its active form Rh^*. This in turn promotes the activity of a G-protein, which binds and activates the phosphodiesterase PDE, thus catalyzing the hydrolysis of cyclic-GMP (cGMP). The consequent drop in the concentration of cGMP induces the closure of the cyclic-nucleotide-gated channels (CNG), permeable to sodium and calcium ions. The Na^+/Ca^{2+}, K^+ exchanger continues its action of pumping extracellularly the calcium ions, thus causing a decrease in the intracellular calcium concentration. Calcium is responsible for three main feedback mechanisms: Ca^{2+} can bind to guanylyl cyclase activating protein (GCAP), blocking its binding to GC and the following increase of GC activity; the calcium-calmodulin complex bound to the CNG channel decreases the affinity of the channel for cGMP; and the calcium-binding protein recoverin inhibits, through the G protein-coupled-receptor-kinase 1 (GRK1), the phosphorilation reaction of rhodopsin. In this way the decreasing concentration of calcium promotes the activity of GC and the opening of the CNG channels, while at the same time decreasing the amount of available (non phosporilated) rhodopsin [46, 73, 106].

In rods the feedback action of calcium ion on the CNG channels is of little account with respect to the other two mechanisms [45]. At low and intermediate light intensities, the dominant feedback is that involving the modulation of the GC, at higher intensities the feedback due to the action of the recoverin acquire increasing importance [106].

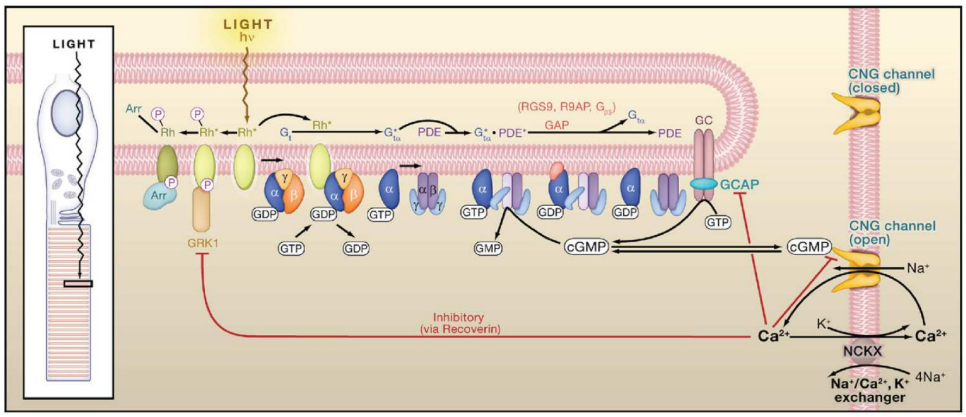

Figure 1.4: **The phototransduction pathway and its feedback loops in vertebrate rods.**[106]

Chapter 2

A detailed dynamical model explaining adaptation in the olfactory transduction pathway

2.1 Background

In order to optimize the signal-to-noise-ratio over a range of input intensities, vertebrate sensory neurons (olfactory, visual and auditory, see [98]) are able to adjust their dynamical range maintaining the response around a nominal value, while their input stimulus changes considerably. Sliding the window of interest maximizes the capacity for distinguishing variations of a signal while avoiding distortions due to saturation. In the biological literature, this process is called adaptation [8, 88, 98].

As explained in the Introduction of this thesis, in olfactory transduction, the ordinary input to an olfactory sensory neuron (OSN, here, the "sensor") consists of a stimulation by odorant molecules eventually leading to an electrical signal. Here we consider the transduction current measured with the voltage clamped at a constant value as the measurable output of the pathway (see Subsection 2.3 for details). Two forms of adaptation of the odorant-induced current response [48, 49, 51, 79] are observed during two types of experimental protocols:

1. *Step adaptation*, which is caused by a sustained stimulus (a step input) and consists of a decline in the response despite the continued presence of a constant odorant stimulus;

2. *Multipulse adaptation*, which is caused by repeated brief stimuli and involves a

reduction in the amplitude of the response to the second odorant stimulus with respect to the first. The difference in amplitude of the responses is reduced when the time interval between stimuli is increased; complete recovery of the response is seen for a sufficiently long interval.

In step adaptation, the return of the transduction current toward the basal pre-stimulus level implies that the system has a memory of the basal level and a mechanism enabling regulation around it. Multipulse adaptation in OSNs also represents a form of memory: the attenuation of the transduction current in response to the second pulse means that also in this case the past history of the system can influence its present behavior [49]. In spite of the evidently similar nature of the two phenomena, mathematical models taking into account both forms of adaptation are very rare (the only papers we know of are [22, 76]). The aim of this work is to provide insight into the mechanism of step and multipulse adaptation by constructing a mathematical model of the olfactory transduction pathway that reproduces these phenomena.

Several mathematical models capturing step adaptation have been reported in the literature, see Refs. [1, 2, 8, 28, 100, 107]. Most of these models describe kinetic mechanisms suitable to attain perfect adaptation, in which a new steady state value exactly corresponds to the pre-stimulus value. In voltage clamp experiments on OSNs, however, step adaptation is never perfect: a (small) difference between the pre-stimulus value of the current and the new steady state value achieved after a step-like stimulation is always observed [49, 61], with an amplitude that typically grows with the size of the step (see [61], Fig. 1). We will show here that imperfect step adaptation and multipulse adaptation can be explained by the same mechanism.

Conceptually, our model derives from the integral feedback model of [107]. In this scheme, feedback evokes temporal integration of the past history of the output in order to force it to return to its pre-stimulus value. For systems in which the signals have constant sign (positive concentrations) a perfect memory of the past implies a feedback variable that is monotonically increasing. However, in olfactory transduction, the strength of adaptation in a multipulse protocol decays as the interpulse interval increases, meaning that the memory of the past is gradually forgotten by the system. An exact integral feedback adaptation cannot capture this feature, just like it does not predict the displacement between steady state and pre-stimulus value in the step adaptation. However, if we add a memory decay to the integral feedback model, its monotonic character is lost and both types of adaptation can be correctly reproduced.

Olfactory transduction occurs in the cilia of OSNs. The cilia contain all the bio-

chemical machinery for transduction and two types of ion channels: cyclic nucleotide-gated (CNG) and Ca-gated Cl channels (see Fig. 2.1). Voltage-gated channels for the generation of action potentials are located in other compartments of OSNs and are not activated when the voltage is clamped at a constant value, thereby decoupling the olfactory transduction process from the spiking events. The main steps of olfactory transduction involve the binding of extracellular odorant molecules to odorant receptors (ORs), which induces intracellularly a G-protein mediated activation of adenylyl cyclase (AC) to produce cyclic AMP (cAMP). cAMP then directly gates CNG channels, causing an influx of Na^+ and Ca^{2+} ions. Ca^{2+} entry amplifies the response by gating a Cl^- current and, in combination with Ca-binding proteins, induces feedback mechanisms: Ca-calmodulin (CaCaM) increases the phosphodiesterase (PDE) hydrolysis of cAMP, and activates CaCaM-dependent protein kinase II (CaMKII), which inhibits AC. Moreover, the cAMP sensitivity of the CNG channels is reduced by Ca^{2+} feedback mediated by CaCaM and/or other Ca-binding proteins natively bound to the CNG channels (see Section 1.3 for a detailed description of the pathway, and for reviews, see [40, 85]).

Previous experiments have shown that the shape of the response to odorants can be reproduced by increasing the concentration of cAMP in the cilia via photorelease of caged cAMP (see Fig. 4 of [96], or Fig. 2 of [48]), indicating that the response time course is not significantly altered by the events occurring in the pathway upstream of the production of cAMP (receptor activation, G-protein and AC signaling). Furthermore, it has been shown that the principal molecular mechanisms underlying multipulse odorant adaptation occur after the production of cAMP, since the responses to repeated photorelease of cAMP have adaptation properties similar to those induced by odorants [48]. We therefore decided to focus our study on the part of the pathway downstream of the production of cAMP, where Ca-mediated regulatory mechanisms play a key role. Ca-induced feedbacks are crucial for adaptation: indeed, it has been shown that in the absence of Ca^{2+} influx, achieved either by removing Ca^{2+} from the extracellular solution [49, 54] or by recording the current at positive membrane potentials [11], neither form of adaptation can take place.

The common dynamical explanation for both types of adaptation provided in this work relies on the kinetics of the Ca-induced feedback being slower than the kinetics of the gating of the CNG channels and Ca^{2+} influx through CNG channels. We will show that by modulating the time constants of these kinetics with respect to the other time constants of the system, a trade-off between the two forms of adaptation is established. For example, assuming a very long time constant for the feedback results in a nearly exact step adaptation but in an amplitude recovery of multipulse adaptation that is slower than that observed experimentally. On the

contrary, assuming a short time constant for the feedback leads to incomplete step adaptation but to faster recovery in multipulse adaptation. This trade-off implicitly constrains the range of values of the parameters in which the behavior of the model reflects the experimental data. We show here that for both input protocols (sustained and repeated stimuli) a variety of data obtained in different experimental conditions (different species; stimulation by odorant or by direct release of second messengers) lead to fairly similar values of the parameters. Our results demonstrate that both types of adaptation can be reproduced correctly if the system is endowed with multiple time scales, such that the regulatory actions have longer time constants than the direct transduction of stimuli to membrane current. This kinetic property is the basis for several models proposed for (step) adaptation [2, 28], and is also consistent with hypotheses presented in the olfactory transduction literature ([55], see also [76]).

2.2 Model

Fig. 2.1 A illustrates the main steps of the olfactory transduction cascade (see also Section 1.3 for a detailed description). We focused our study on the part of the pathway downstream of the production of cAMP and considered experimental data obtained using a constant voltage protocol (thus the voltage dependence does not appear in the model proposed here). Hence, here the "open-loop" part of the pathway (the signaling cascade from the input stimulus to the output current, feedback excluded) consists of the cAMP-induced opening of the CNG channels and the influx of Ca^{2+} into the cilia, while the feedback part involves the Ca-binding proteins, which directly (through their gating action on the CNG channels) or indirectly (through the activation of PDE) lead to the closure of the CNG channels. Both feedback actions are subordinated to Ca^{2+} influx.

The model of Ordinary Differential Equations (ODEs) we use consists of the following five state variables:

1. [cAMP], the concentration of the cyclic nucleotide,
2. [CNG_o], the concentration of open CNG channels,
3. [Ca], the concentration of Ca^{2+} free ions,
4. [CaBP], the concentration of the complex formed by Ca^{2+} and Ca-binding proteins (BP) natively bound to CNG channels,
5. [CaCaM], the concentration of the cytoplasmic Ca-calmodulin complex.

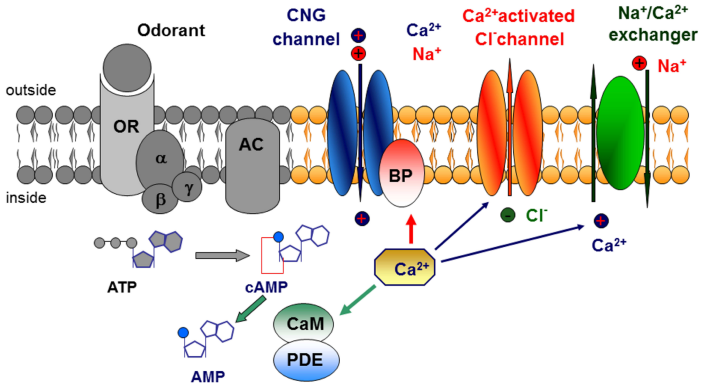

A

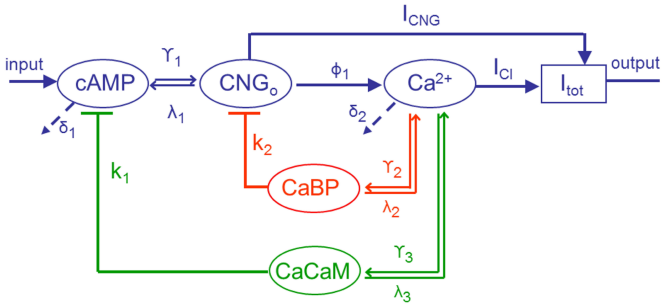

B

Figure 2.1: **The pathway and its feedback loops.** (A) Representation of the entire olfactory transduction pathway in the cilia of OSNs. Modified from [70]. The part in gray is not considered in this study. (B) Scheme of the basic reactions and feedback mechanisms included in our model. The pointed arrows represent positive regulation, stopped arrows represent negative feedbacks, and dashed arrows degradations. The three bidirectional arrows represent reversible reactions. The two feedback loops are represented in red and green.

CaCaM is taken here as a proxy for the PDE activity (not modeled explicitly), and the complex CaCaM is assumed to be free in the ciliary cytoplasm. It is known that Ca-free calmodulin is also pre-associated with CNG channels and facilitates a rapid Ca-dependent reduction in cAMP sensitivity of the CNG channels [14]. However, since calmodulin may not be the only protein involved in this process [6], we take a more general perspective and attribute the reduction in sensitivity for cAMP of the CNG channels to a "generic" BP natively bound to the channels and whose action is triggered by Ca^{2+}. Thus the variable [CaBP] summarizes the effect of potentially more than one type of Ca-binding proteins (including also calmodulin) that are assumed to be permanently bound to the CNG channels and able to rapidly reduce their sensitivity for cyclic nucleotides when activated by the binding with Ca^{2+}. While the first three variables form the open-loop part of the model, the pair [CaCaM] and [CaBP] are our feedback variables (Fig. 2.1 B). Their action in generating dynamical feedback can be formulated using ODEs, as follows:

$$\begin{aligned}
\frac{d[\mathrm{cAMP}]}{dt} &= 2\lambda_1 \cdot [\mathrm{CNG_o}] - 2\gamma_1 \cdot [\mathrm{cAMP}]^2([\mathrm{CNG_{tot}}] - [\mathrm{CNG_o}]) \\
&\quad -\delta_1 \cdot [\mathrm{cAMP}] - \mathrm{f_1}([\mathrm{cAMP}], [\mathrm{CaCaM}]) + \mathrm{u} \qquad (2.2.1) \\
\frac{d[\mathrm{CNG_o}]}{dt} &= \gamma_1 \cdot [\mathrm{cAMP}]^2([\mathrm{CNG_{tot}}] - [\mathrm{CNG_o}]) - \lambda_1 \cdot [\mathrm{CNG_o}] \\
&\quad -\mathrm{f_2}([\mathrm{CNG_o}], [\mathrm{CaBP}]) \qquad (2.2.2) \\
\frac{d[\mathrm{Ca}]}{dt} &= \phi_1 \cdot [\mathrm{CNG_o}] - \delta_2 \cdot [\mathrm{Ca}] \\
&\quad -\gamma_2 \cdot [\mathrm{Ca}]([\mathrm{BP_{tot}}] - [\mathrm{CaBP}]) + \lambda_2 \cdot [\mathrm{CaBP}] \\
&\quad -2\gamma_3 \cdot [\mathrm{Ca}]^2([\mathrm{CaM_{tot}}] - [\mathrm{CaCaM}]) + 2\lambda_3 \cdot [\mathrm{CaCaM}] \qquad (2.2.3) \\
\frac{d[\mathrm{CaBP}]}{dt} &= \gamma_2 \cdot [\mathrm{Ca}]([\mathrm{BP_{tot}}] - [\mathrm{CaBP}]) - \lambda_2 \cdot [\mathrm{CaBP}] \qquad (2.2.4) \\
\frac{d[\mathrm{CaCaM}]}{dt} &= \gamma_3 \cdot [\mathrm{Ca}]^2([\mathrm{CaM_{tot}}] - [\mathrm{CaCaM}]) - \lambda_3 \cdot [\mathrm{CaCaM}] \qquad (2.2.5)
\end{aligned}$$

where the initial concentrations correspond to a basal pre-stimulus level.

In Eqs (2.2.1)-(2.2.5) the total concentrations of the CNG channels $[\mathrm{CNG_{tot}}]$, calmodulin $[\mathrm{CaM_{tot}}]$ and the Ca-binding proteins $[\mathrm{BP_{tot}}]$ are conserved. No conservation law is imposed on the low molecular weight [cAMP] and [Ca]. Since Ca^{2+}:cAMP:CaM have molecular weights 40:329:16800, this assumption is reasonable: small molecules can diffuse more rapidly in the cytoplasm of the neuron. In addition Ca^{2+} and cAMP cannot be conserved because they are also involved in non-conservative reactions: Ca^{2+} can enter the cell through the CNG channels, can diffuse away from the internal membrane and can be extruded through Na^+/Ca^{2+} exchangers; cAMP can be hydrolyzed by PDE. Most of the terms appearing in Eqs (2.2.1)-(2.2.5) are derived from mass action kinetics. We report here the corresponding reactions:

$$2\ \mathrm{cAMP} + \mathrm{CNG_c} \underset{\lambda_1}{\overset{\gamma_1}{\rightleftharpoons}} \mathrm{CNG_o}$$
$$\mathrm{Ca^{2+}} + \mathrm{BP} \underset{\lambda_2}{\overset{\gamma_2}{\rightleftharpoons}} \mathrm{CaBP}$$
$$2\ \mathrm{Ca^{2+}} + \mathrm{CaM} \underset{\lambda_3}{\overset{\gamma_3}{\rightleftharpoons}} \mathrm{CaCaM}$$

where

$$\begin{aligned} [\mathrm{CNG_c}] + [\mathrm{CNG_o}] &= [\mathrm{CNG_{tot}}]; \\ [\mathrm{BP}] + [\mathrm{CaBP}] &= [\mathrm{BP_{tot}}]; \\ [\mathrm{CaM}] + [\mathrm{CaCaM}] &= [\mathrm{CaM_{tot}}]. \end{aligned}$$

The input stimulus u appears as a synthesis term in Eq. (2.2.1) for cAMP, having distinct temporal profiles for the different stimuli used (see Subsection 2.4.4). Two more terms in Eq. (2.2.1) describe the binding/unbinding of cAMP to the CNG channels (the term $[\mathrm{CNG_{tot}}]$-$[\mathrm{CNG_o}]$ represents the concentration of closed channels). Eq. (2.2.1) also involves a linear degradation term representing the diffusion of the nucleotide away from the internal membrane surface, and a negative feedback term due to the hydrolysis induced (through PDE) by the CaCaM complex (green stopped arrow in Fig. 2.1 B). The simplest way to represent this feedback action avoids modeling explicitly PDE and is given by

$$\mathrm{f_1}([\mathrm{cAMP}], [\mathrm{CaCaM}]) = \mathrm{k_1} \cdot [\mathrm{cAMP}] \cdot [\mathrm{CaCaM}]. \tag{2.2.6}$$

This term was difficult for us to represent through mass action kinetics due to the lack in our model of a variable representing the adenylyl cyclase responsible in the biological pathway for the regeneration of cAMP. To describe the opening rate of the CNG channels in Eq. (2.2.2), we use a mass-action law with cooperativity index 2 for cAMP because the binding of two molecules of cAMP is sufficient to open the channel [10, 40, 65]. In Eq. (2.2.2), besides the association/dissociation with cAMP, $[\mathrm{CNG_o}]$ decreases due to negative feedback of the CaBP complex (red feedback loop in Fig. 2.1 B).This negative gating activates only when $\mathrm{Ca^{2+}}$ binds to the Ca-binding proteins permanently attached to the CNG channel and is represented as a negative term which "competes" with the positive term (gate opening induced by cAMP) thereby reducing the sensitivity of the channel to cAMP. The simplest possible functional form to express this feedback is

$$\mathrm{f_2}([\mathrm{CNG_o}], [\mathrm{CaBP}]) = \mathrm{k_2} \cdot [\mathrm{CNG_o}] \cdot [\mathrm{CaBP}]^2 \tag{2.2.7}$$

where a cooperativity index 2 is assumed for CaBP to account for the possible presence of multiple units of BP in the complex they form with the CNG channels, as reported for example for calmodulin [14, 99]. An alternative model to describe this

negative gating is described in Subsection 2.4.7. Eq. (2.2.3) represents the inflow of free Ca^{2+} ions into the cilia which depends on $[CNG_o]$, on their diffusion away from the internal membrane surface (and extrusion through the Na^+/Ca^{2+} exchanger), and on their binding/unbinding with calmodulin and Ca-binding proteins. The remaining Eqs (2.2.4)-(2.2.5) for [CaBP] and [CaCaM] represent mass action laws for the binding and unbinding of Ca^{2+} ions. For simplicity we assume a linear behavior between Ca and BP, while for the binding to CaM, following [76], we consider a cooperativity index equal to 2 (the four binding sites for Ca^{2+} are highly cooperative in pairs, see [69]).

The total elicited transduction current (the output measured in experiments) is the sum of two distinct inward currents: one component carried by the influx of Na^+ and Ca^{2+} through CNG channels and the other carried by the efflux of Cl^- through channels gated by Ca^{2+}. The equations for the currents are therefore:

$$I_{CNG} = k_c \cdot I_{max} \cdot [CNG_o] \tag{2.2.8}$$

$$I_{Cl} = (1 - k_c) \cdot I_{max} \Big(\frac{[Ca]^2}{[Ca]^2 + k_{1/2}^2} \Big) \tag{2.2.9}$$

Thus, the output of our model is given by the sum of I_{CNG} and I_{Cl}. The constant k_c, representing the relative contribution of the two currents, is known to be approximately 20% in the case of a nearly-saturating response [12]. I_{CNG} depends on the number of open channels and we use a direct proportionality with $[CNG_o]$. I_{Cl} depends on the fraction of open Cl channels, which is a function of the Ca^{2+} concentration [94] described by a Hill-equation with a cooperativity index of 2 [11, 40].

2.2.1 Choosing the pre-stimulus baseline level

For some of the quantities of interest in our model, ranges of plausible values of basal (pre-stimulus) concentrations in the olfactory cilia are available. This concerns in particular cAMP and Ca^{2+}. For cAMP, the literature reports a basal concentration of $\sim 0.1\mu$M [13, 75] and a peak of concentration $\sim 100\mu$M during the response to a stimulus [97]. We used this information to normalize the value of [cAMP] in our simulation so that the magnitude of the transient never exceeds a 10^3 ratio with respect to its basal value (for reasonable values of the parameters, not necessarily for the optimal set). Knowing the ratio of the output current before/after a stimulus allows us to choose a proper initial value for [Ca] and for $[CNG_o]$ compatible with the data. As for the other state variables, plausible values can easily be chosen, assuming that at steady state (without input), the feedbacks are nearly inactive.

Once the parameters are chosen, to avoid spurious prestimulus transients in the simulations, the initial condition of the state variables is set equal to the steady state reached by the system in correspondence of u=0.

2.3 Experimental Methods

Patch clamp experiments on dissociated olfactory sensory neurons Olfactory sensory neurons were dissociated from the olfactory epithelium of newts (*Cynops pyrrhogaster*) as described in [47, 48], salamanders (*Ambystoma tigrinum*) as in [25] or mice (BALB/c strain) as in [51]. All experiments were carried out in accordance with the Italian Guidelines for the Use of Laboratory Animals (Decreto Legislativo 27/01/1992, no. 116). Olfactory sensory neurons were identified by their characteristic bipolar shape and only neurons with clearly visible cilia were used for the experiments. Currents were measured in the whole-cell voltage-clamp mode as previously described [25, 48, 51]. Transduction currents were elicited by odorant, IBMX, the photorelease of cAMP [11, 48] or its non-hydrolyzable form 8-Br-cAMP [11], and were recorded at a holding potential of -50 mV. IBMX was dissolved in DMSO at 100 mM and an aliquot was added to the Ringer solution to obtain a final concentration of 0.1 mM. IBMX was applied to the neurons through a glass micropipette by pressure ejection (Picospritzer, Intracel, United Kingdom). All experiments were performed at room temperature.

Photolysis of Caged Compounds Caged cAMP (Dojindo, Japan) and BCMCM-8-Br-cAMP (provided by V. Hagen, Leibniz-Institut fur Molekulare Pharmakologie, Berlin, Germany, [11]) were dissolved in DMSO. Final concentrations were obtained by diluting an aliquot of the stock solution into the pipette solution. Caged compounds diffused into the neuron through the patch pipette and cyclic nucleotides were photoreleased by ultraviolet flashes applied to the ciliary region through the epifluorescence port of the microscope [11, 48]. For the experiments in the newt the light source was a 100W mercury lamp. Timing and duration of the flash were regulated by a mechanical shutter as described in [48]. For the experiments performed in the mouse the light source was a xenon flash-lamp JML-C2 system (Rapp OptoElectronic, Hamburg, Germany) that allowed an intense and short light flash (about 1.5 ms), as described in [11].

2.4 Results

In the present section we describe the experimental data, followed by a fit performed with the model of Eqs (2.2.1)-(2.2.7), and by the description and evaluation of the fitting procedure. Finally we introduce a possible alternative model, presenting the corresponding simulations and comparing it with the model of Eqs (2.2.1)-(2.2.7).

2.4.1 Description of the experiments

To test the ability of the model to reproduce the adaptation of OSN responses, we considered data from various experimental conditions in which responses were elicited by different stimuli: (i) odorant, (ii) photorelease of caged cyclic nucleotides, either cAMP or 8-Br-cAMP, and (iii) IBMX. All experiments considered here were performed in voltage-clamp conditions, holding the membrane voltage constant at -50 mV for the entire duration of the experiment. This allows the measurement of transduction currents without the interference of action potentials.

(i) Response to odorant. A typical example of multipulse odorant adaptation in an OSN is illustrated in Fig. 2.2 A. Responses to pairs of identical odorant pulses separated by a variable time interval Δt are plotted superimposed. The amplitude of the response to the second pulse is reduced with respect to the first, and progressively recovers to the initial value as Δt is increased. The input is modeled as a pair of square pulses of the same duration and Δt as the experimentally delivered odorant pulses. Fig. 2.2 B shows an example of step odorant adaptation. The current response declines to an almost basal steady-state level in spite of the persistent odorant stimulus.

(ii) Response to photorelease of caged compounds. The stimulus is given by the photorelease of caged cyclic-nucleotides: in Fig. 2.3 A cAMP is released with 100 ms light flashes, while in Fig. 2.3 B the non-hydrolyzable 8-Br-cAMP is released with briefer, about 1.5 ms, but more intense flashes. The input is modeled as a pair of square pulses of a similar duration and the same Δt as in the experiments. For both types of caged compounds, we assume that the concentration of the cyclic nucleotide depends on the intensity and duration of the different flashes. As 8-Br-cAMP is not hydrolyzable by PDE [16, 101], we consider PDE to be inactive in this case, and therefore the CaCaM feedback is absent from the model. Multipulse adaptation similar to that observed with odorants is seen with photorelease of both cAMP and of 8-Br-cAMP.

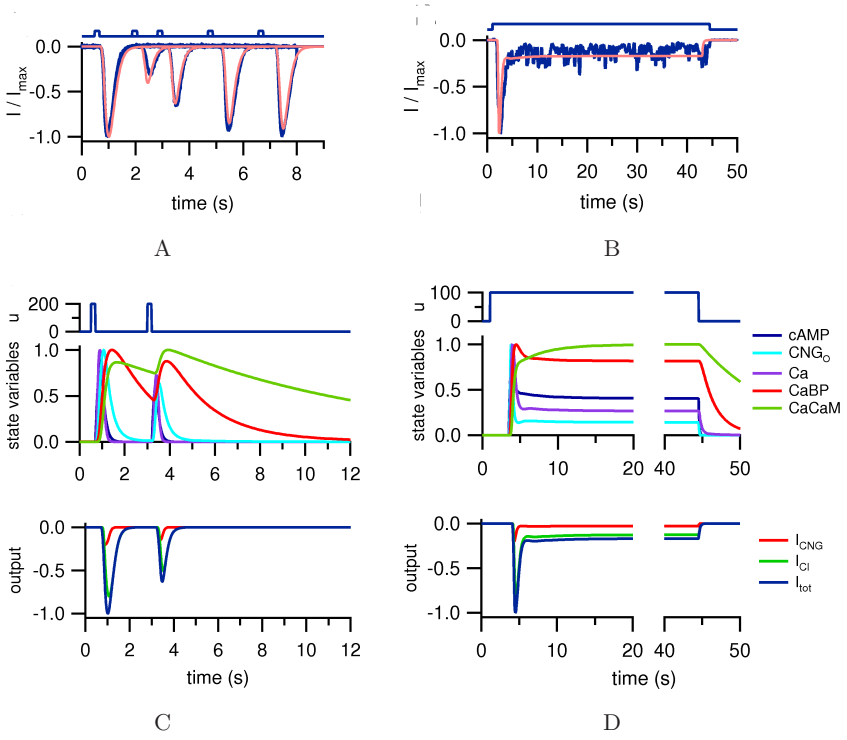

Figure 2.2: **Response to odorant.**(A) Response reductions by a conditioning pulse and their recovery time course in newt OSN (blue) and the corresponding fit of the model (red). The blue traces above the fit of the data represent the timing of the odorant stimulations. The amplitude of each response was normalized to the response to the first conditioning pulse. Two identical odorant stimuli of amyl acetate of 200 ms duration were applied separated by a time interval Δt of 2.5, 4.5 and 6.5 s. Experimental data drawn from [48]. (B) The response of a salamander OSN to an odorant stimulus sustained for 43.5 s. Experimental data adapted from [61]. (C) Corresponding simulated input, normalized state variables and output currents (with the two components I_{CNG} and I_{Cl}) for the pulse pair with $\Delta t = 2.5$ s shown in (A). (D) Simulated input, normalized state variables and output currents (I_{CNG} and I_{Cl}) for a sustained stimulus 43.5 s in duration.

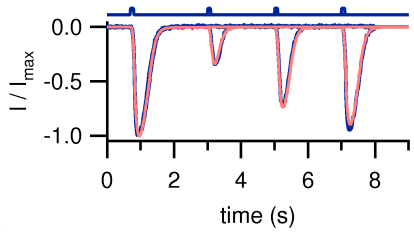

A

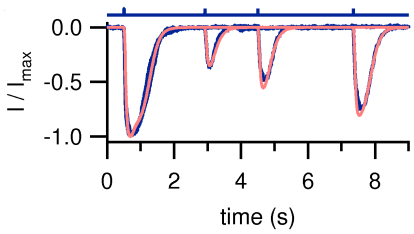

B

Figure 2.3: **Response to photorelease of caged cyclic nucleotides.** Response reductions by a conditioning pulse and their recovery time course in OSNs. The experimental data are shown in blue, the response of the model in red. Above each panel, the experimental input is shown (see Fig. 2.5 for the simulated input). In each panel, the amplitudes of the responses were normalized to the response to the first conditioning pulse. (A) Responses of a newt OSN to photorelease of cAMP by two identical 100 ms ultraviolet flashes, separated by increasing time intervals Δt of 2.3, 4.3 and 6.3 s. Experimental data adapted from [48]. (B) Responses of a mouse OSN to photorelease of 8-Br-cAMP obtained with two identical ultraviolet-light flashes of 1.5 ms separated by time intervals of 2.5, 4 and 6.8 s. Experimental data from [11].

(iii) Response to IBMX. Fig. 2.4 shows responses to applications of IBMX. Since IBMX reduces the activity of PDE, responses in the presence of IBMX are caused by the increase in cAMP concentration produced by the basal activity of AC. Stimulus onset is modeled with a rapid rise in u; its offset is modeled as a slow decay (see Fig. 2.6, and Fig. 2.11, Table 2.2 for an explanation). Fig. 2.4 A shows superimposed current recordings in response to pairs of brief stimuli with increasing Δt. Fig. 2.4 B shows the response of a neuron to a prolonged IBMX stimulation. The current response recovers to a low steady state level although the stimulus is maintained. Fig. 2.4 C shows the superimposed responses to two identical prolonged IBMX applications separated by Δt of 20 or 28 s. The current response to the first stimulus transiently increases and then decays to a steady-state during the sustained stimulus. The amplitude of the transient response to a second stimulus increases as Δt increases, as for the experiments shown in Figs. 2.2 A, 2.3 and 2.4 A.

2.4.2 Validation of the model

The agreement between parameter estimates across input types is quite good, despite the fact that different experimental techniques and animal species were used and despite the absence of step adaptation for two of the input types. This demonstrates that similar dynamics can account for all of the experimental time series we fit. In particular, the 4 parameter sets unanimously agree on the following relationship among degradation and dissociation rates: $0 < \lambda_2, \lambda_3 \ll \delta_2$. This corresponds to saying that the time constants of the feedback variables CaBP and CaCaM are much longer than that of free Ca.

Figure 2.2 C and D shows the temporal profile for the state variables from fits to data shown in Figure 2.2 A and B. The response of the open-loop part of the pathway, involving [cAMP], [CNG_o], and [Ca], is prompter than that of the feedback variables [CaBP] and [CaCaM], both in growth and decay. For multipulse adaptation, in particular, if the concentrations of CaBP and CaCaM are still above their basal levels when the second pulse arrives, the transient excursion of the pulse response of the open loop part is reduced because the feedback response is quicker. The result is that for both [CNG_o] and [Ca] the second pulse is attenuated with respect to the first. In the case of step adaptation in Fig. 2.2 B, the early response consists of a transient peak of [cAMP], [CNG_o] and [Ca]. As the concentration of the two feedback variables [CaBP] and [CaCaM] builds up, the corresponding negative feedbacks start influencing the dynamics of the open loop cascade, progressively

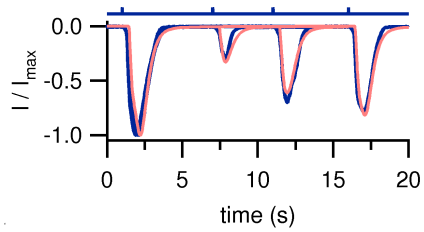

A

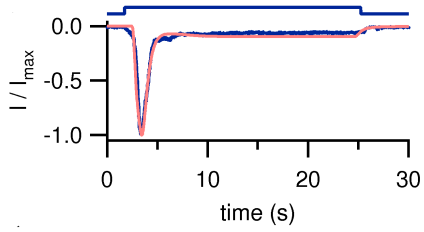

B

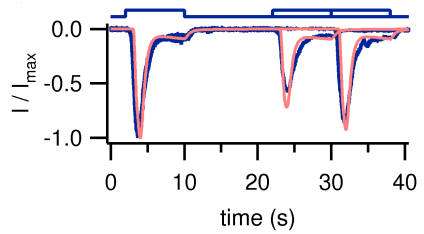

C

Figure 2.4: **Response to IBMX.** Responses of salamander OSNs to IBMX. The experimental data are represented in blue, the response of the model in red. Above each panel, the experimental input is shown (see Fig. 2.6 for the simulated input). (A) Responses to repeated applications of IBMX pulses of 20 ms applied to the cell at time intervals Δt of 6, 10, and 15 s. (B) Response to an IBMX stimulus applied for 24 s. (C) Responses to two subsequent prolonged IBMX stimuli of 8 s duration with interpulse interval of 20 and 28 s. IBMX was applied through a glass pipette controlled by a pressure ejection system. The concentration of IBMX in the pipette was 0.1 mM. Both kinds of adaptation are observed in the experiments and reproduced by the model: decline of the peak and convergence to a new adapted steady state within each stimulation, and peak amplitude modulation depending on the interstimuli lag time.

curtailing the transient excursion, until a steady state is reached. At this steady state, the concentration of the feedback variables is still high, while both [CNG_o] and [Ca] have returned near their basal levels. In turn, from Eqs (2.2.8)-(2.2.9) this implies that the output current returns near its basal level. Similarly, when the input step finishes, the open-loop variables drop to their basal levels much quicker than the feedback quantities.

For photorelease of 8-Br-cAMP, even if PDE activity is absent (no [CaCaM] feedback in the model, $k_1 = 0$), [CaBP] feedback is enough to guarantee multipulse adaptation (Fig. 2.3 B). However, a comparison between the models for cAMP and for 8-Br-cAMP photorelease data (Fig. 2.3 A and B) indicates that the joint action of both feedback mechanisms yields a more rapid recovery of the response. In the model, when the contribution of [CaCaM] is suppressed, the decaying phase of the cyclic nucleotide concentration becomes slower, modifying the kinetics of all the processes downstream (Figure 2.5).

Fig. 2.4 C illustrates a situation in which both types of adaptation are observed in response to IBMX stimulation. Given the dissociation rate constants for [CaBP] and [CaCaM] inferred from data, the recovery from multipulse adaptation is almost complete when Δt is 15 s or longer (Figs. 2.2 A and 2.4 A). In Fig. 2.4 C, however, Δt for the first pair of steps is 20 s but adaptation is still clearly visible, much more than when $\Delta t = 28$ s. This apparent discrepancy is interpretable in terms of the model of Eqs (2.2.1)-(2.2.7). During a step response, the feedback variables [CaBP] and [CaCaM] remain at high concentrations, and only after stimulus offset do they start to decrease (Figure 2.6). Hence essentially only the lag time between the end of the first step and the beginning of the second matters in determining the magnitude of multipulse adaptation.

While the shapes of the output responses plotted in Figures 2.2-2.4 are reproduced by the model fits with appreciable accuracy, their peak amplitude is sometimes not perfectly matched by the model (see Fig. 2.2 A). These errors are however within the range of experimental variability of the system.

2.4.3 Parameters estimation

The model of Eqs (2.2.1)-(2.2.9) contains 18 parameters (plus 5 describing the input profiles, see Table 2.2). These parameters are reported in Table 2.1. A priori knowledge on some of these parameters is available or can be inferred from other experiments. The parameters δ_1, λ_1 and γ_1 were previously estimated from experiments in low calcium conditions (see Fig. 2.7). k_c is drawn from [12, 31], and I_{max} is set equal to 1 because we considered normalized currents. The parameter $k_{1/2}$ is

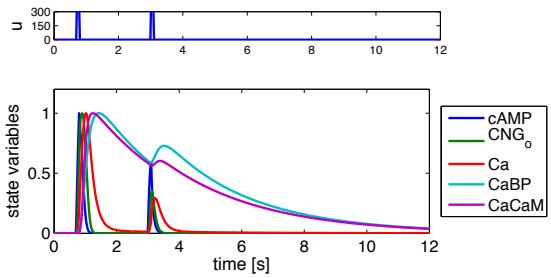

A

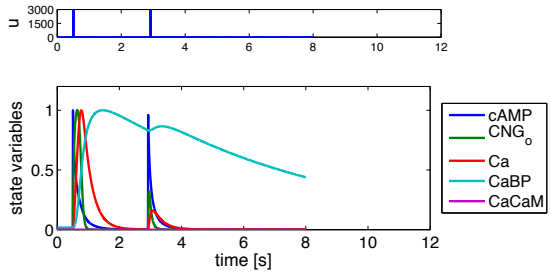

B

Figure 2.5: **Time profile of the state variables for the simulated data in response to caged compounds.** Panels (A) and (B) show the normalized simulation of the model in response to a paired-pulse stimulation using respectively caged cAMP and caged 8-Br-cAMP, corresponding to Fig. 2.3. For both figures, the upper panel represents the input given to the model.

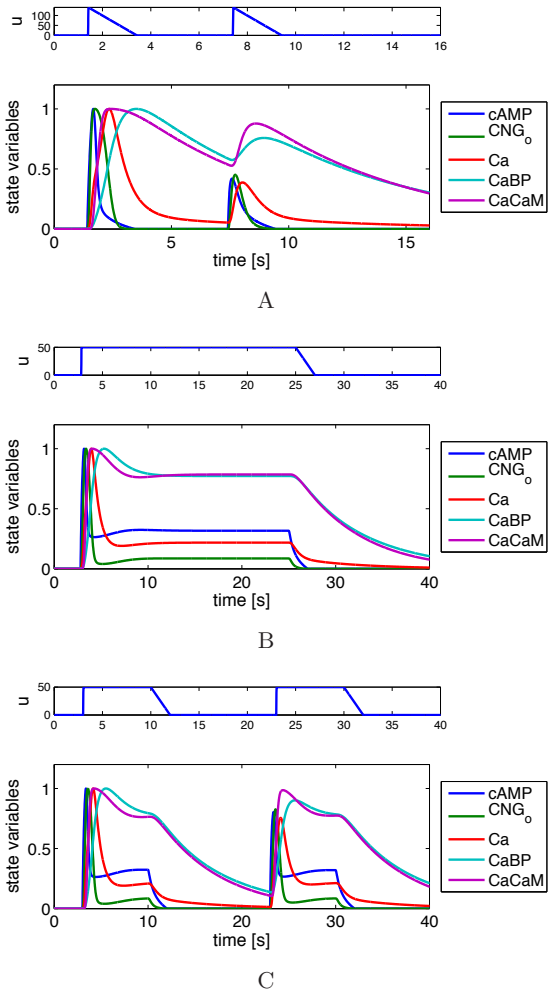

Figure 2.6: **Time profile of the state variables for the simulated data in response to IBMX.** Panels (A), (B) and (C) show the normalized simulation of the model in response to a paired-pulse stimulation, a prolonged stimulus, and a mixed stimulus, corresponding to the data of Fig. 2.4. The top panels on each figure represent the input given to the model.

constrained to be between 2 and 5 [11, 40], and the total concentration of calcium binding proteins [BP_{tot}] bound to CNG channels is constrained by its stoichiometric ratio with [CNG_{tot}]. The relative blockage B of the CaCaM feedback due to the action of IBMX was allowed to vary between 0.6 and 1.

In the equations for the current calculation (Eqs (2.2.8)-(2.2.9)), some of the parameters can be considered constant: $I_{max} = 1$ because of the current normalization; the exponent 2 represents the cooperativity of I_{Cl} [11, 40]; and $k_c = 0.2$ to reproduce a relative contribution of $\sim 20\%$ of the I_{CNG} in the total current [12, 31].

The experiments depicted in Figs. 2.2, 2.3, 2.4 were performed in different experimental conditions and therefore we subdivided them into 4 subsets, each corresponding to a choice of input stimulus (odorant, caged cAMP, 8-Br-cAMP and IBMX), and fitted 4 distinct sets of parameters. The fit was performed normalizing the amplitudes of the current responses. The starting point of the whole fitting procedure was a collection of experimental data obtained using 8-Br-cAMP stimulations of increasing amplitude, in positive potential conditions (thus with a reduced inflow of Ca^{2+}, if any, hence approximately in "open-loop" conditions) [11], see Fig. 2.7. In this way it was possible to obtain a good estimation of the association rate of cAMP and CNG channels, in our model represented by γ_1, of the corresponding dissociation constant λ_1 and of the degradation rate of cAMP δ_1. The input pulse amplitude and shape were assumed to be the same as those used in fitting the 8-Br-cAMP responses. Parameter values resulting from this fit were then used as the initial guesses for subsequent estimation of these parameters. The parameters were allowed to span from 0 to infinity with some exceptions: the intervals for the values of δ_1, λ_1 and γ_1 were restricted around the values previously found, and a lower bound equal to 0.1 was chosen for λ_2 and λ_3 to allow a complete recovery from adaptation of the response in about 30 seconds [11]. The other constrained parameter was $k_{1/2}$ appearing in the calculation of the chloride current: following the experimental data of [11, 40] it was allowed to vary between 2 and 5. The parameter B representing the relative inhibition of PDE due to the action of IBMX (see Subsection 2.4.4 for details) was considered only for the data obtained using IBMX, and was allowed to span from 0.6 to 1. All this a priori knowledge is reported in Table 2.1. Fits were performed using these initial values and constraints with the MATLAB function lsqcurvefit, which performs non-linear least squares (with a trust-region-reflective algorithm) simultaneously over the time series of each of the 4 experimental setups. The lsqcurvefit function finds the vector of coefficients $\mathbf{p}$ that

optimizes the following functional

$$J^* = \min_{\mathbf{p}} ||F(\mathbf{p}, \mathbf{t}) - \mathbf{y}||_2{}^2 = \min_{\mathbf{p}} \sum_i (F(\mathbf{p}, t_i) - y_i)^2 ,$$

where $\mathbf{t}$ represents the time vector, $\mathbf{y}$ the experimental data, and F($\mathbf{p}$,$\mathbf{t}$) the output of our model.

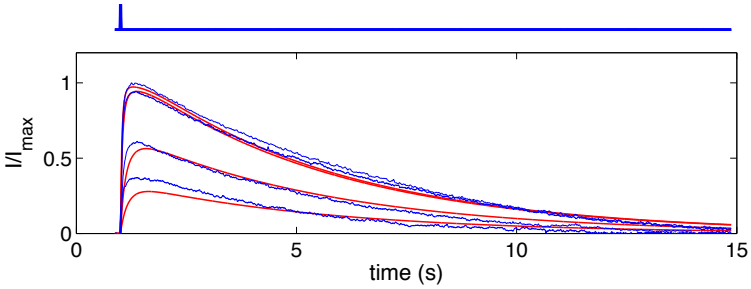

Figure 2.7: **Response to photorelease of caged cyclic nucleotides in a low Ca^{2+} experiment.** The experimental data are shown in blue, the response of the model in red. The blue traces above the data represent the experimental stimulus. Response of a mouse OSN to photorelease of 8-Br-cAMP with ultraviolet light flashes of 1.5 ms at various relative intensities (0.25, 0.4, 0.8 and 1), recording at +50mV in Ringer solution. Parameter estimates: $\delta_1 = 2.28$, $\lambda_1 = 0.21$, $\gamma_1 = 0.09$. Experimental data from [11].

The 4 parameter sets, reported in Table 2.1, show a substantial agreement. They are also in agreement with the parameter values one obtains performing a fit on all data simultaneously (column "common"). Since the model is nonlinear, no globally convergent fitting procedure exists. However, an extensive search over the space of parameters (see Subsection 2.4.5 and Fig. 2.12, 2.13) suggests that the parameter region which optimizes the least squares cost functional may be uniquely defined for most of the parameters. A notable exception is λ_3, the dissociation rate for the CaCaM feedback, whose value appears not to be univocally determined by the optimization procedure. No ambiguity is present in the 8-Br-cAMP responses, since in this case the CaCaM feedback is absent. We comment on this in the Discussion section.

Parameters estimation -Common fit for all experimental data The similarity among the 4 sets of parameters in Table 2.1 suggests that the experiments of Figures 2.2-2.4 can all be fit with a single set of parameters. When performing a si-

multaneous fit to all data sets (i)-(iii) (Table 2.1, last column; Figures 2.8, 2.9, 2.10), the agreement with the data is less precise than for fits to individual data sets. Nonetheless, the predicted output currents are still qualitatively correct, despite the fact that the experiments were performed in OSNs from different species and with different stimuli. This indicates that indeed the model captures the relevant aspects of olfactory adaptation.

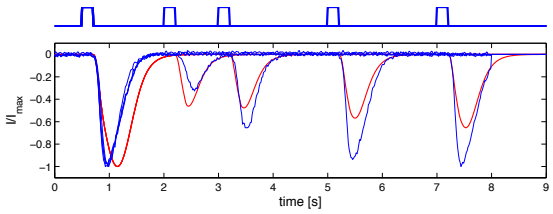

A

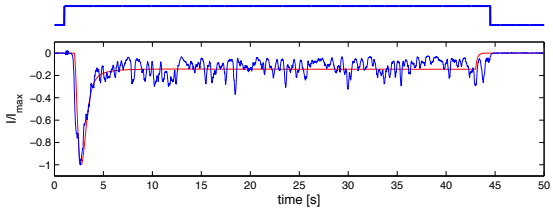

B

Figure 2.8: **Adaptation in response to an odorant.** Responses of the model (red) for the data shown in Fig. 2.16 (blue), using the parameter set in the "common" column of Table 2.1.

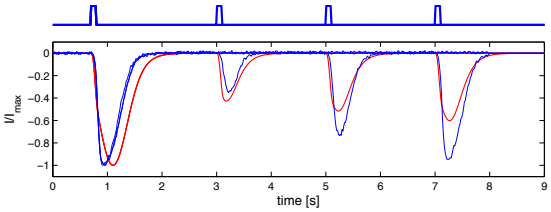

A

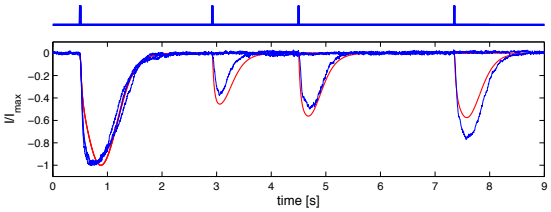

B

Figure 2.9: **Adaptation in response to caged compounds.** Responses of the model (red) for the data shown in Fig. 2.3 (blue), using the parameter set in the "common" column of Table 2.1.

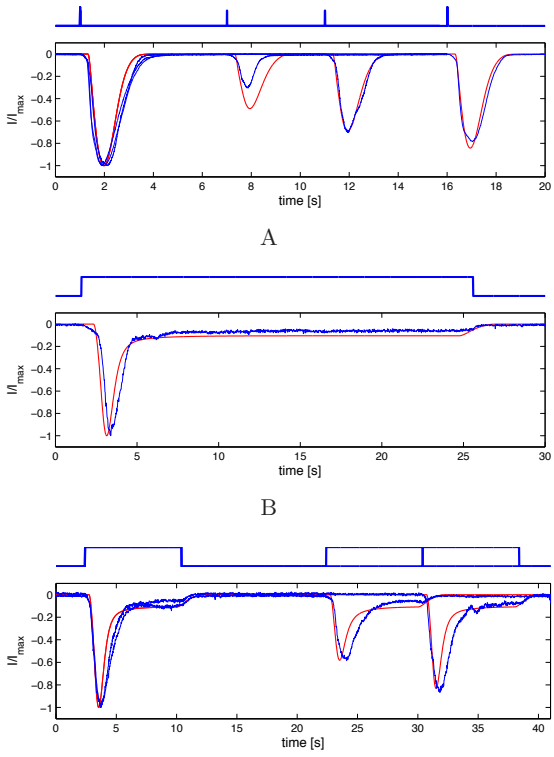

Figure 2.10: **Adaptation in response to IBMX.** Responses of the model (red) for the data shown in Fig. 2.4 (blue), using the parameter set in the "common" column of Table 2.1.

Table 2.1: **Parameter sets used to fit the data** The parameter names, meaning and values are reported. The parameter sets fit to the 4 input types are reported in the first 4 columns (see Fig. 2.2, 2.3, 2.4), while the fifth column contains the "common" parameter set, used to fit all the data simultaneously (see Fig. 2.8, 2.9 and 2.10, and the corresponding explanations). For the "common" column also the standard deviation (SD) is reported. The parameters with the largest error (k_1, γ_3 and $[CaM_{tot}]$) are all involved in the feedback loop of CaCaM. These uncertainties in the parameter estimation can be deduced also from the flat profiles of the cost function around the optimal values of the parameters in Fig. 2.12. It is a consequence of the redundancy of the two feedback loops. Errors are similar for the other parameter sets. In the last column, we collect all a priori information available on the parameters, as well as all constraints imposed in our fitting procedure. "low Ca exps" refers to parameters estimated in low-calcium experiments.

Name	Function	Odor	cAMP	8-Br-cAMP	IBMX	Common(SD)	Details
δ_1	degradation rate of cAMP/8-Br-cAMP	3.16	2.91	3.06	4.00	4.56 (0.03)	low Ca^{2+} exps
k_1	CaCaM feedback gain	47.02	29.57		49.98	12.58 (9.46)	
λ_1	dissociation rate between CNG and cAMP	0.63	0.33	0.33	0.22	1.82 (0.01)	low Ca^{2+} exps
γ_1	association rate between CNG and cAMP	0.08	0.04	0.09	0.09	0.06 (0.0003)	low Ca^{2+} exps
k_2	CaBP feedback gain	163.17	87.01	84.17	134.22	181.39 (19.56)	
ϕ_1	inflow of Ca^{2+} through CNG channels	47.29	55.85	36.80	15.46	13.50 (0.41)	
δ_2	outflow of Ca^{2+}	3.32	5.07	3.48	1.35	2.98 (0.03)	
γ_2	association rate of Ca^{2+} and BP	0.84	0.30	0.14	0.10	0.16 (0.005)	
λ_2	dissociation rate of CaBP	0.60	0.42	0.16	0.25	0.12 (0.001)	≥ 0.1
γ_3	association rate of Ca^{2+} and CaM	0.01	0.21		1.00	0.01 (0.05)	
λ_3	dissociation rate of CaCaM	0.10	0.33		0.20	0.10 (0.03)	≥ 0.1
k_c	percentage of I_{CNG} in the total current	0.2					[12, 31]
I_{max}	maximum amplitude of the total current	1					normalized
$k_{1/2}$	half-maximum activation of I_{Cl} due to Ca^{2+}	4.03	2.91	3.60	4.34	4.92 (0.13)	[11, 40]
B	relative blockage due to IBMX				0.75	0.60 (0.09)	≥ 0.6
$[CNG_{tot}]$	tot concentration of CNG channels	0.74	1.22	5.72	1.00	1.10 (0.01)	
$[BP_{tot}]$	tot concentration of Ca-binding protein	0.74	1.19	1.33	1.00	1.10 (0.01)	$\leq 2[CNG_{tot}]$
$[CaM_{tot}]$	tot concentration of calciumcalmodulin	1.30	0.84	1.00	1.50	0.68 (2.82)	

2.4.4 Modeling the input stimulus

The shape of the input u in Eq. (2.2.1) for [cAMP] changes with the type of stimulation considered. We reported in Fig. 2.11 and in Table 2.2 the shape and the parameter values for the different simulated inputs. The plot of the profiles can be seen above those of the state variables in Fig. 2.2, 2.5 and 2.6. For odorant molecules and caged compounds, we chose a step-like function to represent the shape of the input, assuming fast kinetics for both release and termination of the stimulation. We imposed a total inhibition of the action of PDE in the data obtained using 8-Br-cAMP (the CaCaM feedback gain $k_1 = 0$ in this case). To model the experimental data with IBMX as input, we instead used a ramp-like form for input onset and offset, because of the different mechanism of stimulation: IBMX suppresses part of the basal activity of PDE, directly leading to an increasing amount of cAMP. For this type of data the rise is steeper than the decay, with a rise duration equal to 0.02 s (corresponding to the experimental duration of the stimulus) and a decreasing duration equal to 2 s for the stimulation representing multipulse adaptation, while we used a 0.02 s increase followed by a constant amplitude, and by a 2 second-ramp decrease to represent the longer stimuli (see Fig. 2.11 and Table 2.2 for details). Furthermore a dedicated parameter B was added in the fitting procedure to represent the relative inhibition of the CaCaM feedback due to the action of the PDE (the parameter k_1 in the equations was multiplied by 1-B). The $\sim$75% inhibition of PDE by IBMX obtained by the parameter estimation (see Table 2.1) seems to be a reasonable value and gives a good fit to the experimental data. A delay of the response, varying between 0.2 and 1 s, was added to represent the latency (in this case considered as the time required by the first part of the transduction process, upstream of cAMP production) in the fit of the responses to odorants or to IBMX. Such a delay was not added to the input profile for experiments using caged compounds, in which the photorelease of cyclic nucleotides is very fast and produced a rapid response (Fig. 2.3).

2.4.5 Evaluation of the goodness of the fit

We performed several tests to evaluate the goodness of the parameter estimation. First of all we tested if the parameters we obtained from the fitting procedure were in correspondence of a local minimum. We moved each parameter around its estimated value up to a 10 fold increase/decrease or until the cost function increases more than 10% of its optimum J^*. In Fig. 2.12 the corresponding results for the entire set of parameters are shown (J^* is plotted in red) for the case of "common" parameter set

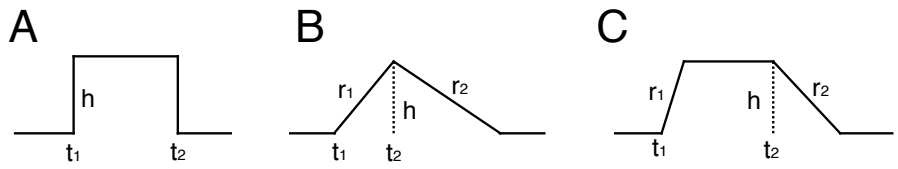

Figure 2.11: **Profiles of the shapes of the simulated inputs.** The profile A is used to simulate the response to odor, cAMP and 8-Br-cAMP, B is for the IBMX pulses, and C for the sustained stimuli of IBMX.

Table 2.2: Details of the simulated inputs. The shape corresponds to one of the three profiles represented in Fig. 2.11. h represents the amplitude of the stimulus, r_1 and r_2 represent the slopes of the profiles. All the time units are expressed in s.

	type	shape	h	(t2-t1)	delay	r_1	r_2
odor	pulses	A	200	0.2	0.2		
	sustained	A	100	43.5	1		
cAMP	pulses	A	300	0.1	0		
8-Br-cAMP	pulses	A	3000	0.005	0		
IBMX	pulses	B	140	0.02	0.3	7000	70
	sustained	C	50	24	1	2500	25
	sustained double	C	50	8	0.7	2500	25

of Table 2.1. The only two parameters for which the cost function decreases with respect to J^* are the dissociation rate λ_3 and the fractional blockage B of the CaCaM feedback in the IBMX experiments. In both cases, the variations improving on J^* are outside the range we allowed for the parameters. In particular, the lower bound we imposed in λ_3, namely 0.1, is due to the fact that in experiments a complete recovery from multipulse adaptation occurs in at most 30 s. This constrains the time constants of the feedbacks. Notice in Fig. 2.12 that a similar behavior does not occur for λ_2. The interpretation of this fact is straightforward: when λ_2 is kept fixed at the optimal value, the CaCaM feedback is largely redundant and it is allowed to behave as an exact integral since the CaBP feedback loop already takes care of shaping the closed-loop system as required. To confirm that this is indeed the case, we have carried out extensive simulations varying simultaneously the two dissociation rates λ_2 and λ_3 for the feedback variables. In no case did λ_2 and λ_3 assume too small values simultaneously while reproducing correctly the input-output adaptation profiles. As for the B parameter, the minimum blockage of 60% which we impose on the IBMX experiments is reasonable, given our current knowledge of the action of this blocker on PDE. Hence, in this case, the (marginal) improvement of J^* shown in Fig. 2.12 is to be considered non-physiological. The pattern of single parameter variations is similar on the odor experiments (B does not appear in this case) and in the IBMX data. No improvement at all appears in the 8-Br-cAMP data set.

While the local analysis carried out above is encouraging, due to the nonlinearities in the dynamics, our parameter fitting procedure is not guaranteed to find a global optimum. We tried anyway to explore the landscape of the parameter space from a more global perspective (see Fig. 2.13). We considered for this kind of test the parameter set obtained for the fit of the responses to odor (the behavior for the other sets is similar). For each parameter we randomly sampled rescaling factors across 4 orders of magnitude ($10^{-2} \div 10^{2}$), combining the rescaled parameters in various ways, at random. We then use these values as starting points for the parameter estimation. Fig. 2.13 A shows that when the procedure is repeated about 100 times a cost function smaller than J^* is never obtained. In the best suboptimal solutions we found (drawn in red in Fig. 2.13 A) we verified that indeed at least one of the two feedback dissociation rates is small compared to the other reaction rates. This confirms that in a model like ours the slow dynamics of the feedback is fundamental to reproduce adaptation, and supports our observation that the two feedback loops perform this task in a redundant way.

In order to evaluate how rugged the parameter landscape is, and to estimate how well our fitting procedure performs (the two aspects are linked and cannot

be disentangled easily), in Fig. 2.13 A the initial parameter guess and the final (suboptimal) parameter set are shown connected by a line. The distance D in parameter space is calculated as

$$D = ||\mathbf{p}^* - \hat{\mathbf{p}}||_2 = \sqrt{\sum_i \left(p_i^* - \hat{p_i}\right)^2},$$

where $\mathbf{p}^*$ is the parameter vector corresponding to J^*, and $\hat{\mathbf{p}}$ the parameter vector of the current suboptimal fitting. Every segment connects a random starting point with the final result $\hat{\mathbf{p}}$ (indicated with a star in the plot). It is possible to see that a diminishing difference in the cost function corresponds to a diminishing distance in the parameters, suggesting the idea of a landscape in the cost function with a unique region for the minimum, surrounded by a large amount of local minima at higher cost.

To increase the sample size, we repeated about 1000 times a similar procedure without re-fitting the parameters but only evaluating the cost function on a random choice of the parameters, see Fig. 2.13 B. For each sampled parameter vector we calculated the cost function and the distance from $\mathbf{p}^*$. No value found in this way appears below J^*, and it is possible to notice how increasing the distance in parameter space from $\mathbf{p}^*$ tends to increase the cost function, suggesting that the basin of attraction of our minimum could be quite large (thereby confirming the result of Fig. 2.13 A).

2.4.6 Dose response relations

The model presented here is able to reproduce the shift in the dynamic range caused by adaptation in the olfactory transduction pathway. The typical illustration of this feature is the dose-response curve. In this curve, the normalized maximal amplitude of the current response is plotted versus the relative input amplitude or input duration. Following adaptation, the input amplitude interval over which the curve is approximately linear (the system is responding but not saturating) is shifted and broader, allowing better detection and discrimination of further stimulations. We present here the response of our model to two different simulated stimuli. In Fig. 2.14 A it is possible to see the dose-response curves of the model in the case of odor stimulation (with stimulus duration on the x-axis) and in Fig. 2.14 B in the case of photoreleased 8-Br-cAMP (with stimulus amplitude on the x-axis). Comparing the shape of these curves with those obtained experimentally (for the type of data we are considering see [11, 48]) it is apparent that the qualitative behavior is very

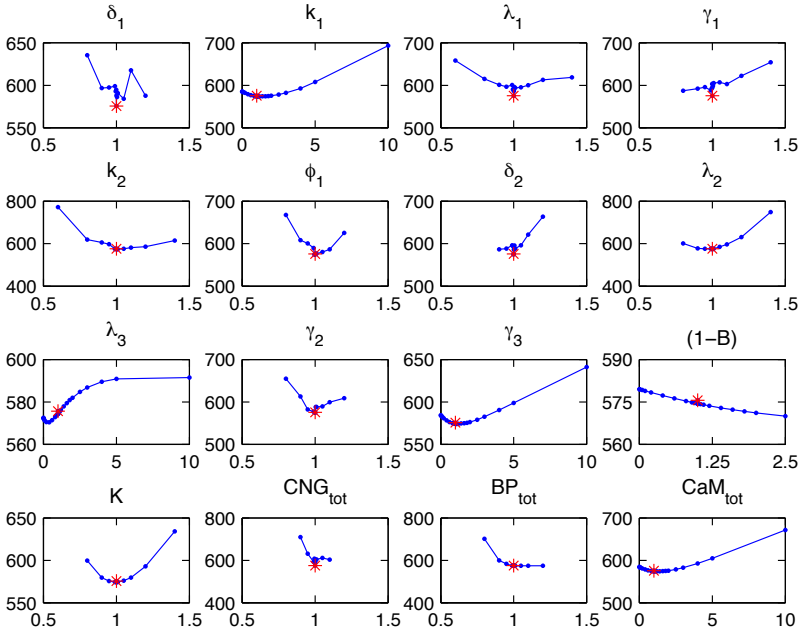

Figure 2.12: **Goodness of fit: testing local optimality in the neighborhood of $\mathbf{p}^*$.** Sensitivity of the cost function to single-parameter perturbations. On the x-axis the relative value of each parameter with respect to its optimal value is reported, on the y-axis the corresponding value of the cost function. $\mathbf{p}^*$ is shown in red.

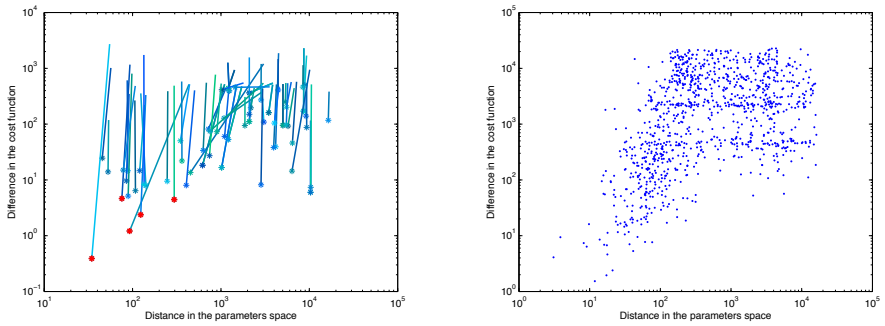

A B

Figure 2.13: **Goodness of fit: exploring the landscape of the cost function.** (A) Starting from random points and optimizing. On the x-axis the distance in the space of parameters is reported, on the y-axis distance from J* of the cost function, both in a logarithmic scale. The segments connect the random starting points and the optimized $\hat{\mathbf{p}}$ (denoted with a star). The red points indicate fitting results with a difference smaller than 5 from the cost function of the optimal solution. All the $\hat{\mathbf{p}}$ very close to $\mathbf{p}^*$ in terms of cost function have similar feedback time constants as our $\mathbf{p}^*$ parameter set. (B) Evaluation of the cost function for a random choice of parameters. On the x-axis the distance in the space of parameters is reported, on the y-axis the difference in the cost function, both in a logarithmic scale.

similar. The typical sigmoidal shape for the activation of both the control and the adapted responses, and the reduction of the distance between the two curves with increasing input are correctly reproduced. We fit these simulated data with a Hill-type function: $Y = \frac{X^n}{X^n + {K_{1/2}}^n}$ where X represents the input duration or amplitude and Y is the value of the current peak in the control or adapted state. The values for the cooperativity index n and for the half-activation constant $K_{1/2}$ are reported in Tab. 2.3.

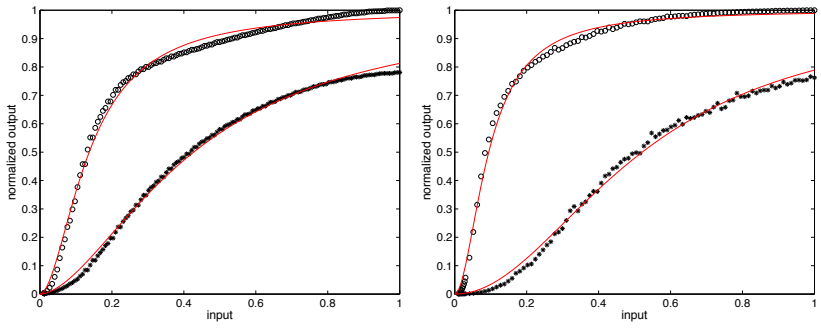

A B

Figure 2.14: **Dose response plot.** (A) Simulated odorant response: the black dots represent the model simulation, the red curve shows the corresponding Hill function. For the response to the first pulse, an input of increasing duration was simulated. To obtain the adapted response, the duration of the second pulse was increased, keeping fixed that of the first pulse. (B) Same as (A), but using simulated responses to a release of caged 8-Br-cAMP of increasing amplitude.

Table 2.3: Parameter set used to fit the dose response curves of Fig. 2.14.

Type of stimulation		n	$K_{1/2}$
odor	control	1.83	0.14
	adapted	1.73	0.43
8-Br-cAMP	control	1.90	0.09
	adapted	2.02	0.52

2.4.7 An alternative model for the CNG channel

In this subsection we formulate a possible alternative model for the gating of a CNG channel inspired by [76], and show that also in this case the input-output behavior

is qualitatively correct. Following [76] a different formulation of the model can be considered, in which the state of a CNG channel is characterized by 3 possible conformations:

- open (hereafter $[CNG_o]$)
- closed ($[CNG_c]$)
- inhibited ($[CNG_i]$)

The inhibited state of the CNG channel resembles the inactivated state of the voltage-gated Na^+ channel, in which after depolarization, the channel is in a non-conductive state and remains refractive to further gate opening commands for a certain time interval. Although to our knowledge there is no experimental evidence to support the existence of an "inhibited" phase in CNG channels during voltage-clamp, the scheme can be used to set up a theoretical model alternative to Eqs (2.2.1)-(2.2.7). In this scheme, the variable [CaBP] no longer appears: the binding of Ca to BP (permanently attached to the channel) automatically turns an open channel into an inhibited channel (second reactions of the list below). The longer time constant associated with the feedback action of the CaBP in the model (2.2.1)-(2.2.7) is replaced here by the longer time constant of the "inhibited" phase with respect to the other two phases of the CNG channel. The reactions are therefore as follows:

$$
\begin{gathered}
2\ \mathrm{cAMP} + \mathrm{CNG_c} \underset{\lambda_1}{\overset{\gamma_1}{\rightleftharpoons}} \mathrm{CNG_o} \\
\mathrm{CNG_o} + 2\ \mathrm{Ca^{2+}} \xrightarrow{\gamma_2} \mathrm{CNG_i} + 2\ \mathrm{cAMP} \\
\mathrm{CNG_i} \xrightarrow{\lambda_2} \mathrm{CNG_c} + 2\ \mathrm{Ca^{2+}} \\
2\ \mathrm{Ca^{2+}} + \mathrm{CaM} \underset{\lambda_3}{\overset{\gamma_3}{\rightleftharpoons}} \mathrm{CaCaM} \\
\mathrm{cAMP} \xrightarrow{k_1 \cdot CaCaM + \delta_1} \mathrm{AMP}
\end{gathered}
$$

with the following conservation laws:

$$
\begin{aligned}
[\mathrm{CNG_{tot}}] &= [\mathrm{CNG_o}] + [\mathrm{CNG_c}] + [\mathrm{CNG_i}]; \\
[\mathrm{CaM_{tot}}] &= [\mathrm{CaM}] + [\mathrm{CaCaM}].
\end{aligned}
$$

Adding a factor σ=volume/surface to allow the interaction between surface and volume concentrations of variables, the reactions above lead to the equations:

$$\begin{aligned}
\frac{d[\mathrm{cAMP}]}{dt} &= 2\cdot\frac{1}{\sigma}\cdot\lambda_1\cdot[\mathrm{CNG_o}] - 2\cdot\frac{1}{\sigma}\cdot\gamma_1\cdot[\mathrm{cAMP}]^2\cdot([\mathrm{CNG_{tot}}]-[\mathrm{CNG_o}]-[\mathrm{CNG_i}]) \\
&\quad -(\mathrm{k}_1\cdot[\mathrm{CaCaM}]+\delta_1)\cdot[\mathrm{cAMP}] + 2\cdot\frac{1}{\sigma}\cdot\gamma_2\cdot[\mathrm{Ca}]^2\cdot[\mathrm{CNG_o}] + \mathrm{u} \qquad (2.4.10) \\
\frac{d[\mathrm{CNG_o}]}{dt} &= \gamma_1\cdot[\mathrm{cAMP}]^2\cdot([\mathrm{CNG_{tot}}]-[\mathrm{CNG_o}]-[\mathrm{CNG_i}]) \\
&\quad -\lambda_1\cdot[\mathrm{CNG_o}] - \gamma_2\cdot[\mathrm{Ca}]^2\cdot[\mathrm{CNG_o}] \qquad (2.4.11) \\
\frac{d[\mathrm{Ca}]}{dt} &= \phi_1\cdot\frac{1}{\sigma}\cdot[\mathrm{CNG_o}] - \delta_2\cdot[\mathrm{Ca}] - 2\cdot\frac{1}{\sigma}\cdot\gamma_2\cdot[\mathrm{Ca}]^2\cdot[\mathrm{CNG_o}] + 2\cdot\frac{1}{\sigma}\cdot\lambda_2\cdot[\mathrm{CNG_i}] \\
&\quad -2\cdot\gamma_3\cdot[\mathrm{Ca}]^2\cdot([\mathrm{CaM_{tot}}]-[\mathrm{CaCaM}]) + 2\cdot\lambda_3\cdot[\mathrm{CaCaM}] \qquad (2.4.12) \\
\frac{d[\mathrm{CNG_i}]}{dt} &= \gamma_2\cdot[\mathrm{Ca}]^2\cdot[\mathrm{CNG_o}] - \lambda_2\cdot[\mathrm{CNG_i}] \qquad (2.4.13) \\
\frac{d[\mathrm{CaCaM}]}{dt} &= \gamma_3\cdot[\mathrm{Ca}]^2\cdot([\mathrm{CaM_{tot}}]-[\mathrm{CaCaM}]) - \lambda_3\cdot[\mathrm{CaCaM}] \qquad (2.4.14)
\end{aligned}$$

Hypothesizing slow dynamics for the $[\mathrm{CNG_i}]$ and [CaCaM] variables this model is able to reproduce both types of adaptation observed in the olfactory transduction (Fig. 2.15).

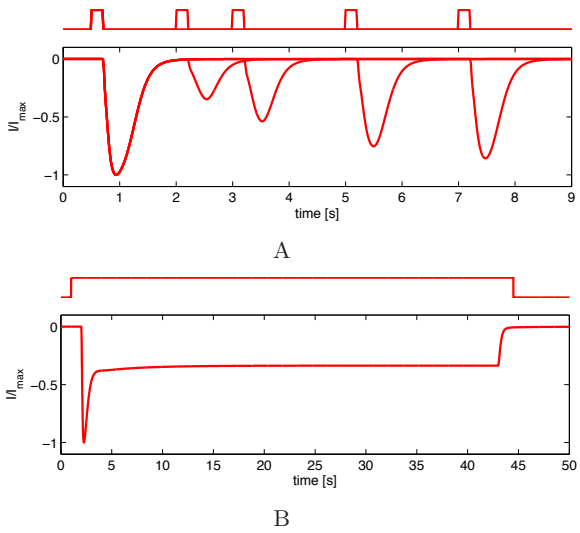

Figure 2.15: **3-conformation model for the CNG channel.** Panel (A) shows the response of the model of Eqs (2.4.10)-(2.4.14) to a double pulses protocol. Panel (B) shows the response on the same model in the case of a sustained stimulation.

In this model, the binding of Ca to BP (and hence the initiation of the inhibition phase) coincides with the detachment of cAMP (and hence with the termination of the opening gate signal). In the model (2.2.1)-(2.2.7), the two gating commands are instead independent and can coexist, which seems to us a more appropriate description for this population of channels. Furthermore the profile of a dose-response curve cannot be reproduced by Eqs (2.2.1)-(2.2.7). Finally the behavior in the adapted state is different in the two models. Indeed, in the case of a saturating input a model like (2.4.10)-(2.4.14) provides right after the stimulus a total inhibition (and unavailability) of the CNG channels. Therefore this system is unable to respond to subsequent stimuli, until the channels have turned from the inhibited to a closed state. On the contrary, in the system of Eqs (2.2.1)-(2.2.7) the CNG channels are still able to produce a response, although reduced due to the feedback action of the calcium binding protein complex.

Notice that also for this model in nominally zero Ca^{2+} the channels never become inhibited, hence both feedback mechanisms are absent, consistently with the experimental data.

2.5 Discussion

The aim of this work is to formulate a basic model for adaptation in OSNs, able to capture all the kinetic features observed in the experiments and to provide a dynamical interpretation of the phenomenon. The main result is that both multipulse and step adaptation can be explained by the same assumption, namely that the dynamics of the feedback part of the pathway are much slower than those of the open-loop part. As mentioned in the Section 2.1 this scheme corresponds to an integral feedback with memory decay. That such a scheme can account for both types of adaptation is shown by best-fits of a kinetic model to experimental data.

One of the main predictions of our model is that the two forms of adaptation are in a dynamical trade-off: when the time constant of the feedback part becomes infinite and step adaptation is exact, then the recovery in multipulse adaptation vanishes, thus the second pulse will have reduced amplitude for any interpulse interval (see Figure 2.16 A and B). In terms of the model of Eqs (2.2.1)-(2.2.7), a long feedback time constant means that the Ca-activated protein complexes responsible for the feedback are long lived after the first pulse. Upon the arrival of a second pulse, their concentration is still high and the feedback-induced response attenuation is more rapid. When the feedback time constants are comparable to those of the open-loop part (Figure 2.16 C and D), then these complexes have time to dissociate

before the arrival of the next pulse, and the response attenuation is diminished. For prolonged stimuli, the difference between the feedback and open-loop time constants determines the degree of adaptation.

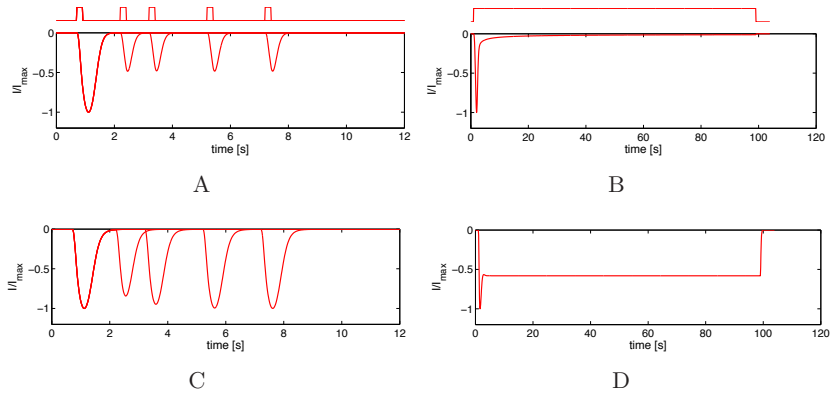

Figure 2.16: **Dynamical trade-off: comparison between perfect adaptation and fast dissociation of CaCaM and CaBP.** Left: Response to double pulses in the case of perfect adaptation (dissociation rates for the feedback variables, λ_2 and λ_3, equal to zero) in panel (A) and in the case of fast kinetics of the feedback variables in panel (C). The lag time for the recovery of the response is overestimated in the first case (for perfect adaptation there is no recovery) and underestimated in the second case. Right: Response to a sustained stimulation for zero (B) and fast (D) feedback kinetics rates. In the first case the pre-stimulus current recovers exactly during the stimulation (hence the name perfect adaptation) while in the second case the system adapts less than observed experimentally.

In a model like that of Eqs (2.2.1)-(2.2.7), a natural way to obtain slow dynamics for a state variable is to choose a time constant which is long (longer than the other time constants of the system), and feedback loops are natural candidates for slower kinetics, especially in the presence of output responses exhibiting only a transient excursion as in step adaptation. For our adaptation experiments, the identification of two slow variables appears to be confirmed by the agreement of fits performed independently on 4 data sets: all of them implicate CaBP- and CaCaM-mediated feedback as candidates. The high correlation among the 4 sets of parameters in Table 2.1 and the qualitatively correct fit obtained from simultaneous fitting of all 4 data sets emphasize that all of the experimental results we have presented can be accounted for by one model and that the trade-off mentioned earlier leaves only a limited parameter range compatible with both types of adaptation. Other

well-known features of adaptation, such as the dose-response shift, are qualitatively reproduced by the model with best-fit parameters (Figure 2.14 and Table 2.3). Also the slow attenuation of the current response following a transient input in low extracellular Ca^{2+} is replicated by the Eqs (2.2.1)-(2.2.7) when the amount of Ca is set equal to zero (Figure 2.7).

Other models for olfactory transduction have been published in recent years [22, 33, 76]. In [22] for instance, the authors focus on modeling multiple aspects of the kinetics, such as the plateau phase of the pulse response appearing on (some) high amplitude stimuli, and the onset of oscillations for step responses (see also the model in [76]), from experiments using the suction-pipette technique [79, 81]. Neither of these features is present in the voltage-clamp experiments described here (the oscillations visible in the step adaptation of Fig. 2.2 are very small and irregular). In [22], capturing such complex phenomena requires a much more complicated model, with several nonlinear kinetic functional forms and several more parameters than the model developed here. This makes it more difficult to understand which basic mechanisms are responsible for adaptation. The model of [76] instead represents an ionic channel with a 3-conformation model: open, closed and inhibited, the last corresponding to a non conductive channel. In this model, the binding of Ca^{2+} to the Ca-binding proteins present on the channel, initiates a refractory period in which the channel has lost sensitivity to cAMP and cannot reopen. This mechanism, in a way similar to what happens during the repolarization phase in models of neuronal action potentials, is described in detail in Subsection 2.4.7 (see also Figure 2.15). The duration of the refractory period plays the same role as the long (feedback) time constant in a model like that of Eqs (2.2.1)-(2.2.7).

As for adaptation in general, many mathematical models have been proposed in recent years [1, 2, 8, 28, 100, 107]. These are however exclusively concerned with step adaptation, and, as the exact integral feedback model shows, they may not manifest both forms of adaptation observed in olfactory transduction. From a kinetic point of view, the integral feedback model corresponds to a time constant which is infinite and induces an exact recovery to the pre-stimulus level (a perfect step adaptation), never observed in voltage-clamp measurements of olfactory transduction. That the inexact adaptation in our measurements is not an artifact is confirmed by the fact that the steady state displacement scales with the amplitude of the step input (see for example Fig. 1 of [61]). This property is not observed in perfect step adaptation which is instead independent of input size - the displacement converges to zero for all amplitudes of the input step. Note that a dependence of the steady state displacement on the amplitude of the constant input is captured by our model (Figure 2.17).

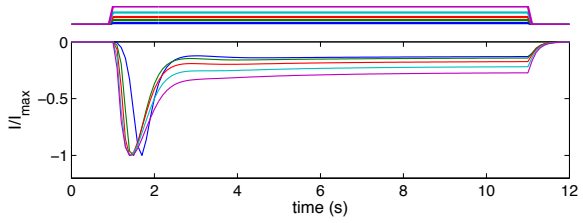

Figure 2.17: **Current responses to a prolonged stimulation of different amplitudes.** Responses are normalized to the amplitude of the transient peak. Increasing inputs yield increasing steady-state levels. This shows that for our model the lack of exact adaptation is not an "error" but a steady-state characteristic, incompatible with models of perfect adaptation. The green trace corresponds to the simulation in Fig. 2.2.

In spite of these differences, a common principle in many adaptation models, namely that adaptation is the result of multiple time scales acting on a system [2, 28], also guides our work. In the context of olfactory transduction, previous studies [55] have suggested that a slower kinetic is due to the action of CaMKII on AC, and that each form of adaptation is due to a different feedback [108]. Our model suggests instead that a feedback on AC is not necessary and that, rather than a neat association of each form of adaptation to a particular feedback mechanism, there is a redundancy in the regulation, with each feedback contributing to both types of adaptation and only a marginal synergistic effect observable from their joint action. In our model this redundancy is highlighted by the observation that the only parameter which can be modified significantly without altering the quality of the fit is λ_3 (the dissociation rate of the CaCaM feedback). Provided that the time constant of the kinetics of the CaBP feedback is kept in the correct time window (i.e. slower than the time constant of Ca but fast enough to avoid perfect adaptation), λ_3 can be modified without drastically altering the closed loop behavior. While a redundant role for the two feedback loops is a plausible hypothesis, its complete experimental validation is still unfeasible. In fact, if the CaCaM feedback loop can be blocked (as in our 8-Br-cAMP experiments), the blockage of the CaBP regulation requires the knowledge of all gating proteins naturally bound to the CNG channel, an information which is still out of reach.

Chapter 3

Basic dynamical models explaining adaptation in olfactory sensory neurons and photoreceptors

3.1 Background

A common trait of most sensory neurons in vertebrates is their capacity to *adapt* to changes of the input signal being monitored. As already mentioned adaptation in this context is intended as the ability of the sensory cell to shift the window of amplitudes in which the signal is accurately detected without incurring in saturation-induced distortions. Physiological recordings have identified the phenomenon in olfactory receptors [48], retinal photoreceptors [74], auditory [20] and somatosensory neurons [58]. In this chapter we focus on the first two such sensory systems, olfactory transduction and phototransduction. If it is commonly accepted that the mechanisms inducing adaptation in sensory receptor cells are those involved in the homeostatic regulation of the signaling pathways [60, 74], there is still no commonly accepted explanation of how this function is performed. In spite of a wealth of knowledge available at the level of molecular components and of reaction mechanisms for the signaling cascades involved and for their regulation (see the Introduction and e.g. [15, 23, 40, 73] for comprehensive surveys of olfactory transduction and phototransduction), what is still missing (and difficult to obtain) is a complete understanding of how the various steps are orchestrated into a coherent behavior at system-level. Our

aim in this work is to combine mathematical modeling and single cell electrophysiological experiments, in particular input-output (i.e., stimulus-response) time series, to thoroughly understand a number of dynamical features which can be associated with sensory adaptation, thereby helping understanding how this phenomenon happens.

The ability of a biological system to adjust the sensitivity in a wide range of input amplitudes, has been extensively studied in the literature [41, 43, 44, 98], especially in recent years [2, 7, 8, 28, 36, 37, 57, 91, 100, 107]. The phenomenon occurs in different contexts, like chemotaxis in bacteria [2, 107] and amoeba [36], osmotic regulation in yeast [64], tryptophan regulation in *E.coli* [102], and sensory systems [41, 98]. Most, if not all, of these studies evaluate adaptation through the steady state values reached in response to different constant stimuli. When one is concerned only with steady states and their variations, then the only form of adaptation which can be studied is what we call *step adaptation*. This dynamical behavior is also known as desensitization in the literature [41] and corresponds to a response that terminates or attenuates in spite of a persistent stimulation. Following [44], step adaptation is called *perfect* ("absolute" in [44]) in the first case, and *partial* in the second. From a modeling perspective, the perfect adaptation case is of particular interest, because it entails the presence of a particular form of regulation known in control theory as integral feedback [107]. Perfect step adaptation means that, regardless of the amplitude of the input step being applied, the system is able to recover exactly the nominal value it had before the stimulus.

If, as in our sensory systems, we are able to apply a richer class of input profiles than just steps, then more features than simply steady state responses can be studied. From a dynamical perspective, in fact, the stimulation with time-varying input protocols provides information which is nonredundant with the steady state responses. Combining this with the possibility of monitoring precisely the entire time history of a response, then more fine-graded hypotheses on the regulatory mechanisms encoded in the pathways can be formulated theoretically and validated (or falsified) experimentally. For instance, if in a system with integral feedback instead of steps we apply a pair of nonoverlapping pulses, no difference should emerge in the elicited responses as we progressively increase the delay of the second pulse with respect to the first. This is not what happens in sensory systems: if for short delays between the pulses adaptation manifests itself in a reduced amplitude of the transient response to the second pulse, increasing the lag time adaptation progressively reduces, until the system recovers completely, i.e., the two pulses elicit identical responses. This effect, which we call *multipulse adaptation*, translates into an integral feedback which cannot be perfect, but which has to "forget" the past with a cer-

tain time constant. Exact integral feedback (which corresponds to an infinite time constant) cannot achieve this, but a dynamical feedback with a suitable memory decay can accomplish the task. However, replacing an exact integral feedback with a dynamical feedback having a memory decay implies that perfect step adaptation is no longer possible. Also this prediction is coherent with the experiments. In both sensory systems, in fact, the step responses reset themselves only partially, never completely. While the gap is minimal in the olfactory neurons, it is consistent in phototransduction, see Fig. 3.1 A and Fig. 3.2 A.

In the previous chapter we have observed that the two forms of adaptation mentioned so far, step adaptation and multipulse adaptation, appear to be in a dynamical trade-off: the more step adaptation gets closer to perfect, the slower is the recovery in multipulse adaptation and viceversa. The limiting case of perfect step adaptation corresponds to no recovery at all in multipulse adaptation. In the present chapter this trade-off is investigated more in detail from both a theoretical and an experimental perspective. In particular, we observe that both our sensory systems obey to the rules imposed by this trade-off, and the fact can be neatly observed in the transient profiles of the electrophysiological recordings. We show that the trade-off is naturally present also in basic regulatory circuits, and that the time constant of the dynamical feedback can be used to decide the relative amount of the two forms of adaptation. These elementary circuits help us understanding the key ingredients needed to have both forms of adaptation, and confuting potential alternative models. For example, while it is in principle possible to realize some form of recovery in multipulse adaptation also in presence of exact integral feedback, we show that this requires necessarily a transient response that undershoots its baseline level during the deactivation phase, something that is not observed experimentally in neither sensor. However, if we manage to artificially shift the baseline level (for example performing phototransduction experiments in dim background light rather than in dark) then our simplified model predicts that nonnegligible undershoots in the deactivation phase should emerge. We have indeed verified their presence in experiments.

Stimulus-response behavior for various input protocols. Several input protocols, i.e., classes of time courses given to the stimulus are used for our two sensory systems:

1. steps;

2. repeated pulses at different lag times;

3. double (nested) steps.

We have applied the first two protocols to olfactory neurons and photoreceptors, obtaining electrical recordings like those shown in Fig. 3.1-3.2. The double step is instead used only for phototransduction (shown in Fig. 3.2 B).

The responses to these input protocols for the two systems exhibit several common features which are highlighted below:

1. step response: we observe a transient excursion followed by a decline of the output signal, which tends to return towards its basal, pre-stimulus level (more in olfactory transduction than in phototransduction);

2. multipulse response: if for short delays between the two pulses the response to the second pulse is attenuated with respect to the first one, as the lag time between the two pulses increases, a progressive growth of the amplitude of the second response is observed, up to a complete recovery;

3. double step response (in phototransduction): unlike for a single step, the deactivation phase of the inner step exhibits an overshoot with respect to the steady state value corresponding to the outer step. No significant overshoot is observable for deactivation of the outer step.

It is remarkable that both sensors exhibit input-output responses which are qualitatively similar for what concerns both the types of adaptation previously mentioned.

3.2 Experimental methods

Olfactory transduction Olfactory sensory neurons have been dissociated from the *Ambystoma Tigrinum* salamander as previously reported [25]. Only neurons with clearly visible cilia were selected for the experiments. The currents were elicited by the application of 0.1 mM IBMX, previously dissolved in DMSO at 100 mM and then diluted in a Ringer solution in order to obtain the final concentration value. The release of IBMX to the neurons was performed through a glass micropipette by pressure ejection (Picospritzer, Intracel, United Kingdom). All experiments were performed at room temperature (22-24°C). Transduction currents on the surface of the dissociated neurons were measured through whole-cell voltage clamp recordings (as described in [25, 48, 51]) where the holding potential corresponds to -50mV. All experiments were carried out in accordance with the Italian Guidelines for the Use of Laboratory Animals (Decreto Legislativo 27/01/1992, no. 116).

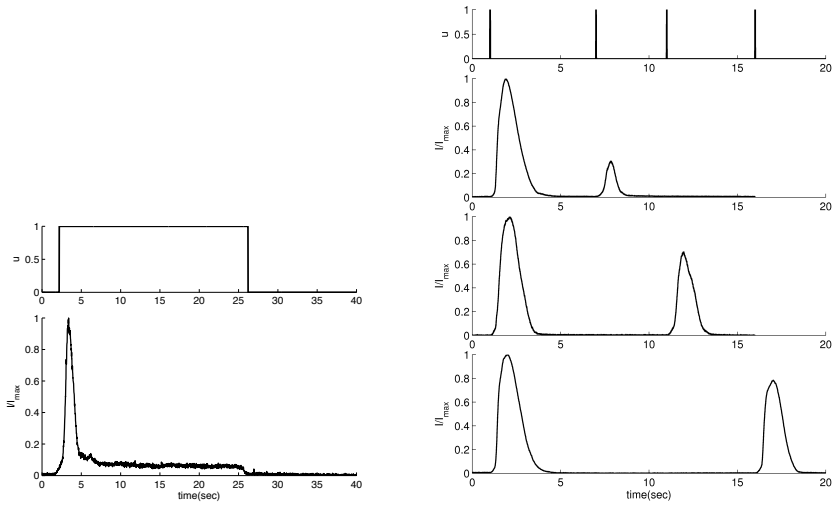

Figure 3.1: **Step and multipulse responses for the olfactory transduction pathway.** A: An example of a normalized response to a stimulus of IBMX sustained for 24 s, applied to a salamader olfactory sensory neuron. B: examples of normalized responses to two identical pulses of IBMX of duration 20 ms, applied with a time interval Δt of 6, 10, and 15 s respectively.

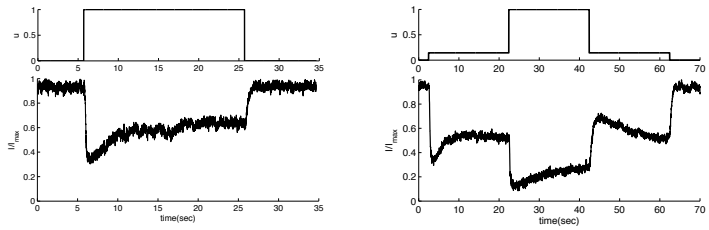

A B

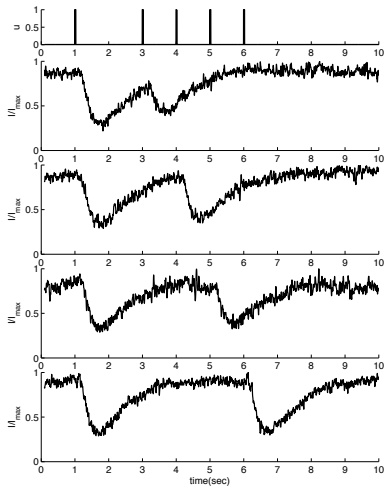

C

Figure 3.2: **Step and multipulse responses for the phototransduction pathway.** A: An example of normalized response to a step sustained for 20 s in non saturating light conditions (wavelength 491 nm) obtained with suction-electrode recording method from an isolated and intact *Xenopus laevis* rod in dark-adapted conditions. B: Example of normalized response to a double step of non saturating light; the two nested steps have a duration of 60 and 20 s. C: Example of normalized response from two identical non saturating light pulses with a duration of 5 ms applied with a time interval Δt of 2, 3, 4, and 5 s respectively.

Phototransduction Isolated photoreceptors from retina: dissociated rods were obtained using adult male *Xenopus laevis* frogs as previously reported [52, 59, 90]. All experiments carried out have been approved by the SISSA's Ethics Committee according to the Italian and European guidelines for animal care (d.l. 116/92; 86/609/C.E.). The frogs were dark-adapted and the eyes were enucleated and emisected under a dissecting microscope with infrared illumination (wavelength 820 nm); isolated and intact rods were obtained by repeatedly dipping small pieces of retina into a Sylgard Petri dish with a Ringer solution containing the following (in mM): 110 NaCl, 2.5. KCl, 1 CaCl2, 1.6 MgCl2, and 3 HEPES-NaOH, 0.01 EDTA and 10 Glucose (pH 7.7 - 7.8 buffered with NaOH). After dissociation the sample was transferred into a silanized recording chamber containing the Ringer solution. All experiments were performed at room temperature (22-24°C).

Electrophysiological recordings: after the mechanical isolation, the external (or the internal) segment of an isolated and intact rod was drawn into a silane-coated borosilicate glass electrode (internal diameter of 6-8 μm) filled with Ringer solution. The cell was viewed under infrared light (wavelength 900 nm) and stimulated with 491 nm diffuse light (Rapp OptoElectronic, Hamburg, Germany). The photocurrents obtained after the stimulus where recorded using the suction-electrode recordings, as previously described [27, 52], in voltage-clamp conditions and achieved with an Axopatch 200A (Molecular Devices). The functionality of the cell was confirmed by the observation of the amplitude of the cell response (typically 15-20 pA) to brief light flashes (1 ms) of saturation intensity. Different light stimuli protocols were used for different recordings (see figure legends).

3.3 Models

In the present section we introduce a minimal model able to reproduce the features of the response, obtained improving some 2-variable systems. More detailed models of the olfactory and phototransduction pathways which have been used to fit the experimental data are then described.

3.3.1 A minimal regulatory model for input response.

Detailed dynamical models for the two sensory systems can be found in [22, 33] for olfactory transduction and in e.g. [27, 34, 87] for phototransduction. The approach followed in this work is different: rather that including into our models all the kinetic details available for the two signaling pathways, we would like to introduce an elementary model which, in spite of its extreme simplicity, is nevertheless able to

qualitatively capture the salient features of the various responses. This basic model is presented now in general terms. In Section 3.4 an interpretation in terms of the specific signaling mechanisms of the two pathways is provided. More specific models tailored to the two transduction processes are discussed in Subsection 3.3.3

Consider the 2-variable prototype regulatory system depicted in Fig. 3.3 A. It represents a system in which two molecular species y and x are linked by a negative feedback loop.

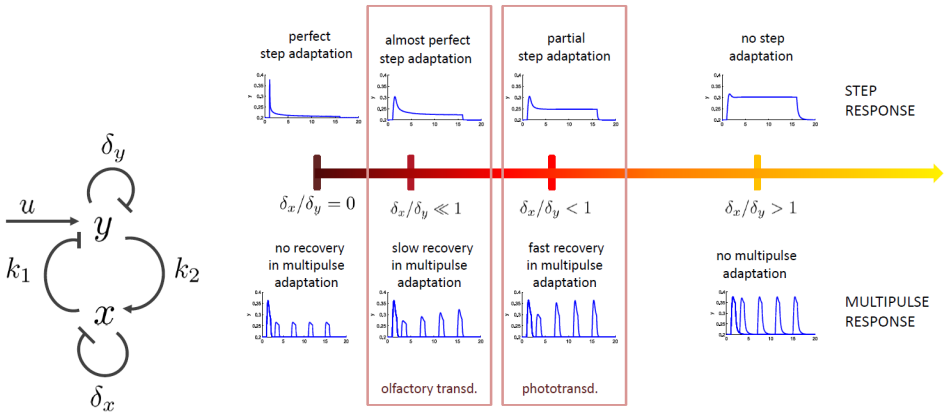

Figure 3.3: **Step and multipulse adaptation.** A: the basic model (3.3.1) consists of the two variables y and x linked by a negative feedback loop (of gains k_1 and k_2), an external input u, and two first order degradation terms (of rates δ_x and δ_y). B: Various levels of adaptation for the model (3.3.1), according to the ratio δ_x/δ_y. The upper and lower parts of the panel show the response to the two main input protocols described in the text, steps and multiple pulse pairs (here a series of 4 pulse pairs in which the second pulse is progressively delayed with respect the first; the 4 double pulse responses are shown all simultaneously, and the 4 first pulses of each pair are all identical and overlapping). Notice that the step responses resembles those of Fig. 5 of [44]. The ratio δ_x/δ_y determines the amount of the two forms of adaptation mentioned in the text, step adaptation and multipulse adaptation. In particular perfect step adaptation requires exact integral feedback (i.e., $\delta_x = 0$) and corresponds to no recovery in multipulse adaptation (leftmost plots). Moving from left to right of the panel as we increase the ratio δ_x/δ_y, step adaptation decreases and the recovery in multipulse adaptation becomes faster. See Fig. 3.6 for blown-up plots of the various cases.

The following minimal mathematical model describes the reactions in the scheme

of Fig. 3.3 A:

$$\begin{aligned} \dot{y} &= u(1-y) - k_1 xy - \delta_y y \\ \dot{x} &= k_2 y - \delta_x x, \end{aligned} \tag{3.3.1}$$

where k_1 and k_2 are gains and the two parameters δ_x, δ_y represent first order degradation rates in y and x. The external stimulus u favors the production of y, which is instead inhibited by the negative feedback from x. In turn, the synthesis of x is enhanced by y. By construction $0 \leqslant y \leqslant 1$ and $x \geqslant 0$, meaning that the model is biologically consistent. The model (3.3.1) is the simplest elementary dynamical system having an input-output behavior resembling that of olfactory transduction.

Consider the change of variable $z = 1 - y$, $0 \leqslant z \leqslant 1$. A straightforward algebraic manipulation allows to rewrite the system (3.3.1) in terms of z. In this case the regulatory actions have the opposite sign: u decreases z while the feedback from x promotes the formation of z.

$$\begin{aligned} \dot{z} &= -uz + k_1 x(1-z) + \delta_y(1-z) \\ \dot{x} &= k_2(1-z) - \delta_x x. \end{aligned} \tag{3.3.2}$$

This is the minimal model which will serve as reference for the input-output behavior of phototransduction. By construction, the models (3.3.1) and (3.3.2) exhibit the same dynamical behavior up to a flipping symmetry in the y and z variables. An exegesis of these models, explaining the role of each of the terms, and including other technical details such as shifted baseline levels, is presented in the following subsections.

3.3.2 Further considerations on elementary 2-variable models

From exact integral feedback model to integral feedback with memory decay This section is meant to explain why on elementary models a simple exact integral feedback is not suitable to reproduce the analyzed data. For the sake of simplicity, we take as reference the experiments with olfactory neurons shown in Fig. 3.1, in which the input positively stimulates the state variable y of the system (and hence the output). We review (basic) models starting from the one in [107] and adding elements to it, with the aim of "qualitatively" satisfying the following dynamical features:

- reproduce the step adaptation, with its steady state value which is similar but not exactly equal to the pre-stimulus level;

- reproduce the two-pulse adaptation protocol, with its recovery profile;
- avoid non-physiological signals. These correspond for example to negative concentrations of a substance, but also to unrealistic transient excursions. In particular in all our experimental data for olfactory response (see Chapter 2), the output current never undershoots the basal level of current, neither in a step adaptation nor in a multipulse protocol.

Model 1. The basic integral feedback model. Following the notation of the caption of Fig. 2 of [107], the basic model is

$$\begin{aligned} y &= k_1(u-x) - y_o \\ \frac{dx}{dt} &= y, \end{aligned} \tag{3.3.3}$$

where y is the output variable, y_o its basal level, and x the feedback variable.

A characteristic of this model is that when $y \geq 0 \; \forall\, t \geq 0$ (physiological condition for most biological models, including ours) $x(t) = \int_0^t y(\tau)d\tau$ is monotonically growing. Hence no matter how delayed is the second pulse of a two-pulse protocol, $y(t) \geqslant 0$ implies $x(t_2) \geqslant x(t_1) \; \forall\, t_2 > t_1$, meaning that the adapted response does not recover increasing the lag time between the two pulses. The only way to decrease x (to "discharge" the integrator in control engineering language) is to allow for negative y, see Fig. 3.4. Notice that the model is exactly the same as the following one, with baseline "shifted"

$$\begin{aligned} y &= k_1(u-x) \\ \frac{dx}{dt} &= (y-y_o), \end{aligned} \tag{3.3.4}$$

where integration is with respect to the baseline value y_o. Now the output y "moves around" y_o, hence when $y_o > 0$ it could remain positive even if $y - y_o < 0$. However, in the multipulse response the problem of possible negative values of y reappears if the amplitude of u is increased, meaning the model is not structurally consistent for biological signals. Furthermore, the profile for the deactivation phase (following the end of a pulse) is not physiological, and differs from any experimentally observed profile.

In addition, y has jumps when u has jumps, since the first equation of (3.3.3) is a static input-output relationship.

Model 2. Adding a kinetics to the input-output relationship. The static input-output transduction of model (3.3.3) can be replaced by a differential equation,

describing the kinetics from input u to output y

$$\begin{aligned} \frac{dy}{dt} &= f(u,\, x) \\ \frac{dx}{dt} &= y, \end{aligned} \tag{3.3.5}$$

where $f(\cdot)$ is any kinetic function, for example a linear one: $f(u,\, x) = u - k_1 x$. In this way we obtain a linear system $\xi = \begin{bmatrix} y \\ x \end{bmatrix}$

$$\frac{d\xi}{dt} = A\xi + Bu,$$

where $A = \begin{bmatrix} 0 & -k_1 \\ 1 & 0 \end{bmatrix}$, $B = \begin{bmatrix} 1 \\ 0 \end{bmatrix}$. A system like this is not asymptotically stable ($\mathrm{trace}(A) = 0$ means the eigenvalues are purely imaginary) and typically induces oscillations in response to steps, see Fig. 3.4. However if we add a damping, i.e., a negative term on the diagonal of A, then asymptotic stability is recovered.

Model 3. Adding a damping term to the y equation. A first possibility is to place the damping term (a first order decay) in the input-output transduction:

$$\begin{aligned} \frac{dy}{dt} &= u - k_1 x - \delta_y y \\ \frac{dx}{dt} &= y, \end{aligned} \tag{3.3.6}$$

or, in presence of a nonzero baseline y_o,

$$\begin{aligned} \frac{dy}{dt} &= u - k_1 x - \delta_y y \\ \frac{dx}{dt} &= y - y_o. \end{aligned} \tag{3.3.7}$$

From Fig. 3.4, these curves are qualitatively correct for double pulse adaptation and show perfect step adaptation. However, as in **Model 1** the double pulse adaptation is obtained only because y becomes negative (or undershoots its baseline), hence the model is inadequate for the same reasons.

Model 1

$$\begin{aligned} y &= k_1(u-x) \\ \frac{dx}{dt} &= y \end{aligned}$$

exact integral feedback
static input-output map
undershooting

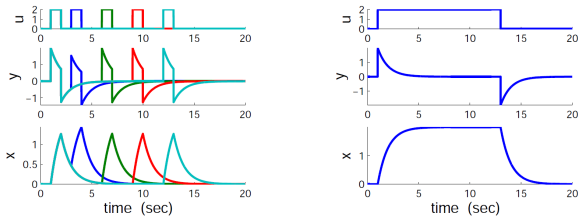

Model 2

$$\begin{aligned} \frac{dy}{dt} &= u - k_1 x \\ \frac{dx}{dt} &= y \end{aligned}$$

exact integral feedback
not asymptotically stable

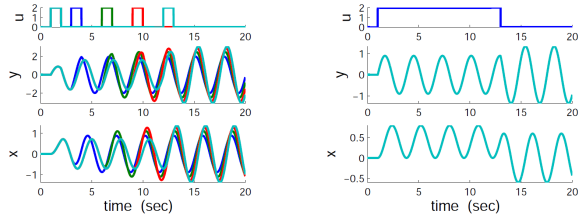

Model 3

$$\begin{aligned} \frac{dy}{dt} &= u - k_1 x - \delta_y y \\ \frac{dx}{dt} &= y \end{aligned}$$

exact integral feedback
asymptotically stable
undershooting

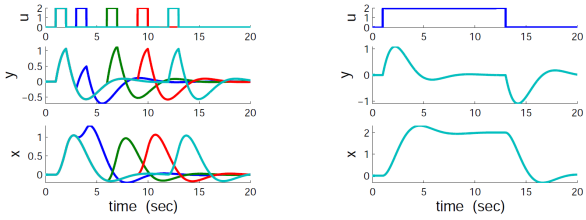

Figure 3.4: **Step and multipulse response for the Models 1-3**. The main dynamical properties of the models are summarized below the equation box.

In order to avoid negative values of y, the simplest solution is to introduce a nonlinearity in the ODE for y, for example a quadratic term, in our case representing the "encounters" of x and y in a mass-action formalism.

Model 4. Adding a quadratic term on **Model 3**. Adding the quadratic term in the input-output transduction and keeping the linear decay in y we get

$$\begin{aligned} \frac{dy}{dt} &= u - k_1 xy - \delta_y y \\ \frac{dx}{dt} &= y. \end{aligned} \tag{3.3.8}$$

From Fig. 3.5, the model (3.3.8)

- avoids negative values for y;
- does not reach a steady state in x in the step response ($dx/dt > 0$ always);
- shows no recovery of the adaptation to a double pulse.

The latter item in particular is unavoidable regardless of the functional form chosen for the kinetics of y, as long as the exact integral ODE of model (3.3.8) is used. In this case in fact the only way to "discharge" the integrator is when y assumes negative values.

We deduce therefore that adaptation to a double pulse cannot be achieved by an exact integral feedback in which the integrated variable is never negative. The argument is similar in presence of a baseline y_o (and of an output y s.t. $y - y_o \geq 0$ always, as in our experiments).

Model 5. Quadratic term as in **Model 4** and damped integral feedback.

In this model the diagonal damping term affects the feedback variable:

$$\begin{aligned} \frac{dy}{dt} &= u - k_1 xy \\ \frac{dx}{dt} &= y - \delta_x x. \end{aligned} \tag{3.3.9}$$

This is the starting point of our scheme of an integral feedback with a memory decay.

From Fig. 3.5, the model (3.3.9)

- avoids negative values of y (or of $y - y_o$ in case of nonzero baseline);
- shows a non perfect adaptation to a step;
- exhibits a recovery of the adaptation in a double pulse protocol.

Qualitatively this elementary model reproduces all the dynamical features observed in the experimental data. The presence of a damping term $-\delta_y y$ in the first equation of model (3.3.9) does not alter this qualitative behavior provided that δ_x/δ_y is small enough (the time constant of x is longer than the one of y).

Model 6. Adding a conservation law to **Model 5**.

If, as in our models, y represents a fraction of a certain molecular species of constant total concentration (e.g. the fraction of open CNG channels in olfactory transduction), then its value must be constrained, for example assuming $0 \leqslant y \leqslant 1$. The **Models 1÷5** do not respect this constraint, because u is not linked to the value assumed by y. A conservation law can be imposed multiplying u by the complement of y (i.e., by the fraction of closed CNG channels in the olfactory pathway). The resulting model

$$\begin{aligned} \frac{dy}{dt} &= u(1-y) - k_1 xy \\ \frac{dx}{dt} &= y - \delta_x x, \end{aligned} \tag{3.3.10}$$

is the one described in the previous subsections once a degradation term is added in the second equation. A similar conservation law can in principle be applied also to x (not necessary in our case). As can be seen on Fig. 3.5, the behavior of **Model 6** is qualitatively similar to that of **Model 5** for what concerns our input responses.

Whenever basal regulation is nonnegligible, nonzero baseline levels can be taken into account for both y (as we did above with y_o) and x (denote it x_o). The model (3.3.10) can be amended as follows:

$$\begin{aligned} \frac{dy}{dt} &= u(1-y) - k_1(x - x_b)(y - y_o) \\ \frac{dx}{dt} &= (y - y_o) - \delta_x(x - x_o) \end{aligned} \tag{3.3.11}$$

where the baseline may or may not be present in the first order degradation rates, depending on the context.

Model 4

$$\begin{array}{rcl} \frac{dy}{dt} & = & u - k_1 xy - \delta_y y \\ \frac{dx}{dt} & = & y \end{array}$$

exact (bilinear) integral feedback
never undershooting
no multipulse adaptation
no steady state for step adaptation

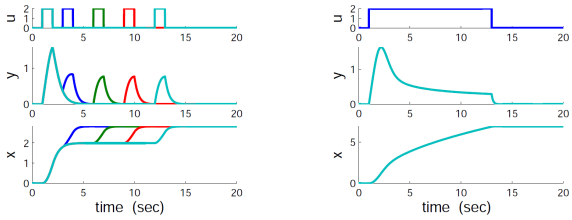

Model 5

$$\begin{array}{rcl} \frac{dy}{dt} & = & u - k_1 xy \\ \frac{dx}{dt} & = & y - \delta_x x \end{array}$$

integral feedback with memory decay
never undershooting
multipulse adaptation
(non-perfect) step adaptation

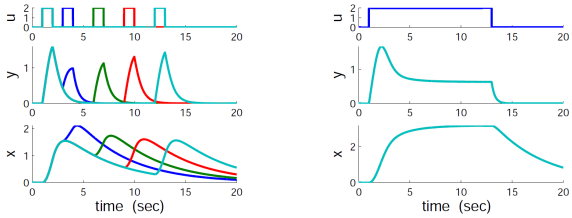

Model 6

$$\begin{array}{rcl} \frac{dy}{dt} & = & u(1-y) - k_1 xy \\ \frac{dx}{dt} & = & y - \delta_x x \end{array}$$

conservation law for y
integral feedback with memory decay
never undershooting
multipulse adaptation
(non-perfect) step adaptation

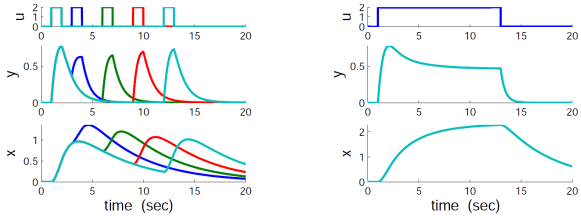

Figure 3.5: **Step and multipulse response for the Models 4-6**. The main dynamical properties of the models are summarized below the equation box.

"Discharging" an integral feedback by undershooting: confutation of an alternative model. Reviewing the behavior of the basic **Models 1** through **5** of the previous paragraph, it can be observed that even with an integral feedback it is possible to generate output profiles which match qualitatively the responses to both types of adaptation but do not exhibit the trade-off described here. This case corresponds for example to Model 3, see (3.3.6) and Fig. 3.4. In this model, the (exact) integrator is "discharged" through a signal that undershoots the baseline level, avoiding any memory decay. From (3.3.7) if y_o is the baseline of y, then $y < y_o$ implies that even with $\delta_x = 0$ the integral $x(t) = \int_0^t (y(\tau) - y_o)d\tau$ is no longer monotone, i.e., the integral $x(t)$ can indeed decrease also in a model with exact integral feedback.

The undershooting in the deactivation phase should however be observable experimentally, i.e., it should produce an output current which becomes less than basal in olfactory transduction or higher than basal in phototransduction. No experiment with the olfactory system shows undershooting of the basal current. Also in phototransduction experiments, for both pulse and step responses in dark, no overshooting above the noise level can be observed in the deactivation phase. For both sensors, a large number of similar experiments available in the literature confirms the lack of undershoot (overshooting for phototransduction) deactivation transients [11, 15, 26, 27, 73, 80].

Furthermore, if y represents a fraction of a (positive) quantity, $0 \leqslant y$, $y_o \leqslant 1$, the scheme making use of undershooting to discharge the integral, in order to be plausible, requires that y_o is sufficiently large. In olfactory transduction, however, y reflects the fraction of open CNG channels, and it is estimated that $y_o \sim 0$ in absence of stimulation (y reaches 0.9 upon strong stimulations). Hence, to preserve nonnegativity of concentrations, the admissible undershooting would in any case be extremely limited. The behavior in phototransduction is not completely specular, in the sense that, for the "complementary variable" $z = 1 - y$, z_o (representing the basal fraction of open channels) in dark is low, and during the transient it decreases further, $z \leqslant z_o$ (i.e., CNG channels close even more, up to a complete closure for saturating illuminations). In spite of this, it is worth observing that when stimulated in dark, overshooting transients in the deactivation phase of a pulse/step are not seen in experiments with rods.

The similarity of the behavior in the two sensors confirms that "discharging" of the feedback variable(s) has to be accomplished by some other mechanism such as the memory decay. Other pieces of evidence in favor of the memory decay mechanism include the graded steady state level reached in response to graded step inputs, see

Chapter 2 for a relate discussion in the olfactory transduction system. Remarkably for cones (which are known to never saturate [74]) some form of undershooting is instead observed [42].

3.3.3 Signaling pathways and their models

Olfactory transduction

Pathway. In the absence of stimuli, the cyclic nucleotide-gated (CNG) channels in the olfactory transduction are almost completely closed. The arrival of the odorant molecules increases, through a G-protein cascade, the amount of activated adenylyl cyclase, which in turn leads to the accumulation of cyclic AMP, thus triggering the opening of the CNG channels. This allows various types of cations to enter the cell. Among these, the calcium ions further open the calcium-activated chloride channels, leading to a second current of chloride anions which flows out from the cell, amplifying the original response [40, 70]. Calcium is also responsible for several feedback loops in the pathway: by binding to proteins (among these possibly calmodulin) which are natively attached to the CNG channels, it decreases the sensitivity of the channels to cAMP thus inducing their closure [6, 14, 19]. Furthermore, by binding to calmodulin free in the cytoplasm it causes the hydrolysis of cAMP through a phosphodiesterase (PDE) [13], and this calcium-calmodulin (CaCaM) complex can activate also the enzyme CaCaM-dependent protein kinase II (CaMK) which inhibits the adenylyl cyclase activity [103]. Calcium is finally extruded through the Na^+/Ca^{2+} exchanger [60]. More details on the pathway are available in the Introduction.

Dynamical model. For the sake of simplicity, these feedback actions are lumped together into the single feedback shown in Fig. 3.10 A. Extensive analysis of more complex models carried out in Chapter 2 in fact suggests that the multiple feedback actions are redundant for what concerns the adaptation behavior considered in this work. Our "minimal" model includes therefore 3 state variables: $[CNG_o]$ (fraction of open channels), [Ca] (concentration of Ca^{2+} ions) and [CaBP] (concentration of the complexes that calcium forms with the protein complexes natively bound to the CNG channels, here indicated as BP). The first and the latter of these variables obey a conservation law. The total number of CNG channels (normalized to one) is the sum of the closed and the open channels (respectively $[CNG_c]$ and $[CNG_o]$). Furthermore the equation $[BP]+[CaBP] = 1$ represents the conservation of the total concentration of the calcium-binding proteins BP. For this reaction a mass-action

kinetic is considered:

$$\mathrm{Ca}^{2+} + \mathrm{BP} \underset{\beta_{\mathrm{CaBP}}}{\overset{\alpha_{\mathrm{CaBP}}}{\rightleftharpoons}} \mathrm{CaBP}.$$

In our dynamical model the cyclic AMP can be considered as the input of the system (here called u):

$$\frac{\mathrm{d}[\mathrm{CNG_o}]}{\mathrm{dt}} = (1-[\mathrm{CNG_o}])u - k_1[\mathrm{CNG_o}][\mathrm{CaBP}]^2 \tag{3.3.12}$$

$$\begin{aligned}\frac{d[\mathrm{Ca}]}{dt} &= k_2[\mathrm{CNG_o}] - \delta_{\mathrm{Ca}}[\mathrm{Ca}] \\ &\quad -\alpha_{\mathrm{CaBP}}[\mathrm{Ca}](1-[\mathrm{CaBP}]) + \beta_{\mathrm{CaBP}}[\mathrm{CaBP}]\end{aligned} \tag{3.3.13}$$

$$\frac{d[\mathrm{CaBP}]}{dt} = \alpha_{\mathrm{CaBP}}[\mathrm{Ca}](1-[\mathrm{CaBP}]) - \beta_{\mathrm{CaBP}}[\mathrm{CaBP}]. \tag{3.3.14}$$

In (3.3.12) the first term represents the opening of the CNG channels due to cyclic AMP and the second term the negative feedback (which includes a cooperative action, known to hold for calmodulin [14]). Equations 3.3.13 and 3.3.14 include the mass-action terms introduced above and the inflow of calcium due to the opening of the channels (term $k_2[\mathrm{CNG_o}]$). The linear degradation term $\delta_{\mathrm{Ca}}[\mathrm{Ca}]$ includes also the extrusion of calcium through the sodium-calcium exchanger. More details on the kinetic terms are available on Chapter 2.

In the cilia the CNG current is further amplified by the chloride current flowing through the calcium-activated chloride channels. Therefore the output of our model (total elicited current) is calculated as the sum of the current flowing through the CNG channels (proportional to the fraction of open channels), and of that carried by chloride anions. To account for this second component we use a Hill-dependence on the calcium concentration with a cooperativity index n equal to 2 (as in [11, 40, 94]) and with the half-activation constant $K_{1/2}$ equal to 4 μM [11, 40]. Furthermore we have added a weight of 0.2 for the current carried by CNG channels and of 0.8 for the calcium-activated chloride current, to reflect their proportionality in the biological data [12]

$$I_{\mathrm{olf}} = 0.2\,[\mathrm{CNG_o}] + 0.8\Big(\frac{[\mathrm{Ca}]^n}{[\mathrm{Ca}]^n + K_{1/2}^n}\Big). \tag{3.3.15}$$

Phototransduction

The signaling mechanisms involved in the phototransduction of vertebrate rods are described at length in several survey papers, such as [15, 23, 73, 74]. Also several detailed mathematical models exist, see e.g. [27, 34, 73, 87]. Coherently with the approach followed in this work, only the basic ingredients needed to have a minimal

regulatory system are considered in our model.

Pathway. In darkness, rods are characterized by Ca^{2+} and Na^{+} currents which circulate through cGMP-gated CNG channels (inflow) and exchange pumps (outflow). Light photoisomerizes rhodopsin which, through the mediation of G-proteins, activates PDE. Activated PDEs hydrolyze cGMP, and the drop of cGMP induces the closure of the CNG channels and hence a drop in the Ca^{2+} current. As the efflux through the exchange pumps is not affected, also the cytoplasmic concentration of Ca^{2+} drops. In dark, Ca^{2+} binds to the guanylate cyclase activating protein (GCAP) reducing its function of inhibitor of guanylate cyclase (GC) activity. The drop of Ca^{2+} during light response implies calcium-free GCAP binds to GC and increases its catalytic activity for second messengers. Hence the synthesis of cGMP passes from a basal level to a higher rate, thereby completing the negative feedback loop which forms the core of the regulation considered in our model. Calcium is responsible for at least two more feedback mechanisms present in the phototransduction pathway[1]. It decreases the affinity of CNG channels through the binding with calmodulin, and the calcium-binding protein recoverin inhibits the phosphorilation of rhodopsin due to G-protein-coupled-receptor-kinase 1 (GRK1) preventing the complete deactivation of rhodopsin by arrestin. Therefore, a decreasing concentration of calcium promotes the activity of GC, the opening of the CNG channels and the quench of rhodopsin [46, 73, 106]. The feedback involving the modulation of the GC is considered dominant at low and intermediate light intensities, whereas the feedback due to recoverin-arrestin seems to play a more important role at higher intensities [106]. The feedback action of calcium ions on CNG-channels is of little importance in rods phototransduction compared with the other two mechanisms [45]. See the Introduction for a more detailed description of the pathway.

Dynamical model. In what follows we will disregard the feedbacks mediated by calmodulin and by recoverin and concentrate on the GC feedback loop. The resulting basic pathway considered in our model is depicted in Fig. 3.11 A. For this pathway we consider a model of 4 variables: [cGMP] (concentration of cGMP), [CNG_o] (fraction of open CNG channels), [Ca] (concentration of Ca^{2+} ions), [GC] (fraction of active guanylate cyclase). GCAP is not modeled explicitly. Conservation laws are imposed on [CNG_o] and [GC]. Denoting [CNG_c] and [GC_i] respectively the fraction of closed CNG channels and the fraction of inactive GC enzyme, these conservation laws can be expressed as $[CNG_o] + [CNG_c] = 1$ and $[GC] + [GC_i] = 1$. The reactions for

[1]Several extra feedback loops are actually mentioned in [73] but will not be described here.

which we use mass-action kinetics are the following:

$$\begin{aligned}
\mathrm{CNG}_c + 2\mathrm{cGMP} &\underset{\beta_{\mathrm{CNG}}}{\overset{\alpha_{\mathrm{CNG}}}{\rightleftharpoons}} \mathrm{CNG}_o \\
\mathrm{GC} + 2\mathrm{Ca}^{2+} &\underset{\beta_{\mathrm{GC}}}{\overset{\alpha_{\mathrm{Ca}}}{\rightleftharpoons}} \mathrm{GC}_i \\
\mathrm{cGMP} &\xrightarrow{\delta_{\mathrm{CNG}}} \emptyset \quad \text{(hydrolyzed to GMP)} \\
\mathrm{Ca}^{2+} &\xrightarrow{\delta_{\mathrm{Ca}}} \emptyset \quad \text{(outflow from the outer segment).}
\end{aligned}$$

The second reaction models the (GCAP mediated) inhibition of GC by Ca^{2+}, which occurs in darkness. Additional (non-mass action) reactions express the inflow of Ca^{2+} through the open CNG channels (linear term, with gain constant k_2), and the feedback action (linear production of cGMP, whose substrate, GTP, is considered abundant). The ODEs we will use are the following:

$$\begin{aligned}
\frac{d[\mathrm{cGMP}]}{dt} &= -(u + \delta_{\mathrm{cGMP}})[\mathrm{cGMP}] + k_1[\mathrm{GC}] \\
&\quad -2\alpha_{\mathrm{CNG}}[\mathrm{cGMP}]^2(1 - [\mathrm{CNG_o}]) + 2\beta_{\mathrm{CNG}}[\mathrm{CNG_o}] \qquad (3.3.16) \\
\frac{d[\mathrm{CNG_o}]}{dt} &= \alpha_{\mathrm{CNG}}[\mathrm{cGMP}]^2(1 - [\mathrm{CNG_o}]) - \beta_{\mathrm{CNG}}[\mathrm{CNG_o}] \qquad (3.3.17) \\
\frac{d[\mathrm{Ca}]}{dt} &= k_2[\mathrm{CNG_o}] - \delta_{\mathrm{Ca}}[\mathrm{Ca}] \\
&\quad -2\alpha_{\mathrm{GC}}[\mathrm{GC}][\mathrm{Ca}]^2 + 2\beta_{\mathrm{GC}}(1 - [\mathrm{GC}]) \qquad (3.3.18) \\
\frac{d[\mathrm{GC}]}{dt} &= -\alpha_{\mathrm{GC}}[\mathrm{GC}][\mathrm{Ca}]^2 + \beta_{\mathrm{GC}}(1 - [\mathrm{GC}]) \qquad (3.3.19)
\end{aligned}$$

In the phototransduction experiments the only affected current in response to light stimuli is the one flowing through the CNG channels. Therefore the output of the model (reproducing the measured current) is considered proportional to the fraction of open CNG channels. To account for the normalization and the shift of the recorded currents (otherwise impossible to compare because of the different amplitudes and responses) we inserted in the model two parameters: K_I representing the amplification of the current and I_0 to account for a different dark current level:

$$I_{\mathrm{photo}} = I_0 + K_I[\mathrm{CNG_o}]. \qquad (3.3.20)$$

3.4 Results

In the present section we first show how the simple models (3.3.1) and (3.3.2) exclude the possibility that multipulse adaptation could be reproduced through perfect adaptation. Afterwards we explain in detail the concept of trade-off between time constants, showing how it can be noticed in the experimental recordings of the olfactory and phototransduction responses. The absence of undershooting in the deactivation phase and, on the contrary, the detection of it when the baseline is altered, like in the deactivation of a double pulse protocol, are then presented, both in the simulations of model (3.3.1) and in the experimental traces of the phototransduction pathway. We further introduce a parallelism between the simple models (3.3.1) and (3.3.2) and the experimental pathways. The details of the fitting procedure performed with models of Eqs (3.3.12)-(3.3.14) and of Eqs (3.3.16)-(3.3.19) are finally described.

Perfect adaptation fails to reproduce multipulse adaptation. While several models exist able to capture perfect step adaptation [2, 7, 37, 41, 100, 107], there is one general principle to which most proposals are equivalent, namely that perfect step adaptation in order to be robust to parametric variations must be obtained by means of a negative regulation, and that this regulation achieving perfect step adaptation must be of integral feedback type, see [37, 107]. In our minimal models (3.3.1) and (3.3.2), an integral feedback is obtained when the degradation rate constant for x vanishes i.e., $\delta_x = 0$. This corresponds to the second differential equation of (3.3.1) being formally solvable as the time-varying integral

$$x(t) = k_2 \int_0^t y(\tau) d\tau, \tag{3.4.21}$$

and analogously for (3.3.2). Since $y(t) \geqslant 0$, the integral (3.4.21) is monotonically growing in this case, hence the feedback variable keeps growing and stabilizes only when $y(t) \to 0$. Such a behavior occurs regardless of the amplitude of the input step[2] u. In the engineering analogy of an integrator being a capacitor, $y(t) \geqslant 0$ implies that $x(t)$ gets charged and never discharges. In a double pulse protocol, this implies that after the first pulse $x(t) > 0$, and when the second pulse arrives the response of the feedback is more prompt because $x(t)$ is already charged. Hence the second pulse response is attenuated with respect to the first. However, lack of degradation of $x(t)$

[2]When a nonzero baseline level y_o is considered in (3.3.1), then (3.4.21) becomes $x(t) = k_2 \int_0^t (y(\tau) - y_o) d\tau$. The monotonicity property is preserved for the variation with respect to y_o, and the steady state imposed by perfect adaptation is $y(t) \to y_o$.

implies that the behavior occurs regardless of the lag time between the two pulses, which contradicts the experimental results shown in Fig. 3.1 B and Fig. 3.2 C. Hence a perfect adaptation model is inadequate for our sensory transduction pathways, because i) it fails to reproduce the non-exact return to the prestimulus level observed in the step responses of Fig. 3.1 A and Fig. 3.2 A, and ii) it completely misses the recovery in the multipulse adaptation observed in Fig. 3.1 B and Fig. 3.2 C.

Reproducing both types of adaptation: a trade-off of time constants. In a model like (3.3.1) or (3.3.2), both types of adaptation are determined by the ratio between the characteristic time constants of the two kinetics, which are captured with good approximation by the first order kinetic terms (i.e., by δ_y and δ_x). The ratio δ_x/δ_y modulates the amount of adaptation in opposite ways in the two types of input protocols (see Fig. 3.6).

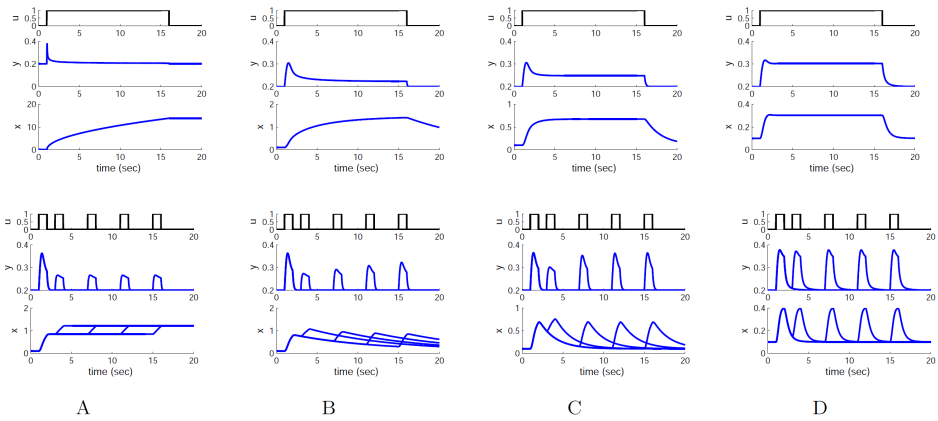

Figure 3.6: **Input responses of the 2-variable model** (3.3.1)**.** The various plots of Fig. 3.3 B are shown here more in detail. The 4 panels show the time course of the input (u) and state variables (y and x) of model (3.3.1) in response to steps (top) and multiple pulse pairs (bottom) for 4 different values of the ratio δ_y/δ_x. The same classification as in Fig. 3.3 B is followed. A: perfect step adaptation / no recovery in multipulse adaptation; B: almost perfect step adaptation / slow recovery in multipulse adaptation; C: partial step adaptation / fast recovery in multipulse adaptation; C: no step adaptation / no multipulse adaptation.

If $\delta_x = 0$ represents perfect step adaptation but recovery from multipulse adaptation is absent, when $\delta_x/\delta_y \ll 1$ (i.e., the characteristic time constant of x is much longer than that of y), then step adaptation is almost exact, while multipulse

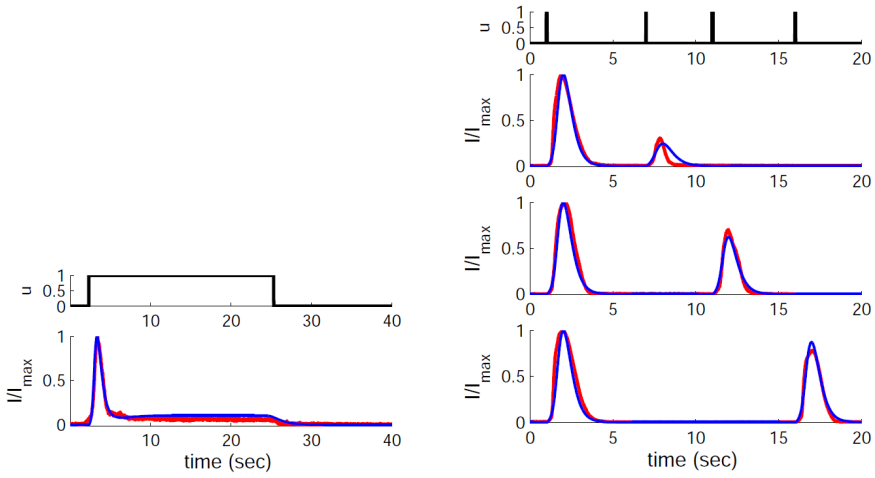

Figure 3.7: **Olfactory transduction.** In red, the experimental traces shown if Fig. 3.1. In blue the corresponding fits with the dynamical model of Eqs (3.3.12)-(3.3.14).

adaptation recovers very slowly. This behavior is similar to what happens in our experiments with the olfactory transduction system shown in Fig. 3.7. When instead $\delta_x/\delta_y < 1$ but not too far from a ratio of 1, then step adaptation is partial but multipulse adaptation recovers quickly, see again Fig. 3.3. This situation resembles our experiments with phototransduction shown in Fig. 3.8. When instead $\delta_x/\delta_y > 1$ neither of the two forms of adaptation is visible.

Deactivation and (lack of) undershooting. Upon termination of a step, a response deactivates, meaning in our model (3.3.1) that the observable variable y returns to its pre-stimulus level y_o (which for simplicity and without loss of generality we are assuming equal to 0). The way it does so is informative of the dynamics of the system. In a system with exact integral feedback, if the activation profile overshoots the baseline and then approaches it again, then the deactivation time course must follow a pattern which is qualitatively similar but flipped with respect to the baseline, i.e., it must undershoot the baseline during the transient, see Model 3 of the previous Section, described in (3.3.6) and Fig. 3.4. In models with a high degree of symmetry, like for example in presence of input scale invariance ("fold change detection" of [89]), the responses could even have a mirror symmetry around

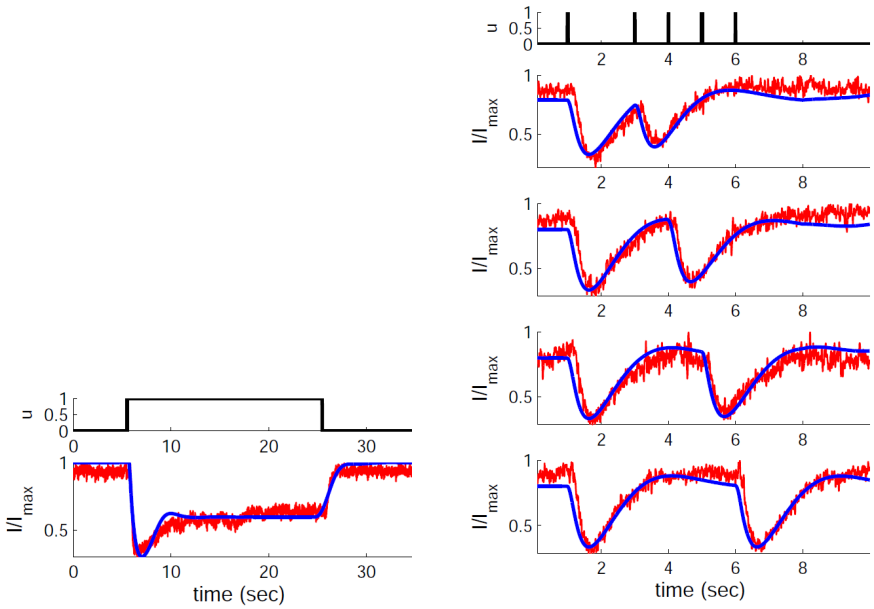

Figure 3.8: **Phototransduction.** In red, the experimental traces shown if Fig. 3.2 A, B. The blue traces show the response of the dynamical model of Eqs (3.3.16)-(3.3.19).

the baseline y_o.

The undershooting in the deactivation phase should however be observable experimentally, i.e., it should produce an output current which becomes less than basal in olfactory transduction or higher than basal in phototransduction. No experiment with the olfactory system shows undershooting of the basal current. Also in phototransduction experiments, for both pulse and step responses in dark, no overshooting above the noise level can be observed in the deactivation phase. For both sensors, this behavior is confirmed by many more experiments available in the literature [11, 15, 26, 27, 73, 80].

As already discussed, the lack of deactivation undershooting is another element that can be used to rule out the presence of exact integral feedback regulation in our systems.

A double step may instead exhibit undershooting. By construction, the model (3.3.1) can never undershoot the baseline since all negative terms in the first equation vanish when $y \to 0$ (the argument is similar for a baseline $y_o \neq 0$, see (3.3.11)). This is coherent with the step deactivation recordings shown in Figs. 3.7-3.8. Assume now that the input protocol consists of a double step as in Fig. 3.9. If y_1 is the steady state reached in correspondence of a single step, then necessarily $y_1 > 0$ in our non-perfectly adapting systems. However, even when this single step stimulation is present, the negative feedback in the model (3.3.1) still maintains the original baseline $y_o = 0$ as reference. It means that when a second step input is superimposed to the first as in Fig. 3.9, it is in principle possible that in the deactivation phase of this second step a transient significantly undershooting the "fictitious" baseline y_1 may now appear. This is indeed what happens for the model (3.3.1), see Fig. 3.9 A. Clearly under perfect adaptation $y_1 = y_o = 0$, hence exact integral feedback predicts no difference between the single step and the double step deactivation.

Given the very strong adaptation in olfactory sensory neurons, the double step experiment has been performed only in photoreceptors: indeed the combination of near zero baseline and almost perfect adaptation implies that in olfactory sensory neurons the presence of an overshoot will be hardly detectable. In photoreceptors, instead, the double step deactivation behavior of (3.3.1) is faithfully reproduced. In the input protocol, the broader step of smaller amplitude corresponds to a constant dim light on top of which a more intense light step is applied. The current recording shown in Fig. 3.9 B indeed exhibits a consistent deactivation overshooting not observed in dark.

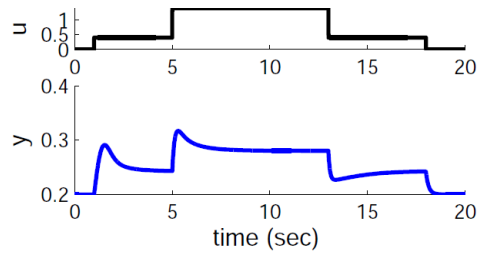

A

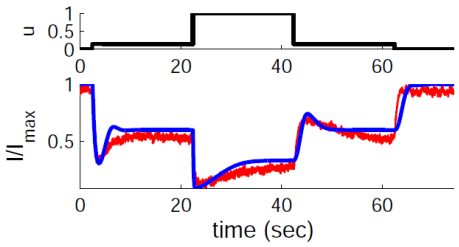

B

Figure 3.9: **Double step responses.** A: double step protocol applied to the model (3.3.1). While the step response never exhibits deactivation undershooting (i.e., upon termination of the step the output returns to its baseline without crossing it over), in a stimulation with a double step, the deactivation of the inner step shows a drop in the output that undershoots the shifted baseline. B: In red, the experimental traces shown if Fig. 3.2 C. The deactivation transients of the inner step overshoots the steady state corresponding to the outer step. The fitting for the model of Eqs (3.3.16)-(3.3.19) is shown in blue.

Apart from providing a validation of the reliability of the simple model (3.3.1), a direct interpretation of this transient is that indeed the system keeps a memory of the basal level "anchored" at y_o even when constant stimuli are applied to the system.

Interpretation of the elementary model in the context of olfactory and phototransduction pathways. In this work we will not attempt to present comprehensive mathematical models of the two sensory pathways containing all the biochemical reactions known to be involved in the signaling transduction of the stimuli, but will limit ourselves to consider the section of the pathways involving the Cyclic Nucleotide-Gated (CNG) channels and a primary calcium-induced feedback regulation. For the olfactory system, the pathway is depicted in Fig. 3.10 A and the corresponding model in Eqs (3.3.12)-(3.3.14).

In our minimalistic approach, in the olfactory system the variable y can be associated to the fraction of open CNG channels on the ciliary membrane. In absence of stimulation, the channels are almost completely closed. Upon arrival of a stimulation, the CNG channels open and the inflow of calcium ions triggers the negative feedback regulation which closes the CNG channels. In a model like (3.3.1), the feedback variable x plays the role of the concentration of the calcium-activated protein complexes responsible for the gating of the channels. The fit resulting from the kinetic model of Eqs (3.3.12)-(3.3.14) is shown in blue in Fig. 3.7, see also Fig. 3.10. Its dynamical behavior is very similar to that of (3.3.1), shown in Fig. 3.3 B.

Unlike for the olfactory system, in phototransduction the CNG channels are (partially) open in absence of stimulation, and they further close when the photoreceptors are hit by an input of light. If we think of z as the fraction of open CNG channels, then the mechanism (3.3.2) can be used in phototransduction to describe qualitatively the core action of the primary feedback loop (due to guanylate cyclase). In the response to light, in fact, its effect is to reactivate z. The resulting fit for the phototransduction experiments is the blue trace of Fig. 3.8. Other details are in Fig. 3.11. Also in this case the core dynamical behavior of the pathway-specific model of Eqs (3.3.16)-(3.3.19) and that of the elementary model (3.3.2) resemble considerably.

Fitting procedure. The parameters of the models of Eqs (3.3.12)-(3.3.14) and of Eqs (3.3.16)-(3.3.19) have been fitted to the data presented in Figs. 3.1 and 3.2. To perform this fit, we used the MATLAB function lsqcurvefit. This function minimizes the residuals sum of squares of the different datasets simultaneously with a nonlinear

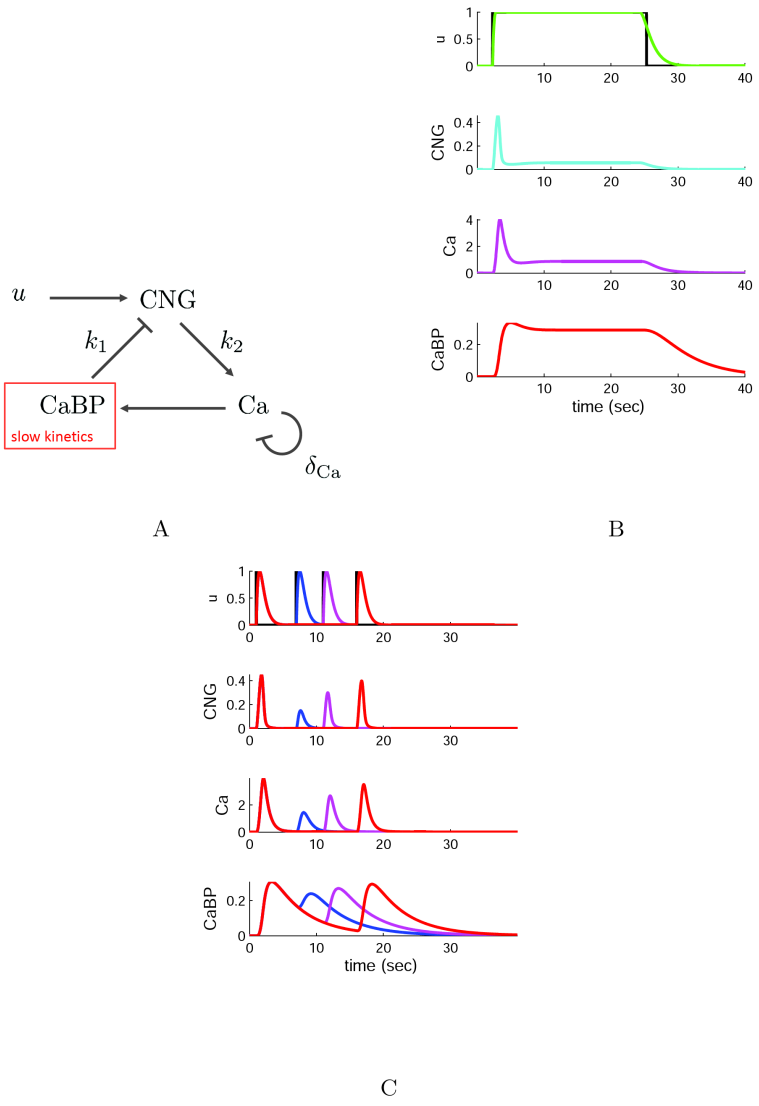

Figure 3.10: **Olfactory transduction.** A: the diagram represents the core regulatory action included in the model of Eqs (3.3.12)-(3.3.14) for the olfactory transduction. B: behavior of the state variables of Eqs (3.3.12)-(3.3.14) for the step response of Fig. 3.7 A. The top panel shows in black the "ideal" input and in green the more plausible input shape as described in (3.4.22). C: state variables (and input) for the pulse pairs of Fig. 3.7 B.

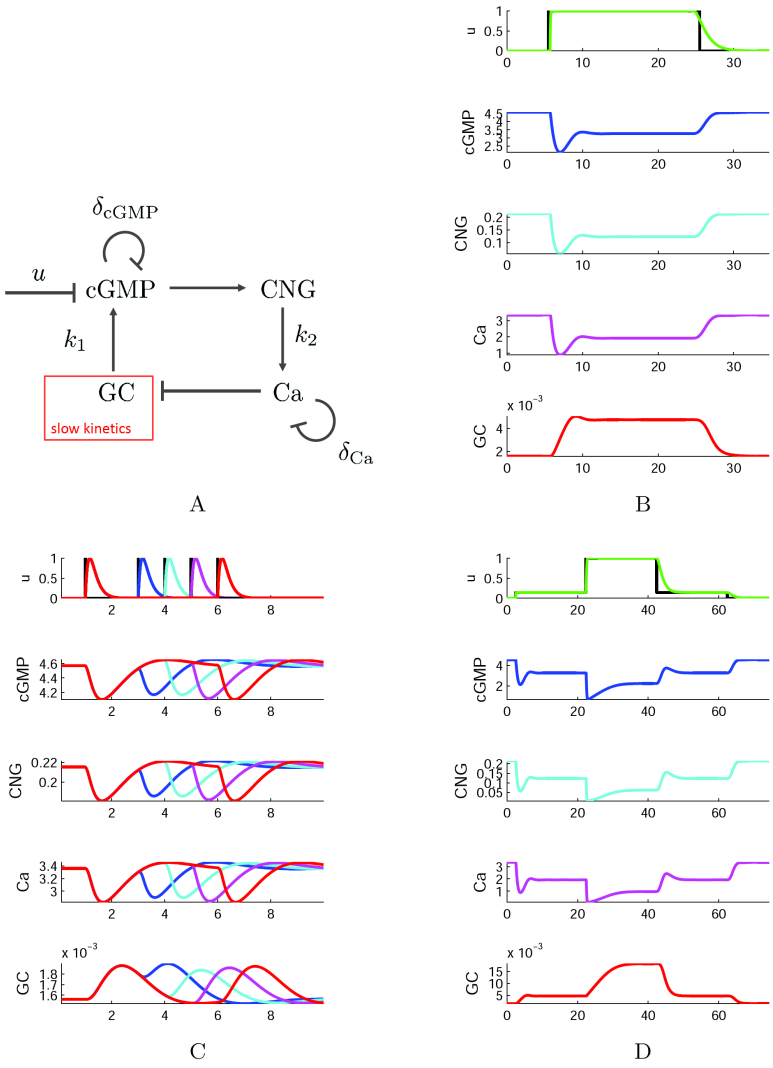

Figure 3.11: **Phototransduction.** A: the diagram shows the pathway used for phototransduction with its calcium-mediated GC feedback loop, see text and Eqs (3.3.16)-(3.3.19). The panels B, C and D show the input u (both the ideal profile in black and the more realistic shape obtained from (3.4.22) in color) and the 4 state variables of the model of Eqs (3.3.16)-(3.3.19) for B: the step response of Fig. 3.8 A; C: the multipulse response of Fig. 3.8 B; and D: the double step response of Fig. 3.9 B.

least square method (using the trust-region-reflective algorithm). The resulting values of the parameters are reported in Tables 3.1 and 3.2.

Table 3.1: **Parameter set used to fit the olfactory transduction data of Fig. 3.7.**

Name	Description	Value
k_1	CaBP feedback gain	215
k_2	inflow of Ca^{2+} through CNG channels	23
δ_{Ca}	outflow of Ca^{2+}	1.5
α_{CaBP}	association rate between Ca^{2+} and BP	0.10
β_{CaBP}	dissociation rate between Ca^{2+} and BP	0.21

Table 3.2: **Parameter set used to fit the phototransduction data of Figs. 3.8-3.9.**

Name	Description	Value
δ_{cGMP}	degradation rate of cGMP	0.38
k_1	GC feedback gain	3480
α_{CNG}	association rate between CNG and cGMP	1.95
β_{CNG}	dissociation rate between CNG and cGMP	150
k_2	inflow of Ca^{2+} through CNG channels	440
δ_{Ca}	outflow of Ca^{2+}	28
α_{GC}	association rate between Ca^{2+} and GC	0.10
β_{GC}	dissociation rate between Ca^{2+} and GC	0.0018

Modeling the input stimulus For phototransduction, the input of our model is the PDE which hydrolyzes the cGMP. Since we do not describe the early steps of the pathway, the dynamics of activation is taken from literature. For instance, the tailed peak of PDE from a pulse stimuli reported in [77] is here reproduced (normalized) with the following expression

$$u(t) = \begin{cases} 0 & t < t_o \\ (t - t_o)\lambda e^{1-\lambda(t-t_o)} & t \geqslant t_o \end{cases} \tag{3.4.22}$$

where the parameter $\lambda = 6.0$. Step inputs are reproduced holding the maximum value of this function for the whole length of the pulse. Moreover, we assume that the stronger action induced by a step (with respect to a short pulse) reflects also in a slower decay. In these cases the parameter λ is reduced to 2.2. The same input

modeling is used for the olfactory transduction, with values of $\lambda = 2$ and $\lambda = 1$ respectively.

Inducing adaptation via negative feedback: faster and slower time constants. As mentioned before, if in a model like (3.3.1) exact integral feedback implies an infinite time constant for the variable x, achieving partial step adaptation still requires a system with a faster (y) and a slower (x) kinetics, see Fig. 3.6. Also the models of Eqs (3.3.12)-(3.3.14) and of Eqs (3.3.16)-(3.3.19) obey this principle.

For example, it is known that in phototransduction the opening and closing of the CNG channels occurs on a very fast time scale (milliseconds, [73]) when compared with the PDE-mediated decline of the input stimulus and with the regulatory action of GC, which is induced by GCAP reactivation following the Ca^{2+} drop. Therefore for the purposes of our modeling we can consider the CNG gating (and the consequent kinetics of Ca^{2+} influx/efflux) as faster processes when compared to the negative feedback regulation due to GC, see Fig. 3.11 A.

Similarly in the olfactory transduction, the time constant of the feedback mechanism is longer than that associated with the opening of the CNG channels. As just mentioned, this last is known to be very fast, of the order of milliseconds, while the onset of the feedback is neatly slower, as can be seen in Fig. 3.1. Notice that also in Chapter 2, where related models are studied in detail, similar ranges of values for the time scales of the system emerge naturally when trying to fit step/multipulse response data.

Finally, it is worth remarking that the presence of fast and slow dynamics is a prerequisite also in other models for adaptation, like the incoherent feedforward loop (in this case a delay element is often used to mimic slower response).

On minimality of the model and identifiability At the level of a single photoreceptor, much more detailed kinetic models than the one adopted here to fit the data have been available for several years [27, 34, 73, 87]. The same consideration applies also to the olfactory transduction [22]. As we have observed for the latter pathway in Chapter 2, from the perspective of the input-output dynamical modeling (i.e., without the possibility of monitoring extra variables other than the stimulus and the output current) the introduction of extra details and of multiple feedback loops essentially introduces redundancy into the mathematical model. The complications associated with "non-minimal" dynamical models are well-known in the parameter identification literature [56, 82]. They essentially amount to the impossibility of uniquely determining the kinetic parameters of a model. The drastic choice

made in this work, namely to (deliberately) oversimplify the differential equations is also meant to avoid such type of ill-posed identifiability problems.

3.5 Discussion

To date, the vast majority of papers dealing with models for sensory adaptation has focused on the perfect step adaptation case [2, 7, 28, 36, 37, 41, 44, 57, 89, 91, 100]. While in some examples of sensory response, like in *E.coli* chemotaxis, perfect step adaptation may reasonably well describe the motility response of the bacterium, in many other case studies (notably in sensory systems of higher organisms) the classification as perfect adapters holds only as long as the sensor "as a whole" is considered. These sensory responses are however much more complex cognitive processes than the single cell signaling transductions considered in this work, and have little to do with the models (and data) discussed in this thesis. For example, the visual system can adapt over light variations of several orders of magnitude. However, when looking at single photoreceptors, if cones virtually never saturate in response to steady illumination [42, 74], the capacity of rods (the receptors studied in this work) to adapt is much more modest and this can already be seen in the partial step adaptation of Fig. 3.8 A. When it comes to modeling adaptation, an emblematic example of the difference between an omnicomprehensive sensory system and the single cell level of interest here is given by a "sniffer", i.e., a basic circuit (an incoherent feedforward loop) often considered as a model for perfect adaptation and sometimes taken as paradigm for the functioning of the sense of smell "as a whole" on a purely phenomenological basis [57, 89, 100]. This model not only can adapt perfectly, but it can do so without any feedback loop. If experiments such as those of Fig. 3.7 show that at the level of single receptor step adaptation is not exact, other experiments in low-calcium show that when the (calcium-induced) feedback regulation is impaired, adaptation basically disappears and even a single pulse response terminates very slowly (see e.g. [11] and Fig. 2.7 of Chapter 2). This implies that feedback regulation is crucial for adaptation in our olfactory neurons. As similar arguments hold also for phototransduction, in this work incoherent feedforward mechanisms are never considered as potential models for adaptation (perfect or less).

Even though the distinction between perfect and partial step adaptation has been known for a while [44], the dynamical implications of the different models for other input protocols has in our knowledge never been investigated in detail. In this work we show that not only this difference is observable in several experimental features of the responses, but also that it has important conceptual consequences. One of

these consequences is that in a system with a perfectly adapting mechanism modeled with an exact integral feedback the basal working value of the state is "internal" and uncorrelated with the environment. While this allows the system to climb exactly any step of input (all steps have the same steady state y_o), it implies that the transient responses during stimulus activation and termination should have similar (but specular with respect to a baseline level) profiles as in Model 3 of Fig. 3.4. On the contrary, in a sensor with a partial step adaptation mechanism, the steady states reached in the step responses depend on the amplitude of the step, while instead the feedback remains "anchored" around the basal level y_o, itself uniquely associated to an input amplitude (which could be $u = 0$ in the simplest case). This implies that while weberian-type graded responses for the peaks of the transients are still possible [74], properties involving the whole profile of the response such as the input scale invariance of [89] are no longer possible, not even approximately. Our double step experiment with its asymmetry in the two deactivation phases clearly shows that such an input invariance cannot hold not even qualitatively for our sensors. Furthermore, anchoring the state around a nominal value helps shifting the dynamical range back to that value when the stimulus terminates, resetting the sensor to the most plausible value of the environment without incurring into unrealistic deactivation transients.

Another important difference between the dynamical models of perfect and partial adaptation concerns the effect on internal, nonobservable variables like our x in (3.3.1). Exact integral implies an infinite time constant for x (or, in practice, longer that the time scales of interest for the observable kinetics). Partial step adaptation, instead, is associated to changes in x which are still slower than those observed on the output of the system, but not by orders of magnitude. How much slower these changes are influences how much adaptation we observe in the step responses. Experiments with time-varying input protocols, namely with double pulse sequences, allow to have a rough estimate of the slower time constant. In olfactory transduction, this time constant is normally associated to the shift in dose-response plots (which is an alternative, compatible, way to describe the multipulse adaptation effect, see Chapter 2, Fig. 2.14). What is predicted by theoretical models and confirmed by experiments is that the speed of the recovery in multipulse adaptation is inversely correlated to the amount of step adaptation. In particular, for the two sensors investigated in this work the relative amount of the two forms of adaptation are different. Both values are coherent with the trade-off proposed.

The main prerequisite for this trade-off to be well-posed, namely that the system in the deactivation phase obeys approximately a linear decay law, is the same mechanism that enables the reset of the output to the pre-stimulus baseline without

undershooting this nominal value. This property of the model is confirmed in the experiments. Also the more fine-graded prediction that, upon perturbation of the natural decay law by means of an altered baseline level, the deactivation transient can become less regular (and undershooting can appear) is validated by our double pulse experiments.

Chapter 4

A dynamical model for the calcium-activated chloride channel in the olfactory transduction

In this chapter we study more in detail a single component of the olfactory transduction pathway, the calcium-activated chloride channel. What could be measured from the experimental data in general is explained in the first part, together with the specific experimental recordings of the Ca-activated Cl channel, appearing in [18]. In Section 4.2 we introduce Markov models which are used to reproduce the behavior of ion channels, and we explain the genesis of our proposed scheme. A description of the models present in literature for the same family of channels is further introduced. The presentation of our results and their discussion close the chapter.

4.1 Background

Ion channels are fundamental bricks in the machinery of a biological system. They are transmembrane proteins able to regulate the flow of various types of ions through the cellular membrane. These proteins allow the selection of a specific intracellular environment and the regulation of the membrane potential. This is strictly related to cell excitability, which permits the transmission of information much quicker than the diffusion rate of molecules. Transmembrane channels are controlled by one or

more external factors, such as the concentration of an agonist or the membrane potential. In response to these agents, they are able to modify the permeability of ions, through a conformational change. This change, at the level of the single channel, causes an alternation between open and closed states [3, 35, 39, 63].

Several types of ion channels are present in the different cells: they can be classified depending on the permeant ions (the type of ions flowing through them), or by their gating (the mechanism which controls the opening of the channel). In particular they can be selective for a single type of ion, or permeable to a bigger class (like cations or anions), and they can be voltage-gated, ligand-gated or both [35].

Modern experimental techniques allow the recording of ionic currents both in the whole cell (or in a part of a membrane) and at the level of a single channel (fluctuating between open and close conformations). The type of data and consequently the analyses required for these experiments are quite different. The first type corresponds to the recording of the sum of thousands of microscopic currents flowing through an equal number of ion channels, mediating the fluctuations of single channel activity. The second instead allows the study of the gating process of the single unit, which consists of discrete changes in conductance over time. Considering the small conductance of the channel we are studying, namely the calcium-activated chloride channel (0.8 pS in frog [53], 1.5 pS in rat [78], 2.6 pS in mouse [72]) and the consequent lack of data due to the difficulty to measure the single channel activity, we have focused our work on the experimental recordings of a population of channels.

In the study of the total current flowing through a population of channels, we have to distinguish between two components: the current flowing through a single channel unit (depending on the conformation of the channel and on the transmembrane potential) and the number of open channels (modified by the potential or by some ligand concentration or by both, depending on the type of the channel). The amount of current can thus be written as:

$$I(V, L, t) = \phi(V) \cdot n(V, L, t) \tag{4.1.1}$$

where V is the transmembrane potential, L is the ligand concentration, n the number of open channels and ϕ the amount of current flowing through the single open channel. Notice that $n(V, L, t)$ can be written as $n(V, L, t) = N \cdot p(V, L, t)$ in which N is a constant and represents the total number of channels contributing to our recordings and p is the probability to have an open channel. In this type of collective experimental recordings we can distinguish the contribution of the single channel current

ϕ and the probability p considering the instantaneous and the steady state currents. Indeed, what we immediately detect in response to a step of the transmembrane potential is the change in current due to the function ϕ, while the channels modifications in response to the change of potential (the change of p) are slower. Thus the profile obtained with the instantaneous current amplitudes in response to different steps of potential is useful to estimate the function ϕ, while the final steady states of the current after the (slower) modification of the amplitude reflect both contributions. In particular, the calcium-activated chloride channel we are considering, has a linear current-voltage relationship for the instantaneous response, meaning that $\phi(V)$ follows Ohm's law and that the conductance of the single channel does not depend on the potential applied ($\phi(V) = g \cdot V$). This reduces equation 4.1.1 to:

$$I(V, L, t) = N \cdot g \cdot V \cdot p(V, L, t) \tag{4.1.2}$$

We can therefore focus our study in the description of $p(V, L, t)$, the probability of the channels of being in the open state. In Section 4.2 we introduce the techniques used to deal with this problem.

4.1.1 Behavior description

As mentioned in the Introduction, the calcium-activated chloride channel present in the olfactory sensory neurons has been identified with the TMEM16B protein. In this section we describe the behavior of the TMEM16B channel, using the data recently obtained in the laboratory of Professor Anna Menini [18]. Following the classification proposed at the beginning of the chapter, TMEM16B belongs to the family of the channels which are permeable to chloride ion and whose gating is regulated by both a ligand, the calcium ion, and the transmembrane potential. The precise dependence of the TMEM16B channel on the two gating mechanisms acting on it and the way in which they are able to modify its structural properties are still unknown. In the present thesis, we mainly consider experiments in which the calcium concentration is held constant during every recording, while the voltage is modified using a step protocol (see Fig. 4.1 A).

Concerning the voltage dependence, the instantaneous current recorded in response to voltage steps is linearly dependent on the potential (see Fig. 4.1 B, filled triangles), meaning that a fraction of channels was open at 0mV (because of the detection of an instantaneous current) and that the single channel conductance g is constant for the different amplitudes of the potential. However it is possible to notice clearly that, after the instantaneous increase of current depending on the

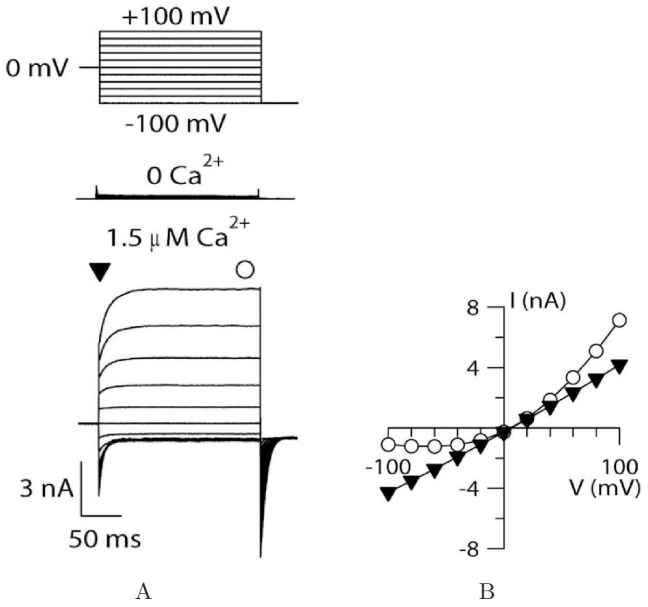

Figure 4.1: **Experimental data: TMEM16B responses and I-V relationship.** A: in the panel above a scheme of the voltage protocol is presented (the cell is held at 0 mV, then exposed to a voltage between -100 mV and +100 mV and finally held at -100 mV); the panels below represent the recoded currents in the case of nominally 0 Ca^{2+} and 1.5 μM Ca^{2+}. B: I-V relations for the instantaneous currents (triangles) and steady state currents (circles) [18].

number of open channels at the time of the change of the potential, the current amplitude is further modified: the voltage contributes to the opening or the closure of a part of channels (in the case respectively of positive or negative potential). This dependence can be seen in the outward rectification of the current-voltage curves at steady state of Fig. 4.1 B (empty circles) and in Fig. 4.2, in which the normalized steady state conductance of the channel ($G = Ngp$ of Eq. (4.1.2) is plotted versus the potential, at different calcium concentrations.

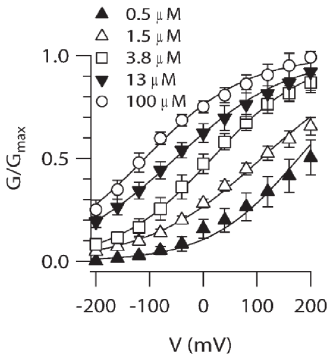

Figure 4.2: **Experimental data: voltage dependence of TMEM16B.** Steady state normalized values of the conductance plotted versus the transmembrane potential, at different concentrations of intracellular Ca^{2+} [18].

Another fundamental actor which influences the behavior of the channel is the calcium ion. In the absence of intracellular calcium the channel cannot open, independently from the potential considered (see Fig.4.1 A). With increasing concentration of calcium, the fraction of open TMEM16Bs increases (Fig. 4.3). In Fig. 4.4 the calcium dependence at different potentials is reported. The curves can be well fitted by the Hill equation: $G = G_{\max}\frac{[Ca^{2+}]^n}{[Ca^{2+}]^n + K_{1/2}^n}$, where $K_{1/2}$ represents the calcium concentration giving the half-maximal activation and n represent the cooperativity index. In literature, n has always been reported to be greater than 1 for this channel [18, 71], meaning that probably the channel has more than one calcium-binding site and that the binding of the second calcium ion is favored with respect to that of the first one. The action of calcium on the channel influences also its voltage dependence. Indeed the outward rectification clearly distinguishable at low calcium concentration decreases with increasing calcium, meaning that at high calcium concentrations the voltage contribution is reduced (see Fig. 4.3).

So far we have focused our attention on the steady state behavior of the TMEM16B

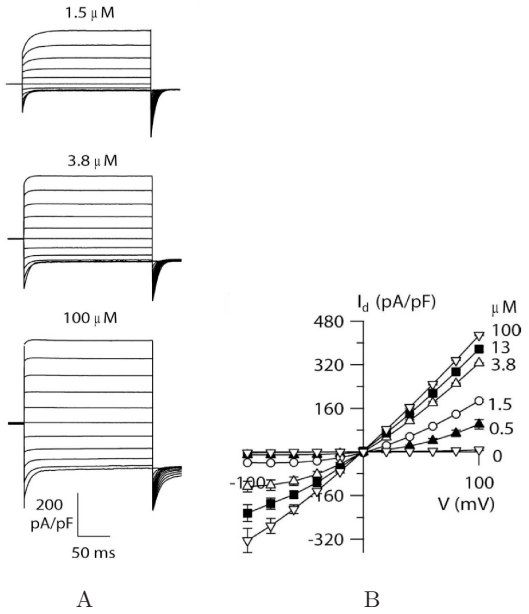

Figure 4.3: **Experimental data: TMEM16B responses and I-V relations at different Ca^{2+} concentrations** [18].

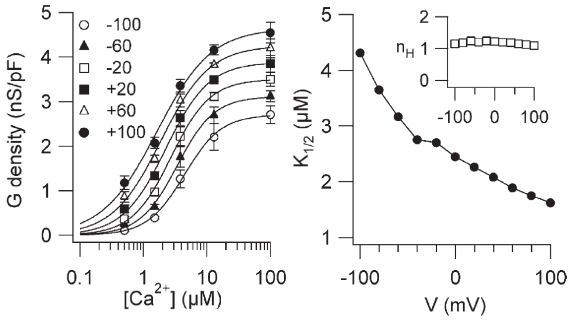

Figure 4.4: **Experimental data: calcium dependence of TMEM16B.** Steady state values of the channel conductance (normalized for the capacity of the single cells) plotted versus the intracellular Ca^{2+} concentration, at different transmembrane potentials [18].

channel. Considering also the dynamic response of the channel could give important clues on its activity. Fitting the time-dependent component of the response with an exponential function like $y = y_0 + A \cdot e^{-t/\tau}$ it is possible to estimate the time constant τ of activation/deactivation of the channel. The experimental data suggest us that the activation time constant decreases with increasing calcium concentration and it is not strongly dependent on the voltage (see Fig. 4.5 A). On the contrary, the deactivation time constant is altered by the potential and increases with increasing calcium (see Fig. 4.5 B). This means that at high calcium concentrations the channel has a fast opening and a slow closure, while it is the opposite at low calcium concentrations.

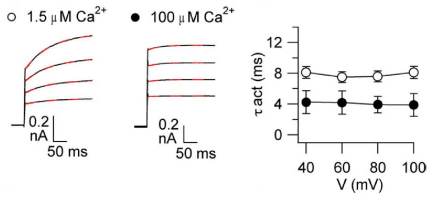

A

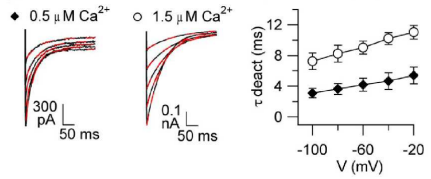

B

Figure 4.5: **Experimental data: dynamic response of TMEM16B.** Calcium and voltage dependence of the time constant values for the transient response of the channel after a positive/negative voltage step, corresponding respectively to the activation/deactivation time constants [18].

4.2 Models

The different structural conformations that an ion channel can assume, can be discretized through a Markov model. A Markov model is a set of open and closed states, interconnected through state transitions. In a Markov process, the system is defined only by its present state and it is independent from its past. At each time interval, there is the probability to switch to a different state, depending on the current state of the system, on the transition rates and on some external factors able to modify the transitions between states.

The simplest scheme for a model of a channel is composed by two states, one open and one closed:

$$\mathrm{C} \underset{k_{-1}}{\overset{k_1}{\rightleftharpoons}} \mathrm{O}$$

where C denotes the closed state, O the open state and k_{-1} and k_1 represent the transition rates. The equation giving the probability p of an open state is:

$$p(t+dt) = p(t)(1-k_{-1}dt) + (1-p(t))k_1 dt \tag{4.2.3}$$

which gives

$$\dot{p}(t) = \lim_{dt\to 0} \frac{p(t+dt)-p(t)}{dt} = -k_{-1}\cdot p(t) + k_1(1-p(t)) \tag{4.2.4}$$

This gives the stationary open distribution and time constant:

$$p_\infty = \frac{k_1}{k_1+k_{-1}} \tag{4.2.5}$$

$$\tau = \frac{1}{k_1+k_{-1}} \tag{4.2.6}$$

and, denoting $p(0) = p_0$ the initial condition,

$$p(t) = p_\infty - (p_\infty - p_0)e^{-t/\tau} \tag{4.2.7}$$

Equation (4.2.7) gives the evolution of the open probability of the channel when exposed to a change in the voltage or in the ligand concentration (depending on the type of channel), before reaching the new equilibrium state. Both the ligand concentration and the transmembrane potential can appear in this scheme by modifying the rate constants (becoming $k_1(L,V)$ and/or $k_2(L,V)$).

Starting from this simple scheme, it is possible to build more complicated schemes,

in which multiple closed and open states are present and every transition between two states is developed as described above.

4.2.1 Toward the creation of a model for the chloride channel

Similarly to the simple model just presented, to reproduce the behavior of the channel and to understand its voltage and calcium dependence, we chose to represent it through a Markov process. For clarity, we use the letter k to refer to calcium-dependent transitions (and K for the equilibrium constants e.g. k_{-1}/k_1) and α and β for the voltage-dependent ones. The calcium dependence is modeled considering a direct proportionality between the binding rate constants and calcium concentration. Following [5, 50], we use exponential functions for α and β dependence on the potential:

$$\alpha(V) = \alpha_0 \cdot e^{\frac{V}{s_\alpha}}; \tag{4.2.8}$$

$$\beta(V) = \beta_0 \cdot e^{-\frac{V}{s_\beta}}. \tag{4.2.9}$$

where V represents the transmembrane potential and α_0, β_0, s_α and s_β are constants. The output of the model is a current which is proportional to the sum of the fraction of channels in the open states. A direct proportionality has been chosen because of the linear instantaneous current-voltage relation, meaning that the single channel conductance is not affected by the potential (see Section 4.1).

In every configuration we have considered, the transition depending on the calcium contribution is upstream (and therefore necessary for) the opening of the channel. This choice is due to the fact that the channel, regardless of the value of the voltage, is not capable of opening in the total absence of calcium (see 4.1 A and [18]).

In the experimental data considered, the transmembrane potential applied to the cell span from -200 mV to 200 mV and the calcium concentration from 0.5 μM to 100 μM. Hereafter we will consider as "low" concentrations of calcium values below 1 μM and "high" concentrations values above 10 μM.

3-state schemes We started considering the simplest schemes allowing us to distinguish between the action of the voltage and of the calcium concentration on the channel. Following [5], in order to study the qualitative behavior of these models with an analytical approach it is possible to hypothesize that the transition between the closed and the open state is much slower than the other transitions (that we can assume in equilibrium). This allows us to reduce the 3-state schemes to simpler

close-open configurations in which the voltage and the calcium contributions are combined together. The resulting system has now a single eigenvalue, reciprocal to the time constant of the system τ ($\lambda = -1/\tau$).

Two different cases of this 3-state scheme and consequent reduction are now discussed in some detail.

- Model 1

$$C_0 \underset{\beta}{\overset{\alpha}{\rightleftharpoons}} C_1 \underset{k_{-1}}{\overset{k_1 \cdot [\mathrm{Ca}]}{\rightleftharpoons}} \mathrm{O}$$

The corresponding equations are:

$$\begin{aligned} \dot{C_0} &= -\alpha \cdot C_0 + \beta \cdot C_1 \\ \dot{C_1} &= \alpha \cdot C_0 - \beta \cdot C_1 - k_1 \cdot [\mathrm{Ca}] \cdot C_1 + k_{-1} \cdot O \\ \dot{O} &= k_1 \cdot [\mathrm{Ca}] \cdot C_1 - k_{-1} \cdot O \end{aligned} \tag{4.2.10}$$

It is now possible to reduce this model to a simple close-open model. Under the assumption of a fast $C_0 - C_1$ transition we can obtain from the first equation of system (4.2.10):

$$C_{0ss} = \frac{\beta}{\alpha} \cdot C_1 \tag{4.2.11}$$

Denoting $C = C_0 + C_1$ the closed state of the reduced model we obtain:

$$C_1 = \frac{1}{1 + \frac{\beta}{\alpha}} \cdot C \tag{4.2.12}$$

Therefore the equations for the new system become:

$$\begin{aligned} \dot{C} &= -\frac{k_1 \cdot [\mathrm{Ca}]}{1 + \frac{\beta}{\alpha}} \cdot C + k_{-1} \cdot O \\ \dot{O} &= \frac{k_1 \cdot [\mathrm{Ca}]}{1 + \frac{\beta}{\alpha}} \cdot C - k_{-1} \cdot O \end{aligned} \tag{4.2.13}$$

which correspond to the reduced configuration

$$C \underset{k_{-1}}{\overset{\frac{k_1 \cdot [\mathrm{Ca}]}{1 + \frac{\beta}{\alpha}}}{\rightleftharpoons}} \mathrm{O}$$

For this configuration the steady state percentage of the open channels p_{ss} and the time constant of the transition τ are:

$$p_{ss} = \frac{1}{1+\frac{k_{-1}}{k_1\cdot[\mathrm{Ca}]}\cdot(1+\frac{\beta}{\alpha})}; \tag{4.2.14}$$

$$\tau = \frac{1+\frac{\beta}{\alpha}}{k_1\cdot[\mathrm{Ca}]+k_{-1}\cdot(1+\frac{\beta}{\alpha})}. \tag{4.2.15}$$

This type of model correctly reproduces, from a qualitative point of view, both the steady states curves of Fig. 4.2 and 4.4. τ diminishes with increasing concentration of calcium in the activation phase of the channel at positive potential (for V$\gg$ 0, $\beta \to 0$), as in the experimental data, but it becomes independent from calcium concentration in the deactivation phase at negative potential (for V$\ll$ 0, $\beta \to \infty$). Moreover, even at intermediate transmembrane potential (when $k_1\cdot[\mathrm{Ca}] \simeq k_{-1}\frac{\beta}{\alpha}$), τ is inversely proportional to the concentration of calcium. For this reason Model (4.2.10) cannot reproduce correctly the behavior of the channel, in which the activation time constant diminishes with increasing calcium, while the deactivation time constant increases in the presence of more calcium.

- Model 2

  An alternative scheme consists in inverting the order of the Ca and V transitions.

$$C_0 \underset{k_{-1}}{\overset{k_1\cdot[\mathrm{Ca}]}{\rightleftharpoons}} C_1 \underset{\beta}{\overset{\alpha}{\rightleftharpoons}} \mathrm{O}$$

  The corresponding equations are:

$$\begin{aligned} \dot{C_0} &= -k_1\cdot[\mathrm{Ca}]\cdot C_0 + k_{-1}\cdot C_1 \\ \dot{C_1} &= k_1\cdot[\mathrm{Ca}]\cdot C_0 - k_{-1}\cdot C_1 - \alpha\cdot C_1 + \beta\cdot O \\ \dot{O} &= \alpha\cdot C_1 - \beta\cdot O. \end{aligned} \tag{4.2.16}$$

  Still under the equilibrium assumption for the $C_0 - C_1$ transitions, the $\mathrm{p_{ss}}$ and the τ can be calculated as described above, and become as follows:

$$p_{ss} = \frac{1}{1+\frac{\beta}{\alpha}\cdot(1+\frac{k_{-1}}{k_1\cdot[\mathrm{Ca}]})}; \tag{4.2.17}$$

$$\tau = \frac{1+\frac{k_{-1}}{k_1\cdot[\mathrm{Ca}]}}{\alpha+\beta\cdot(1+\frac{k_{-1}}{k_1\cdot[\mathrm{Ca}]})}. \tag{4.2.18}$$

This scheme correctly captures the stationary behavior of Fig. 4.2 and 4.4 and the calcium dependence of the activation τ at positive potential (diminishing with increasing calcium concentration). However it does not reproduce the deactivation τ at negative potential, which results constant for every concentration of calcium ($\tau \to 1/\beta$, thus depending only on the potential). Adding more calcium bindings before the close-open transition does not modify this feature.

4-state scheme As we have shown in the previous paragraph, it is not possible to correctly capture the slower closure of the channel due to the increasing of the calcium concentration without adding in the scheme at least one calcium-dependent transition after a close-open transition. This consideration led us to the following scheme:

$$C_0 \underset{k_{-1}}{\overset{k_1 \cdot [\mathrm{Ca}]}{\rightleftharpoons}} C_1 \underset{\beta}{\overset{\alpha}{\rightleftharpoons}} O_1 \underset{k_{-2}}{\overset{k_2 \cdot [\mathrm{Ca}]}{\rightleftharpoons}} O_2$$

of equations:

$$\begin{aligned} \dot{C_0} &= -k_1 \cdot [\mathrm{Ca}] \cdot C_0 + k_{-1} \cdot C_1 \\ \dot{C_1} &= k_1 \cdot [\mathrm{Ca}] \cdot C_0 - k_{-1} \cdot C_1 - \alpha \cdot C_1 + \beta \cdot O \\ \dot{O_1} &= \alpha \cdot C_1 - \beta \cdot O_1 - k_2 \cdot [\mathrm{Ca}] \cdot O_1 + k_{-2} \cdot O_2 \\ \dot{O_2} &= k_2 \cdot [\mathrm{Ca}] \cdot O_1 - k_{-2} \cdot O_2. \end{aligned} \tag{4.2.19}$$

Still under our assumption of a slower transition for the close-open process with respect to the transitions among closed states or open states (thus hypothesizing the steady state for the calcium binding-unbinding transitions), we reduced this scheme to a two state model in which:

$$p_{ss} = \frac{1 + \frac{k_2 \cdot [\mathrm{Ca}]}{k_{-2}}}{1 + \frac{k_2 \cdot [\mathrm{Ca}]}{k_{-2}} + \frac{\beta}{\alpha}(1 + \frac{k_{-1}}{k_1 \cdot [\mathrm{Ca}]})}; \tag{4.2.20}$$

$$\tau = \frac{(1 + \frac{k_{-1}}{k_1 \cdot [\mathrm{Ca}]})(1 + \frac{k_2 \cdot [\mathrm{Ca}]}{k_{-2}})}{\alpha(1 + \frac{k_2 \cdot [\mathrm{Ca}]}{k_{-2}}) + \beta(1 + \frac{k_{-1}}{k_1 \cdot [\mathrm{Ca}]})}. \tag{4.2.21}$$

In this case, we have a second binding of calcium which "stabilizes" the opening of the channel. Consequently the deactivation time constant at negative potential correctly increases with increasing concentration of calcium, while the activation time constant at positive potential decreases with increasing calcium. However,

considering Eq. (4.2.20), it is possible to notice how, unless we select a $K_2 = \frac{k_{-2}}{k_2}$ ratio very large (meaning an "anti-cooperative" behavior for the binding of the second ion of calcium), at high calcium concentration at positive potential the open probability is equal to one independently from the value of the voltage. In the experimental data, the binding of calcium displays a cooperative behavior, as the cooperativity index of the Hill curve (see Fig.4.4) is greater than one. Moreover the maximal conductance in the dose-response plot (Fig.4.4) is clearly still dependent on the potential. Also in this scheme adding more calcium bindings before or after the close-open transition does not modify this feature.

The final scheme The simplest model able to reproduce, in addition to the other features, the slower closure of the channel in the presence of a high concentration of calcium, being at the same time qualitatively different from the 4-states scheme presented above, is shown in Fig. 4.6 A. The horizontal connections represent the

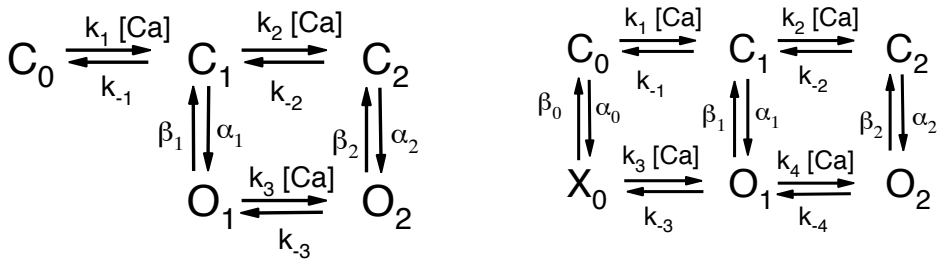

Figure 4.6: **Possible schemes for TMEM16B.** The scheme in B is derived by the scheme in A adding the possibility of a modification of the channel due to the transmembrane potential even in the absence of intracellular calcium.

binding/unbinding of the calcium ion to the channel and the vertical ones correspond to the opening and closing to the channel due to the voltage action. In this case two different opening/closing transitions are present: the first from the state C_1 to the state O_1 representing the dynamics of the channel with one bound calcium ion (thus predominant at low and intermediate concentrations of calcium), the second $C_2 - O_2$ for the case in which two calcium ions are bound to the channel (becoming important at high calcium concentrations). This double close-open transition allows us to reproduce different time constants in the dynamics of the channel depending on the concentration of calcium. To entail the possibility of a modification of the channel due to the action of the transmembrane potential even in the absence of

calcium, we modify the scheme of Fig. 4.6 A into that of Fig. 4.6 B. We have called X_0 the newly introduced state representing this configuration of the channel, to underline the peculiarity of this condition, corresponding to an open state from a conformational point of view, but still not conducting current because of the absence of calcium. The corresponding equations for the scheme of Fig. 4.6 B are:

$$\begin{aligned}
\dot{C}_0 &= -k_1 \cdot [\mathrm{Ca}] \cdot C_0 + k_{-1} \cdot C_1 - \alpha_0 \cdot C_0 + \beta_0 \cdot X_0 \\
\dot{C}_1 &= k_1 \cdot [\mathrm{Ca}] \cdot C_0 - k_{-1} \cdot C_1 - k_2 \cdot [\mathrm{Ca}] \cdot C_1 + k_{-2} \cdot C_2 - \alpha_1 \cdot C_1 + \beta_1 \cdot O_1 \\
\dot{C}_2 &= k_2 \cdot [\mathrm{Ca}] \cdot C_1 - k_{-2} \cdot C_2 - \alpha_2 \cdot C_2 + \beta_2 \cdot O_2 \\
\dot{X}_0 &= -k_3 \cdot [\mathrm{Ca}] \cdot X_0 + k_{-3} \cdot O_1 + \alpha_0 \cdot C_0 - \beta_0 \cdot X_0 \\
\dot{O}_1 &= k_3 \cdot [\mathrm{Ca}] \cdot X_0 - k_{-3} \cdot O_1 - k_4 \cdot [\mathrm{Ca}] \cdot O_1 + k_{-4} \cdot O_2 + \alpha_1 \cdot C_1 - \beta_1 \cdot O_1 \\
\dot{O}_2 &= k_4 \cdot [\mathrm{Ca}] \cdot O_1 - k_{-4} \cdot O_2 + \alpha_2 \cdot C_2 - \beta_2 \cdot O_2
\end{aligned} \tag{4.2.22}$$

We have not added further binding-unbinding transitions (and corresponding open states) for calcium binding because our aim was to find the simplest model able to reproduce the main features of the TMEM16B channel and the estimated Hill coefficient from the experimental data was only slightly greater than one [18].

We chose to distinguish two different open states because of the presence of (at least) two different dynamics of the channel in low or high concentrations of calcium (there should be two different close-open transitions). The possibility to mesh together this two open states was not considered due to its physiological meaning: the two open states represent the open channel with one or two bound calcium ions. Thus a single state representing both conditions could have led to misunderstandings about the number of ions bound to the channel and it would not have been possible to impose that a channel open through $C_1 - O$ could not close through $O - C_2$ and viceversa. Allowing this, the channel would gain a calcium ion without any calcium dependence and this transition would be preferred in the case of low calcium concentration, in which the state C_2 is less populated than C_1.

Moreover we noticed that the fit improved allowing the transition between the two open states and X_0 and O_1, confirming our idea that the binding of the calcium ion is possible in both the closed and the open channel. We constrained the equilibrium binding contants $K_i = k_{-i}/k_i$, $i = 1, 2, 3, 4$ to be equal for all the transitions. Furthermore hypothesizing that the binding rate is not affected by the presence of an ion already bound to the channel, the value for the constants of the transitions between closed states are set to be equal and the same for the transitions $X_0 - O_1 - O_2$.

4.2.2 State-of-art of models for the calcium-activated chloride channel

Possible schemes for the dynamics of the calcium-activated chloride channels have been investigated by different groups ([5], reconsidered by [32], and [50], further developed also by [4]).

Arreola and colleagues [5] proposed a 4-states scheme in which only one open state was present:

$$C_0 \underset{\beta_1}{\overset{\alpha_1 \cdot [\mathrm{Ca}]}{\rightleftharpoons}} C_1 \underset{\beta_1}{\overset{\alpha_1 \cdot [\mathrm{Ca}]}{\rightleftharpoons}} C_2 \underset{\beta_2}{\overset{\alpha_2}{\rightleftharpoons}} \mathrm{O}$$

In this scheme they hypothesized two consecutive binding of calcium to the closed channel, regulated by the ligand concentration and by the transmembrane potential. The final step, responsible for the opening of the channels, is instead dependent only on the potential. The binding affinity is equal for both the binding steps and in the transition between C_2 and O the dependence on the potential is only through the closing rate β_2, using an exponential function as Eq. (4.2.9) (α_2 is constant). Moreover they considered the instantaneous component of the current due to the a very fast calcium binding kinetics and they consequently assumed the steady state for the first two transitions $C_0 - C_1$ and $C_1 - C_2$ while studying the opening dynamics. This allowed them to reduce the scheme as the simpler 2 states scheme presented earlier and to study the kinetics of the reduced model, as shown in the previous subsection. The scheme correctly reproduced the steady state values of the current and the different instantaneous currents which increase with increasing calcium concentrations after a voltage step, but was not able to represent the slow closure of the channel at high amounts of calcium.

An alternative scheme was presented by the group of Hartzell [50] (see Fig. 4.7). They distinguished seven possible states for the calcium-activated chloride channel, four closed and three open. The transitions between closed states are calcium-dependent, while the transition between closed and open states are voltage-dependent. Transitions between open states are not allowed. The rate constants accounting for the binding/unbinding of calcium are equal for the binding of the first, second and third calcium ion. The rate constants for the opening of the channel are instead different for the three transitions, they are not depending on the transmembrane potential and they increase in transitions between states with more ions of calcium bound to the channel ($\alpha_1 < \alpha_2 < \alpha_3$). The closure of the channel is voltage-dependent (through an exponential function like Eq. (4.2.9)) and equal for the three possible closing transitions present in the scheme. This model was tested in simula-

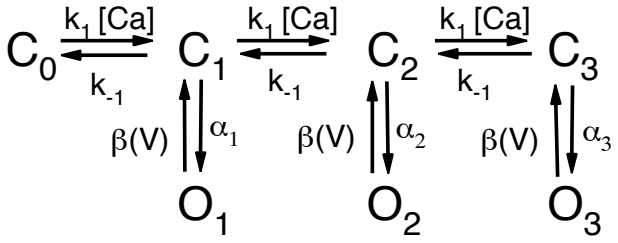

Figure 4.7: **The scheme proposed by Kuruma and Hartzell in [50].**

tions of responses to voltage steps between -120 and +120 mV, at a given concentration of calcium, and of responses to calcium steps, with the potential held constant for all the duration of the simulation. In both cases the activation of the channel became faster with increasing calcium concentrations, as in the experimental data. The outward rectification of the current response present in the experimental data gradually becoming less pronounced at high calcium concentration is also correctly reproduced. On the contrary, the model fails to reproduce the slow closure of the channel at high calcium concentration. Moreover in the closure of the channel after a step of calcium, it predicted a slower deactivation time constant for 50 μM Ca^{2+} than for 500 nM Ca^{2+}, a difference not detected in the experimental data.

4.3 Results

We fit the model (4.2.22) to experimental recordings of the type shown in Figs. 4.1, 4.2 and 4.3 through a least square algorithm similar to that described in the previous chapters. The corresponding parameters are reported in Table 4.1.

In Fig. 4.8 the responses of the model of Fig. 4.6 B are shown. The calcium concentration was held constant for all the duration of the simulation, while the potential stepped from 0 mV to different values between -200 mV and +200 mV, then to -200 mV and finally back to 0 mV. These data correctly capture both the steady states values and the time dependent profiles of the experimental data. The steady state dependence on the potential can be seen in Fig. 4.9. The model reproduces the sigmoidal shape of the dependence of p_{open} with respect to V and the shift of this curve towards smaller transmembrane potential values with increasing calcium concentrations. Notice that at 0 mV the open probability of the channel is greater than 0, despite of the fact that the current is equal to 0. This allows to

Table 4.1: Parameter set used to fit the data of Fig. 4.1, 4.3 and 4.2.

Parameter	Value	Parameter	Value
α_{00}	219.2	β_{00}	1038
$s_{\alpha 0}$	0.43	$s_{\beta 0}$	1
α_{01}	14.5	β_{01}	27
$s_{\alpha 1}$	0.05	$s_{\beta 1}$	0.05
α_{02}	103	β_{02}	21.6
$s_{\alpha 2}$	0.15	$s_{\beta 2}$	0.17
k_1,k_2	1137	K_1,K_2	2.3
k_3,k_4	67.4	K_3,K_4	2.3

reproduce the instantaneous currents detected in response to the voltage steps and is achieved through an exponential dependence of the voltage-dependent transitions α and β (see Eqs (4.2.8), (4.2.9)). An explicit calcium dependence of these simulated traces is represented in Fig. 4.10. These curves have been fitted like the experimental data to the Hill equation $\frac{G}{G_{max}} = \frac{[Ca^{2+}]^{n_h}}{[Ca^{2+}]^{n_h}+K_{1/2}^{n_h}}$. On the right panels of Fig. 4.10 it is possible to visualize the estimated half-maximal intracellular calcium concentration $K_{1/2}$ (above) and the cooperativity number n_h (below). The dependence of $K_{1/2}$ to the transmembrane potential is similar to the profile obtained from the experimental data (see Fig. 4.4). The cooperativity index n_h seems to be not modified by the voltage and slightly greater than one, as in Fig. 4.4.

As previously mentioned the transient dynamics of the channel have been also considered. The traces of the simulated data presented in Fig. 4.8 have been fitted with the exponential function $y = y_0 + A \cdot e^{-t/\tau}$, in order to estimate the time constant τ of activation/deactivation of the *in silico* channel and compare it with that of the experimental data. The time constants at different calcium concentrations and their dependence on the transmembrane potential are reproduced in Fig. 4.11. The simulated data correctly captures the opening time constant of the channel after a voltage step, which is fast in the case of a high calcium concentration and increases at lower concentrations. On the contrary the closure of the channel following a negative potential step is faster in the presence of a small calcium amount. This means that a high calcium concentration not only enhances the steady state open probability of the channel, but also influences the dynamic response contributing to accelerate the opening and to slow down the closure of the channel, as in the experimental data. As can be noticed in Fig. 4.11, τ is also dependent on the transmembrane potential and it decreases at lower voltages during the closure of the

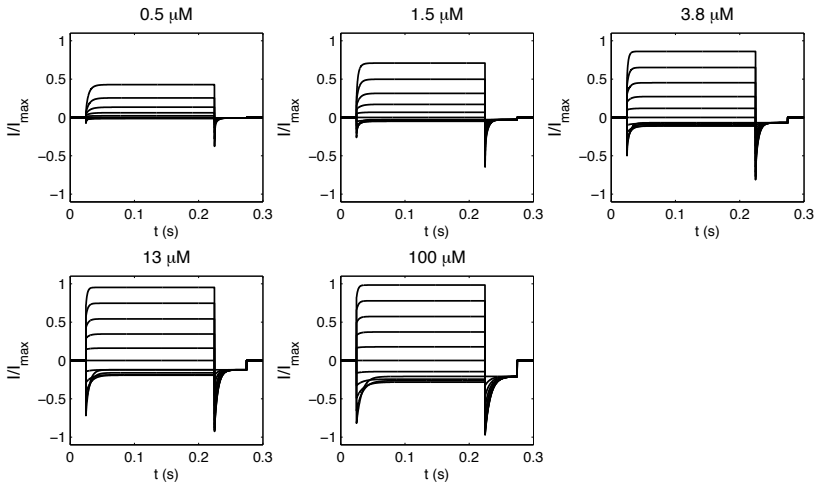

Figure 4.8: **Simulated data resembling those of Figs. 4.1, 4.3.**

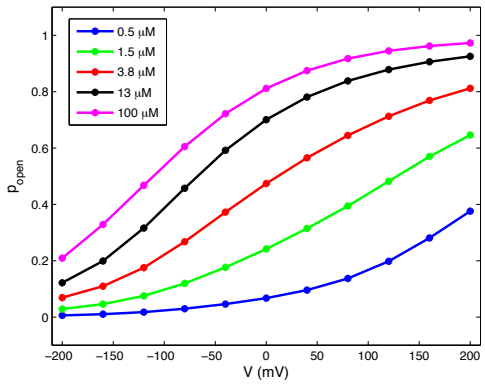

Figure 4.9: **Simulated data: voltage dependence.** Steady state current values reported versus the transmembrane potential, at different intracellular calcium concentrations. The corresponding experimental data are shown in Fig. 4.2

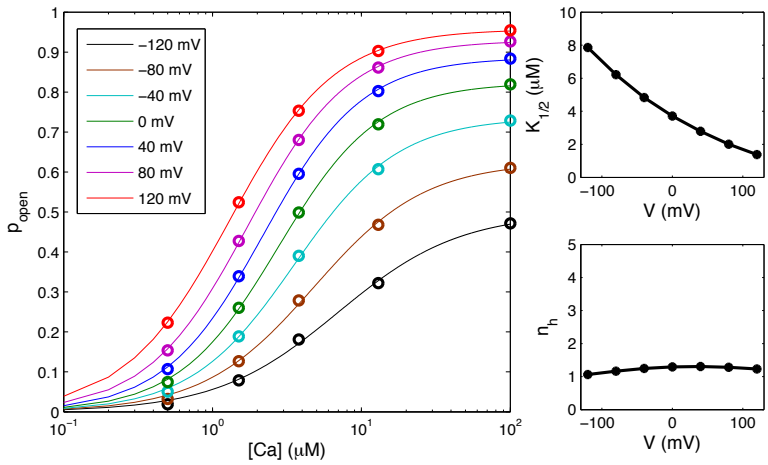

Figure 4.10: **Simulated data: calcium dependence.** Steady state current values reported versus the calcium concentration, half-maximal calcium concentration $K_{1/2}$ and cooperativity number n_h values, to be compared with those of Fig. 4.4. The voltage of the simulation is changed from -120 mV to 120 mV.

channel, reflecting the behavior of the experimental data (see Fig. 4.5). Regarding the channel opening, the model predicts a decreasing activation time constant at positive potential, which cannot be seen in the experimental profiles. However, given a certain calcium concentration, the experimental time constants at positive voltages are smaller than those at negative voltages, meaning that the function relating τ and V cannot be monotonically increasing and consequently that the constant experimental τ at the considered values of V could decrease at higher potentials.

4.4 Discussion

As introduced in the Methods section, different Markov models have been studied to explain the behavior of the calcium-activated chloride channel. The first was introduced by Arreola and collaborators [5] presenting data of the native channel in rat parotid acinar cells. They noticed from the experimental data that the current flowing through the channel increases with increasing intracellular calcium concentration and that the responses to a voltage step were composed by an instantaneous and a slower components. The proposed scheme (see Subsection 4.2.2) contains a

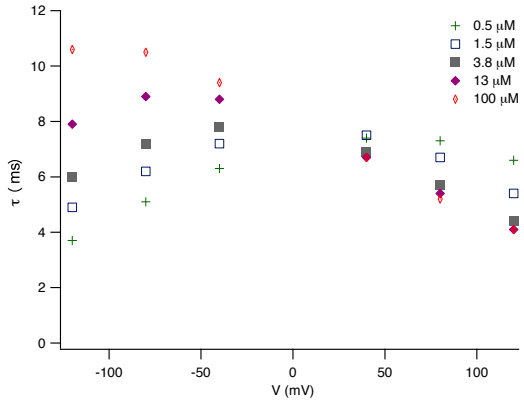

Figure 4.11: **Simulated data: time constant of the channel in response to voltage step.** The time constant of the current response is reported in dependence of the voltage value (changing from -120 mV to 120 mV) and of intracellular calcium concentration (see Fig. 4.5 for a comparison).

single open state and consequently a single close-open transition, which depends only on the transmembrane potential and not on the calcium concentration. This means that if the amount of calcium can influence the steady state current and the activation time, it cannot modify the deactivation time, i.e. the time needed to the channel to modify its state from open to close. Therefore the proposed model cannot reproduce the slow closure of the current in the presence of a high calcium concentration.

A similar scheme was presented by Haase and Hartung in 2006 [32] to explain the behavior of the calcium-activated chloride channel in *Xenopus* oocytes. The main difference between the two models is that in [32] an inactivated state was added, to account for the inactivation exhibited by the channel in response to voltage steps. They consequently focused their studies on the activation current profiles in response to positive voltage steps, which consisted in a fast transient followed by a slower voltage-independent activation. In particular they did not study the inactivation time constant of the channel in response to negative voltage step, which was the main feature not correctly reproduced by the model proposed in [5].

In 2000 Kuruma and Hartzell [50] introduced a very different scheme (afterwards considered also in [4]) for the calcium-activated chloride channels in *Xenopus* oocytes. They did not detect the deactivation phase subsequently measured in [32]. The *in silico* data of the responses of the channel to voltage and calcium concentra-

tion steps were compared with the experimental data. In response to a step of Ca^{2+} the opening of the channel becomes faster with increasing calcium concentration both in the simulations and in the experimental data, while the closure of the channel is slower at high Ca^{2+} only in the simulated data (they did not found a similar dependence on calcium concentration in the experimental recordings). The same scheme was tested for voltage steps responses and, at high calcium concentration, it correctly reproduced the fast activation time constant but not the slower closure of the channel following a negative voltage step.

The schemes of Fig. 4.6 we are presenting in this thesis resemble that of Kuruma and Hartzell [50]. We did not consider the states C_3 and O_3 (accounting for the binding of the third calcium ion to the channel) because they turned out to be not fundamental in reproducing the data. Moreover we added transitions between open states to account for the possibility that the binding of calcium could occur even in the case of an open channel, stabilizing this opening. In the scheme of Fig. 4.6 B we also added a further closed state X_0 representing the action of the transmembrane potential on the closed channel in the case of nominally zero calcium concentration.

Following these considerations and the results shown in [50] and [104] a new type of experimental data have been recorded recently. Using a photorelease protocol similar to that of the caged compounds in Chapter 2, the channel (previously held at nominally zero calcium) have been exposed to a fast release of intracellular calcium. This protocol allows the emission of different calcium concentrations through shieldings of the uncaging light, at various constant transmembrane potentials. The recorded currents exhibit an extremely fast activation (with a time constant below 5 ms) both at +50 mV and -50 mV at a high flash intensity (high calcium concentration) and a slower response ($\tau \sim$10 ms, both at +50 mV and -50 mV) in the case of a shield for 96.8% of the light (corresponding to a low calcium concentration).

These data suggest the possibility that the channel could "be prepared" to the opening by the transmembrane potential, confirming our idea of the presence of a state X_0 in which the channel is still close (no current flows through the channel), but it is prompter for the opening with respect to the state C_0. Upon the arrival of the calcium ion the channel in this state opens rapidly and the opening time constant depend only on the calcium amount. On the contrary, in the absence of the state X_0, it would be impossible to obtain a smaller opening time constant in the experiments in which the channel undergoes a sudden change of calcium concentration (while keeping constant the voltage) compared to the voltage step experiments (at constant calcium). Indeed in a scheme as that presented in Fig. 4.6 A, in the

absence of calcium all the population of channel is in the state C_0, independently of the transmembrane potential. When calcium is released, the channel opening must occur through the transitions $C_0 - C_1 - O_1$ or $C_0 - C_1 - C_2 - O_2$. In the voltage step experiments calcium is already present and at the constant potential of 0 mV the population of the channels is distributed between all the states. Thus, after a positive voltage step, we would expect an instantaneous current accounting for the already open channels, followed by a fast opening of the remaining current (faster than the response to a calcium release). The minimum modification of the scheme of Fig. 4.6 A to account for this difference, is the introduction of the state X_0 of Fig. 4.6 B. In this case, when the channel is held at a given potential and nominally zero calcium amount, the population of the channels is distributed between states C_0 and X_0. After the calcium release, the channel has the possibility to open through the $X_0 - O_1$ transition, which could be faster than those between $C_0 - C_1 - O_1$ and $C_0 - C_1 - C_2 - O_2$ and is by definition only depending on the calcium concentration.

Clearly at a given calcium concentration and a fixed potential, the steady states of the simulated currents are independent from the history of the channel (i.e. independent from the type of experiment). The difference between the two experiments lies in the initial conditions and in the time constants of the transient current, meaning that the response to a given experimental protocol depends on the order of the input.

We are going to focus our future studies on this interesting behavior, investigating the model responses and the necessary dynamical features in order to correctly reproduce it.

Bibliography

[1] U Alon, M G Surette, N Barkai, and S Leibler. Robustness in bacterial chemotaxis. *Nature*, 397(6715):168–171, Jan 1999.

[2] Uri Alon. *An Introduction to Systems Biology: Design Principles of Biological Circuits (Chapman & Hall/CRC Mathematical & Computational Biology)*. Chapman and Hall/CRC, 1 edition, July 2006.

[3] T Andersson. Exploring voltage-dependent ion channels in silico by hysteretic conductance. *Math Biosci*, 226(1):16–27, Jul 2010.

[4] J E Angermann, A R Sanguinetti, J L Kenyon, N Leblanc, and I A Greenwood. Mechanism of the inhibition of Ca^{2+}-activated Cl^{-} currents by phosphorylation in pulmonary arterial smooth muscle cells. *J Gen Physiol*, 128(1):73–87, Jul 2006.

[5] J Arreola, J E Melvin, and T Begenisich. Activation of calcium-dependent chloride channels in rat parotid acinar cells. *J Gen Physiol*, 108(1):35–47, Jul 1996.

[6] S Balasubramanian, J W Lynch, and P H Barry. Calcium-dependent modulation of the agonist affinity of the mammalian olfactory cyclic nucleotide-gated channel by calmodulin and a novel endogenous factor. *J Membr Biol*, 152(1):13–23, Jul 1996.

[7] N Barkai and S Leibler. Robustness in simple biochemical networks. *Nature*, 387(6636):913–917, Jun 1997.

[8] M Behar, N Hao, H G Dohlman, and T C Elston. Mathematical and computational analysis of adaptation via feedback inhibition in signal transduction pathways. *Biophys J*, 93(3):806–821, Aug 2007.

[9] G M Billig, B Pál, P Fidzinski, and T J Jentsch. Ca^{2+}-activated Cl^- currents are dispensable for olfaction. *Nat Neurosci*, 14(6):763–769, Jun 2011.

[10] C Biskup, J Kusch, E Schulz, V Nache, F Schwede, F Lehmann, V Hagen, and K Benndorf. Relating ligand binding to activation gating in CNGA2 channels. *Nature*, 446(7134):440–443, Mar 2007.

[11] A Boccaccio, L Lagostena, V Hagen, and A Menini. Fast adaptation in mouse olfactory sensory neurons does not require the activity of phosphodiesterase. *J Gen Physiol*, 128(2):171–184, Aug 2006.

[12] A Boccaccio and A Menini. Temporal development of cyclic nucleotide-gated and Ca^{2+}-activated Cl^- currents in isolated mouse olfactory sensory neurons. *J Neurophysiol*, 98(1):153–160, Jul 2007.

[13] F F Borisy, G V Ronnett, A M Cunningham, D Juilfs, J Beavo, and S H Snyder. Calcium/calmodulin-activated phosphodiesterase expressed in olfactory receptor neurons. *J Neurosci*, 12(3):915–923, Mar 1992.

[14] J Bradley, W Bönigk, K W Yau, and S Frings. Calmodulin permanently associates with rat olfactory CNG channels under native conditions. *Nat Neurosci*, 7(7):705–710, Jul 2004.

[15] Marie E Burns and Denis A Baylor. Activation, deactivation, and adaptation in vertebrate photoreceptor cells. *Annual Review of Neuroscience*, 24(1):779–805, 2001.

[16] E Butt, D Pöhler, H G Genieser, J P Huggins, and B Bucher. Inhibition of cyclic GMP-dependent protein kinase-mediated effects by (Rp)-8-bromo-PET-cyclic GMPS. *Br J Pharmacol*, 116(8):3110–3116, Dec 1995.

[17] A Caputo, E Caci, L Ferrera, N Pedemonte, C Barsanti, E Sondo, U Pfeffer, R Ravazzolo, O Zegarra-Moran, and L J Galietta. TMEM16A, a membrane protein associated with calcium-dependent chloride channel activity. *Science*, 322(5901):590–594, Oct 2008.

[18] V Cenedese, G Betto, F Celsi, O L Cherian, S Pifferi, and A Menini. The voltage dependence of the TMEM16B/anoctamin2 calcium-activated chloride channel is modified by mutations in the first putative intracellular loop. *J Gen Physiol*, 139(4):285–294, Apr 2012.

[19] T Y Chen and K W Yau. Direct modulation by Ca^{2+}-calmodulin of cyclic nucleotide-activated channel of rat olfactory receptor neurons. *Nature*, 368(6471):545–548, Apr 1994.

[20] Cheryl D. Condon and Norman M. Weinberger. Habituation produces frequency-specific plasticity of receptive fields in the auditory cortex. *Behavioral Neuroscience*, 105(3):416 – 430, 1991.

[21] G De Palo, F Eduati, M Zampieri, B Di Camillo, G Toffolo, and C Altafini. Adaptation as a genome-wide autoregulatory principle in the stress response of yeast. *IET Syst Biol*, 5(4):269–279, Jul 2011.

[22] D P Dougherty, G A Wright, and A C Yew. Computational model of the cAMP-mediated sensory response and calcium-dependent adaptation in vertebrate olfactory receptor neurons. *Proc Natl Acad Sci U S A*, 102(30):10415–10420, Jul 2005.

[23] G. L. Fain, H. R. Matthews, M. C. Cornwall, and Y. Koutalos. Adaptation in vertebrate photoreceptors. *Physiological reviews*, 81(1):117–151, 2001.

[24] E E Fesenko, S S Kolesnikov, and A L Lyubarsky. Induction by cyclic gmp of cationic conductance in plasma membrane of retinal rod outer segment. *Nature*, 313(6000):310–313, Jan 1985.

[25] S Firestein, C Picco, and A Menini. The relation between stimulus and response in olfactory receptor cells of the tiger salamander. *J Physiol*, 468:1–10, Aug 1993.

[26] S Firestein, G M Shepherd, and F S Werblin. Time course of the membrane current underlying sensory transduction in salamander olfactory receptor neurones. *J Physiol*, 430:135–158, Nov 1990.

[27] S Forti, A Menini, G Rispoli, and V Torre. Kinetics of phototransduction in retinal rods of the newt triturus cristatus. *J Physiol.*, 419:265–295, 1989.

[28] T Friedlander and N Brenner. Adaptive response by state-dependent inactivation. *Proc Natl Acad Sci U S A*, 106(52):22558–22563, Dec 2009.

[29] T V Getchell. Functional properties of vertebrate olfactory receptor neurons. *Physiol Rev*, 66(3):772–818, Jul 1986.

[30] T V Getchell and G M Shepherd. Adaptive properties of olfactory receptors analysed with odour pulses of varying durations. *J Physiol*, 282:541–560, Sep 1978.

[31] Y Gu, P Lucas, and J P Rospars. Computational model of the insect pheromone transduction cascade. *PLoS Comput Biol*, 5(3), Mar 2009.

[32] A Haase and K Hartung. Activation and inactivation kinetics of a Ca^{2+}-activated Cl^{-} current: photolytic Ca^{2+} concentration and voltage jump experiments. *Pflugers Arch*, 452(1):81–90, Apr 2006.

[33] G Halnes, E Ulfhielm, E Eklöf Ljunggren, J H Kotaleski, and J P Rospars. Modelling and sensitivity analysis of the reactions involving receptor, G-protein and effector in vertebrate olfactory receptor neurons. *J Comput Neurosci*, 27(3):471–491, Dec 2009.

[34] R.D. Hamer, S.C. Nicholas, D. Tranchina, T.D. Lamb, and J.L.P. Jarvinen. Toward a unified model of vertebrate rod phototransduction. *Vis Neurosci*, 22(4):417–36, 2005.

[35] B. Hille. *Ion Channels of Excitable Membranes*. Sinauer, 2001.

[36] Pablo A. Iglesias. Chemoattractant signaling in dictyostelium: Adaptation and amplification. *Sci. Signal.*, 5(213):pe8, 2012.

[37] Pablo A. Iglesias. A systems biology view of adaptation in sensory mechanisms. In Igor I. Goryanin and Andrew B. Goryachev, editors, *Advances in Systems Biology*, volume 736 of *Advances in Experimental Medicine and Biology*, pages 499–516. Springer New York, 2012.

[38] U B Kaupp. Olfactory signalling in vertebrates and insects: differences and commonalities. *Nat Rev Neurosci*, 11(3):188–200, Mar 2010.

[39] J.P. Keener and J. Sneyd. *Mathematical Physiology*. Interdisciplinary applied mathematics: Mathematical biology. Springer, 1998.

[40] S J Kleene. The electrochemical basis of odor transduction in vertebrate olfactory cilia. *Chem Senses*, 33(9):839–859, Nov 2008.

[41] B E Knox, P N Devreotes, A Goldbeter, and L A Segel. A molecular mechanism for sensory adaptation based on ligand-induced receptor modification. *Proc Natl Acad Sci U S A*, 83(8):2345–2349, Apr 1986.

[42] J I Korenbrot. Speed, sensitivity, and stability of the light response in rod and cone photoreceptors: Facts and models. *Prog Retin Eye Res*, 31(5):442–466, Sep 2012.

[43] DE Koshland. A response regulator model in a simple sensory system. *Science*, 196(4294):1055–1063, 1977.

[44] DE Koshland, A Goldbeter, and JB Stock. Amplification and adaptation in regulatory and sensory systems. *Science*, 217(4556):220–225, 1982.

[45] Y Koutalos and K W Yau. Regulation of sensitivity in vertebrate rod photoreceptors by calcium. *Trends Neurosci*, 19(2):73–81, Feb 1996.

[46] D Krizaj and D R Copenhagen. Calcium regulation in photoreceptors. *Front Biosci*, 7:2023–2044, Sep 2002.

[47] T Kurahashi. Activation by odorants of cation-selective conductance in the olfactory receptor cell isolated from the newt. *J Physiol*, 419:177–192, Dec 1989.

[48] T Kurahashi and A Menini. Mechanism of odorant adaptation in the olfactory receptor cell. *Nature*, 385(6618):725–729, Feb 1997.

[49] T Kurahashi and T Shibuya. Ca^{2+}-dependent adaptive properties in the solitary olfactory receptor cell of the newt. *Brain Res*, 515(1-2):261–268, May 1990.

[50] A Kuruma and H C Hartzell. Bimodal control of a Ca^{2+}-activated Cl^{-} channel by different Ca^{2+} signals. *J Gen Physiol*, 115(1):59–80, Jan 2000.

[51] L Lagostena and A Menini. Whole-cell recordings and photolysis of caged compounds in olfactory sensory neurons isolated from the mouse. *Chem Senses*, 28(8):705–716, Oct 2003.

[52] T D Lamb, H R Matthews, and V Torre. Incorporation of calcium buffers into salamander retinal rods: a rejection of the calcium hypothesis of phototransduction. *J Physiol*, 372:315–349, Mar 1986.

[53] H P Larsson, S J Kleene, and H Lecar. Noise analysis of ion channels in non-space-clamped cables: estimates of channel parameters in olfactory cilia. *Biophys J*, 72(3):1193–1203, Mar 1997.

[54] T Leinders-Zufall, C A Greer, G M Shepherd, and F Zufall. Imaging odor-induced calcium transients in single olfactory cilia: specificity of activation and role in transduction. *J Neurosci*, 18(15):5630–5639, Aug 1998.

[55] T Leinders-Zufall, M Ma, and F Zufall. Impaired odor adaptation in olfactory receptor neurons after inhibition of Ca^{2+}/calmodulin kinase II. *J Neurosci*, 19(14), Jul 1999.

[56] Lennart Ljung. *System identification: theory for the user*. Prentice Hall, Upper Saddle River, NJ, USA, 2nd edition, 1993.

[57] W. Ma, A. Trusina, H. El-Samad, W.A. Lim, and C. Tang. Defining network topologies that can achieve biochemical adaptation. *Cell*, 138(4):760–773, 2009.

[58] Miguel Maravall, Rasmus S. Petersen, Adrienne L. Fairhall, Ehsan Arabzadeh, and Mathew E. Diamond. Shifts in coding properties and maintenance of information transmission during adaptation in barrel cortex. *PLoS Biology*, 5(2):323 – 334, 2007.

[59] A Marchesi, M Mazzolini, and V Torre. Gating of cyclic nucleotide-gated channels is voltage dependent. *Nat Commun*, 3:973–973, 2012.

[60] H R Matthews and J Reisert. Calcium, the two-faced messenger of olfactory transduction and adaptation. *Curr Opin Neurobiol*, 13(4):469–475, Aug 2003.

[61] A Menini, C Picco, and S Firestein. Quantal-like current fluctuations induced by odorants in olfactory receptor cells. *Nature*, 373(6513):435–437, Feb 1995.

[62] R Milo, S Shen-Orr, S Itzkovitz, N Kashtan, D Chklovskii, and U Alon. Network motifs: simple building blocks of complex networks. *Science*, 298(5594):824–827, Oct 2002.

[63] L Moffatt. Estimation of ion channel kinetics from fluctuations of macroscopic currents. *Biophys J*, 93(1):74–91, Jul 2007.

[64] Dale Muzzey, Carlos A. Gmez-Uribe, Jerome T. Mettetal, and Alexander van Oudenaarden. A systems-level analysis of perfect adaptation in yeast osmoregulation. *Cell*, 138(1):160 – 171, 2009.

[65] V Nache, E Schulz, T Zimmer, J Kusch, C Biskup, R Koopmann, V Hagen, and K Benndorf. Activation of olfactory-type cyclic nucleotide-gated channels is highly cooperative. *J Physiol*, 569(Pt 1):91–102, Nov 2005.

[66] T Nakamura and G H Gold. A cyclic nucleotide-gated conductance in olfactory receptor cilia. *Nature*, 325(6103):442–444, Jan 1987.

[67] W T Nickell, N K Kleene, R C Gesteland, and S J Kleene. Neuronal chloride accumulation in olfactory epithelium of mice lacking NKCC1. *J Neurophysiol*, 95(3):2003–2006, Mar 2006.

[68] D Ottoson. Analysis of the electrical activity of the olfactory epithelium. *Acta Physiol Scand Suppl*, 35(122):1–83, 1955.

[69] H Y Park, S A Kim, J Korlach, E Rhoades, L W Kwok, W R Zipfel, M N Waxham, W W Webb, and L Pollack. Conformational changes of calmodulin upon Ca^{2+} binding studied with a microfluidic mixer. *Proc Natl Acad Sci U S A*, 105(2):542–547, Jan 2008.

[70] S Pifferi, A Boccaccio, and A Menini. Cyclic nucleotide-gated ion channels in sensory transduction. *FEBS Lett*, 580(12):2853–2859, May 2006.

[71] S Pifferi, M Dibattista, and A Menini. TMEM16B induces chloride currents activated by calcium in mammalian cells. *Pflugers Arch*, 458(6):1023–1038, Oct 2009.

[72] S Pifferi, G Pascarella, A Boccaccio, A Mazzatenta, S Gustincich, A Menini, and S Zucchelli. Bestrophin-2 is a candidate calcium-activated chloride channel involved in olfactory transduction. *Proc Natl Acad Sci U S A*, 103(34):12929–12934, Aug 2006.

[73] E.N. Pugh Jr. and T.D. Lamb. Phototransduction in vertebrate rods and cones: Molecular mechanisms of amplification, recovery and light adaptation. In D.G. Stavenga, W.J. de Grip, and E.N.Jr. Pugh, editors, *Handbook of Biological Physics*, pages 183–255. Elsevier Science B.V., Amsterdam, 2000.

[74] E.N. Pugh Jr., S Nikonov, and T.D. Lamb. Molecular mechanisms of vertebrate photoreceptor light adaptation. *Current Opinion in Neurobiology*, 9(4):410 – 418, 1999.

[75] R Y Pun and S J Kleene. Contribution of cyclic-nucleotide-gated channels to the resting conductance of olfactory receptor neurons. *Biophys J*, 84(5):3425–3435, May 2003.

[76] J Reidl, P Borowski, A Sensse, J Starke, M Zapotocky, and M Eiswirth. Model of calcium oscillations due to negative feedback in olfactory cilia. *Biophys J*, 90(4):1147–1155, Feb 2006.

[77] J. Reingruber and D. Holcman. The dynamics of phosphodiesterase activation in rods and cones. *Biophysical journal*, 94(6):1954–1970, 2008.

[78] J Reisert, P J Bauer, K W Yau, and S Frings. The Ca-activated Cl channel and its control in rat olfactory receptor neurons. *J Gen Physiol*, 122(3):349–363, Sep 2003.

[79] J Reisert and H R Matthews. Adaptation of the odour-induced response in frog olfactory receptor cells. *J Physiol*, 519 Pt 3:801–813, Sep 1999.

[80] J Reisert and H R Matthews. Adaptation-induced changes in sensitivity in frog olfactory receptor cells. *Chem Senses*, 25(4):483–486, Aug 2000.

[81] J Reisert and H R Matthews. Responses to prolonged odour stimulation in frog olfactory receptor cells. *J Physiol*, 534(Pt 1):179–191, Jul 2001.

[82] R T Roper, M Pia Saccomani, and P Vicini. Cellular signaling identifiability analysis: a case study. *J Theor Biol*, 264(2):528–537, 2010.

[83] C Sagheddu, A Boccaccio, M Dibattista, G Montani, R Tirindelli, and A Menini. Calcium concentration jumps reveal dynamic ion selectivity of calcium-activated chloride currents in mouse olfactory sensory neurons and TMEM16b-transfected HEK 293T cells. *J Physiol*, 588(Pt 21):4189–4204, Nov 2010.

[84] M A Savageau. Parameter sensitivity as a criterion for evaluating and comparing the performance of biochemical systems. *Nature*, 229(5286):542–544, Feb 1971.

[85] D Schild and D Restrepo. Transduction mechanisms in vertebrate olfactory receptor cells. *Physiol Rev*, 78(2):429–466, Apr 1998.

[86] B C Schroeder, T Cheng, Y N Jan, and L Y Jan. Expression cloning of TMEM16A as a calcium-activated chloride channel subunit. *Cell*, 134(6):1019–1029, Sep 2008.

[87] L. Shen, G. Caruso, P. Bisegna, D. Andreucci, V.V. Gurevich, H.E. Hamm, and E. DiBenedetto. Dynamics of mouse rod phototransduction and its sensitivity to variation of key parameters. *IET Systems Biology*, 4(1):12–32, 2010.

[88] Gordon M. Shepherd. *Neurobiology*. Oxford University Press, USA, 3 edition, May 1994.

[89] O Shoval, L Goentoro, Y Hart, A Mayo, E Sontag, and U Alon. Fold-change detection and scalar symmetry of sensory input fields. *Proc Natl Acad Sci U S A*, 107(36):15995–16000, Sep 2010.

[90] N Sim, D Bessarab, C M Jones, and L Krivitsky. Method of targeted delivery of laser beam to isolated retinal rods by fiber optics. *Biomed Opt Express*, 2(11):2926–2933, Nov 2011.

[91] E.D. Sontag. Remarks on feedforward circuits, adaptation, and pulse memory. *IET Systems Biology*, 4(1):39–51, 2010.

[92] A B Stephan, E Y Shum, S Hirsh, K D Cygnar, J Reisert, and H Zhao. ANO2 is the cilial calcium-activated chloride channel that may mediate olfactory amplification. *Proc Natl Acad Sci U S A*, 106(28):11776–11781, Jul 2009.

[93] H Stöhr, J B Heisig, P M Benz, S Schöberl, V M Milenkovic, O Strauss, W M Aartsen, J Wijnholds, B H Weber, and H L Schulz. TMEM16B, a novel protein with calcium-dependent chloride channel activity, associates with a presynaptic protein complex in photoreceptor terminals. *J Neurosci*, 29(21):6809–6818, May 2009.

[94] N Suzuki, M Takahata, and K Sato. Oscillatory current responses of olfactory receptor neurons to odorants and computer simulation based on a cyclic AMP transduction model. *Chem Senses*, 27(9):789–801, Nov 2002.

[95] K Takeda, D Shao, M Adler, P G Charest, W F Loomis, H Levine, A Groisman, W J Rappel, and R A Firtel. Incoherent feedforward control governs adaptation of activated ras in a eukaryotic chemotaxis pathway. *Sci Signal*, 5(205), Jan 2012.

[96] H Takeuchi and T Kurahashi. Photolysis of caged cyclic AMP in the ciliary cytoplasm of the newt olfactory receptor cell. *J Physiol*, 541(Pt 3):825–833, Jun 2002.

[97] H Takeuchi and T Kurahashi. Mechanism of signal amplification in the olfactory sensory cilia. *J Neurosci*, 25(48):11084–11091, Nov 2005.

[98] V Torre, J F Ashmore, T D Lamb, and A Menini. Transduction and adaptation in sensory receptor cells. *J Neurosci*, 15(12):7757–7768, Dec 1995.

[99] M C Trudeau and W N Zagotta. Calcium/calmodulin modulation of olfactory and rod cyclic nucleotide-gated ion channels. *J Biol Chem*, 278(21):18705–18708, May 2003.

[100] J J Tyson, K C Chen, and B Novak. Sniffers, buzzers, toggles and blinkers: dynamics of regulatory and signaling pathways in the cell. *Curr Opin Cell Biol*, 15(2):221–231, Apr 2003.

[101] J Valsamis, J Van Peborgh, and H Brauman. Relative contribution of various expressions of cAMP excretion to other indices of parathyroid function, as tested by discriminant multivariate linear regression analysis. *Clin Chem*, 32(7):1279–1284, Jul 1986.

[102] K.V. Venkatesh, Sharad Bhartiya, and Anurag Ruhela. Multiple feedback loops are key to a robust dynamic performance of tryptophan regulation in escherichia coli. *FEBS Letters*, 563(1-3):234 – 240, 2004.

[103] J Wei, A Z Zhao, G C Chan, L P Baker, S Impey, J A Beavo, and D R Storm. Phosphorylation and inhibition of olfactory adenylyl cyclase by CaM kinase II in Neurons: a mechanism for attenuation of olfactory signals. *Neuron*, 21(3):495–504, Sep 1998.

[104] Q Xiao, K Yu, P Perez-Cornejo, Y Cui, J Arreola, and H C Hartzell. Voltage- and calcium-dependent gating of TMEM16A/Ano1 chloride channels are physically coupled by the first intracellular loop. *Proc Natl Acad Sci U S A*, 108(21):8891–8896, May 2011.

[105] Y D Yang, H Cho, J Y Koo, M H Tak, Y Cho, W S Shim, S P Park, J Lee, B Lee, B M Kim, R Raouf, Y K Shin, and U Oh. TMEM16A confers receptor-activated calcium-dependent chloride conductance. *Nature*, 455(7217):1210–1215, Oct 2008.

[106] K W Yau and R C Hardie. Phototransduction motifs and variations. *Cell*, 139(2):246–264, Oct 2009.

[107] T M Yi, Y Huang, M I Simon, and J Doyle. Robust perfect adaptation in bacterial chemotaxis through integral feedback control. *Proc Natl Acad Sci U S A*, 97(9):4649–4653, Apr 2000.

[108] F Zufall and T Leinders-Zufall. The cellular and molecular basis of odor adaptation. *Chem Senses*, 25(4):473–481, Aug 2000.